

**UNIVERSITÀ DEGLI STUDI DI NAPOLI  
FEDERICO II**



**DIPARTIMENTO DI INGEGNERIA CHIMICA, DEI MATERIALI  
E DELLA PRODUZIONE INDUSTRIALE**

*Dottorato di Ricerca in Ingegneria Chimica – XXVIII Ciclo*

**PhD THESIS**

**CHEMICAL STORAGE OF  
CONCENTRATED SOLAR POWER**

**Scientific Committee**

*Prof. Piero Salatino*

*Prof. Fabio Montagnaro*

*Prof. Roberto Solimene*

*Prof. Martino Di Serio*

**PhD Student**

Claudio Tregambi

# CHEMICAL STORAGE OF CONCENTRATED SOLAR POWER

## Chapter I. State of the Art

I.1	Global Overview of the World Energetic and Environmental Panorama .....	1
I.2	Solar Energy and Concentrating Solar Power Systems .....	3
I.3	Thermal Energy Storage .....	6
I.4	Thermochemical Energy Storage .....	8
I.4.1	Hydrides.....	10
I.4.2	Hydroxides.....	11
I.4.3	Carbonates .....	13
I.4.4	Oxides .....	15
I.4.5	Solar Fuels Production.....	16
I.5	The Role of Fluidized Bed as Solar Thermal Receiver .....	22
I.6	Current CSP Plants in the World .....	23
I.7	Alternative Strategies for CO <sub>2</sub> Reduction: the Calcium Looping Cycle .....	27
I.8	Aim of the PhD Thesis .....	29

## Chapter II. A Model of Integrated Calcium Looping for CO<sub>2</sub> Capture and Concentrated Solar Power

II.1	Introduction.....	30
II.2	The Model.....	30
II.2.1	Outline of the CaL-CSP Integrated Scheme and Main Assumptions .....	30
II.2.2	Model Equations.....	31
II.2.3	Evaluation of Parameters.....	36
II.2.4	Model Implementation .....	38
II.3	Results and Discussion .....	38
II.3.1	Results of Base Case Model Computations .....	38
II.3.2	Effect of the Operating Parameters .....	39
II.4	Final Remarks.....	43
II.5	Model Nomenclature .....	44

## **Chapter III. Heat Transfer in Directly Irradiated Fluidized Beds**

III.1	Introduction.....	46
III.2	Experimental Apparatus, Diagnostics and Materials.....	46
III.2.1	Fluidized Bed Reactor.....	47
III.2.2	Solar Simulator: Short-Arc Xenon Lamp and Optical Reflectors.....	47
III.2.3	Bubble Generation System.....	49
III.2.4	Thermal Infrared Camera.....	49
III.2.5	Capacitance Probes.....	49
III.2.6	Gas Meter.....	50
III.2.7	Radiative Heat Flux Sensor.....	50
III.2.8	Materials.....	51
III.3	Characterization.....	51
III.3.1	SiC Emissivity.....	51
III.3.2	Xe-Lamp Thermal Power.....	52
III.3.3	Bubble Generation System Features.....	56
III.4	Experimental Procedure and Operating Conditions.....	58
III.5	Results and Discussion.....	59
III.5.1	Analysis of Thermal Maps of the Bed Surface Upon Irradiation.....	59
III.5.2	Analysis of the Temperature Time-Series at the Focal Point.....	66
III.5.3	A Compartmental Model of In-Bed Dispersion of Radiative Flux.....	67
III.6	Final Remarks.....	74

## **Chapter IV. Design of a Fluidized Bed Solar Reactor and Application to Calcium Looping Process**

IV.1	Introduction.....	75
IV.2	Basic Design of the Solar Reactor.....	75
IV.2.1	Geometrical Features.....	75
IV.2.2	Process Operating Conditions.....	76
IV.2.3	Fluidized Bed Surface Over-Temperature.....	76
IV.2.4	Energy Balance.....	77
IV.3	Mechanical Design of the Solar Fluidized Bed Reactor.....	78
IV.4	Experimental Apparatus, Diagnostics and Materials.....	80

IV.4.1 Semi-Cylindrical Ceramic Fiber Heaters.....	82
IV.4.2 Gas Preheater .....	82
IV.4.3 Infrared Pyrometer .....	83
IV.4.4 Gas Analyzer.....	84
IV.4.5 Materials .....	84
IV.5 Characterization of the Solar Simulator.....	85
IV.6 Experimental Procedure.....	86
IV.7 Results and Discussion.....	88
IV.7.1 A Complete Calcination-Carbonation Cycle .....	88
IV.7.2 Detailed Analysis of the First and Fourth Carbonation Steps .....	89
IV.7.3 TGA and XRD Analysis of the Calcined Sample.....	91
IV.7.4 CO <sub>2</sub> Capture Efficiency .....	92
IV.8 Final Remarks .....	93

**Chapter V. Final Remarks and Future Developments..... 94**

**References..... 96**

# Chapter I. State of the Art

## I.1 Global Overview of the World Energetic and Environmental Panorama

Renewable sources are becoming ever more important in recent years as their use represent both a significant key climate change mitigation technology and a decisive route toward freedom from fossil fuel dependency. The increase in renewable energy use continued during last years despite the increasing global energy consumption and the substantial decline in oil prices. By the end of 2013, renewable energy provided nearly 19.1% of the global energy consumption, larger than the 16.7% market share registered in 2010. More in detail, the renewable market share can be further distinguished into contributions from traditional biomass and modern renewables. The former mainly refers to materials coming in the form of unprocessed agricultural waste or animal dung, mainly used for cooking and heating in remote and rural area of developing countries, while the latter include solar, wind, geothermal, and hydropower energy together with that produced through modern biomasses or biofuels. Taking into account these two subcategories, the modern renewables account for nearly 10% while the remaining 9% is ascribed to the traditional biomass (Figure I.1).

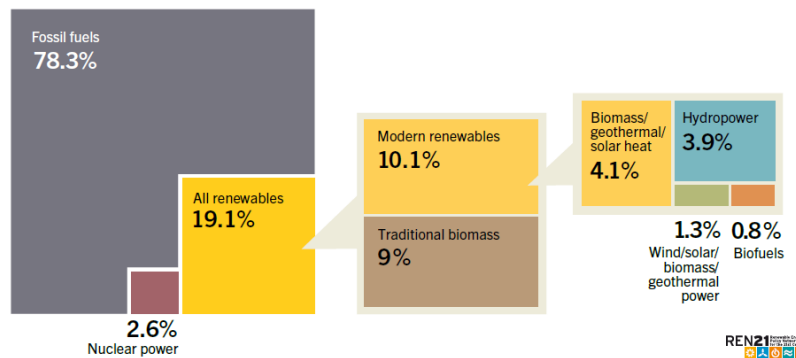


**Figure I.1:** Estimated renewable energy share of global final energy consumption in 2013.

The statistical data discussed so far refer to the global final energy consumption, which means that they take into account the power, heat and transport contributes. By solely referring to the power sector, renewable sources comprised an estimated 27.7% share of the world's power generating capacity at the end of 2014, with a total power capacity of 1712 GW (8.5% more than 2013). The distribution among the renewable sources is largely dominated by the hydropower energy, followed by wind power (the least-cost option), solar photovoltaic and bio-power (Figure I.2).

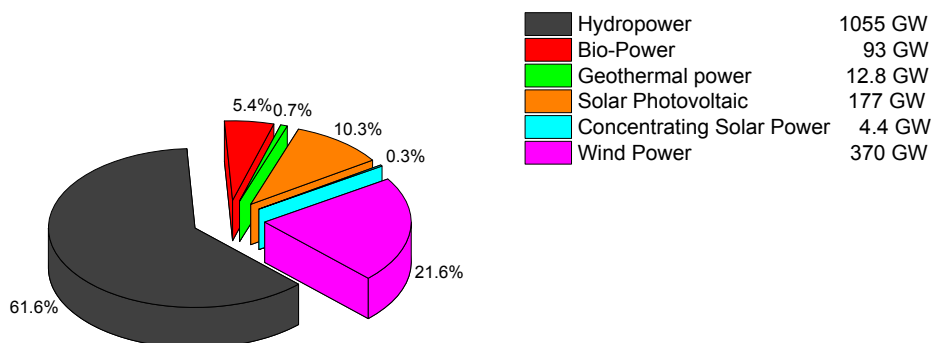


**Figure I.2:** Distribution among renewable energy sources in the power sector.

The Concentrating Solar Power (CSP) market remains less established than most other renewable energy markets, probably because it is a relatively new technology compared to the other ones. However, it is worth to note that its growth rate was, together with that of the solar photovoltaic, one of the larger during last years (Figure I.3). All the statistical data so far discussed, and more of them, can be found in *REN21*, 2015.

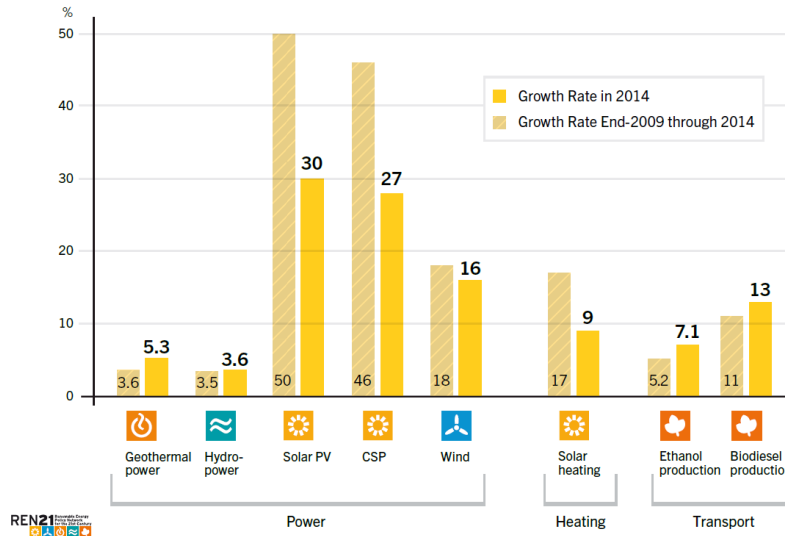


**Figure I.3:** Average annual growth rates of renewable energy capacities.

On a parallel line, the atmospheric CO<sub>2</sub> concentration is incessantly increasing in last decades due to the continuous use of fossil fuels. A value of nearly 402 ppm has been reached in December 2015 (Figure I.4). The upper safety limit, which is stated to be around 350 ppm, has been largely exceeded since 1990. Important efforts are required in the next years to let this value decrease through an extensive use of renewable sources or through the use of carbon capture and sequestration technologies, so as to avoid or at least limit the serious climate changes induced by the global warming.

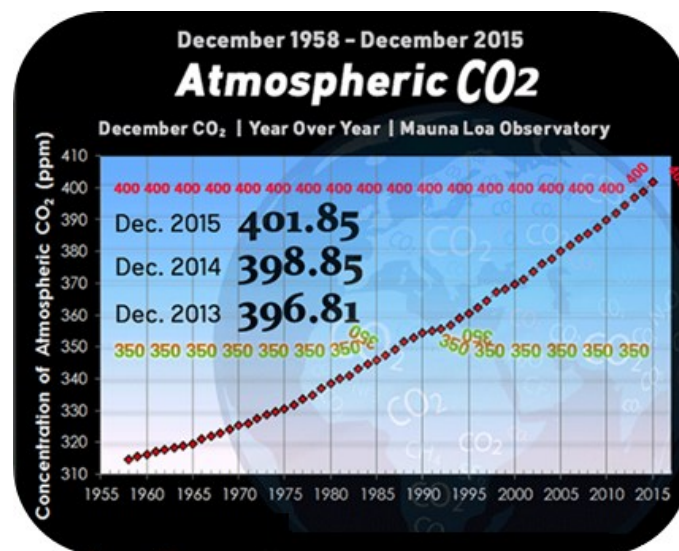


**Figure I.4:** Atmospheric CO<sub>2</sub> concentration over last 50 years.<sup>1</sup>

<sup>1</sup> <http://co2now.org/>

## I.2 Solar Energy and Concentrating Solar Power Systems

Among the renewable sources, energy coming from the sun is one of the most important to reach the global energy needs without the concomitant production of greenhouse gases. A simple comparison between the current global energy consumption rate (~16 TW) and the huge amount of solar energy falling on the Earth (~100,000 TW) lead to the conclusion that just 0.1% of the Earth's land would be needed to supply the energy for all the inhabitants of the planet if considering an energy conversion efficiency of 20% (Steinfeld and Meier, 2004). The solar energy is also free and theoretically infinite. However, despite the enormous advantages related to the use of solar energy, some relevant drawbacks exist. First of all, the solar energy is an intermittent energy source as it is available only during the day (intended as the fraction of the astronomical day comprised between dawn and sunset) and only in clear-sky conditions. Moreover, the solar radiation is also quite diluted, with a maximum flux density of  $1 \text{ kW m}^{-2}$  in the most irradiated regions (generally referred as sunbelt), and unequally distributed around the Earth. A map of the worldwide solar distribution is depicted in Figure I.5.

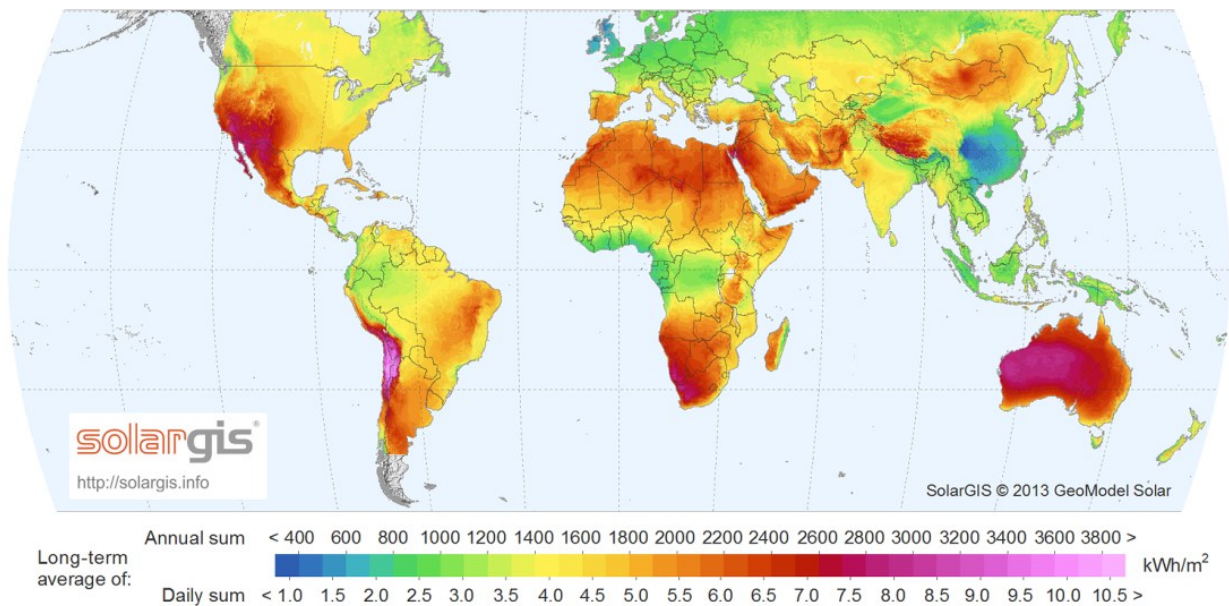


**Figure I.5:** World map of direct normal irradiation.

Radiant energy coming from the sun hits the Earth with a spectral distribution ranging in the  $0.1\text{--}10 \mu\text{m}$  interval. Three regions can be distinguished: UV, Visible and IR. The UV region includes radiation with a wavelength up to 400 nm, and at Earth's surface accounts for 3–5% of the total energy. The Visible region ranges from 400 to 700 nm and accounts for 42–43% of the total energy, while the IR region includes wavelengths above 700 nm and accounts for 52–55% of the total energy. At the top of the atmosphere, UV radiations are more intense and account for 7–8% of the total energy. The solar spectrum is quite similar to that of a blackbody emitter at a temperature of 5800 K (Figure I.6). Nowadays, two major strategies exist to take advantage of the solar energy: photovoltaic and CSP systems.

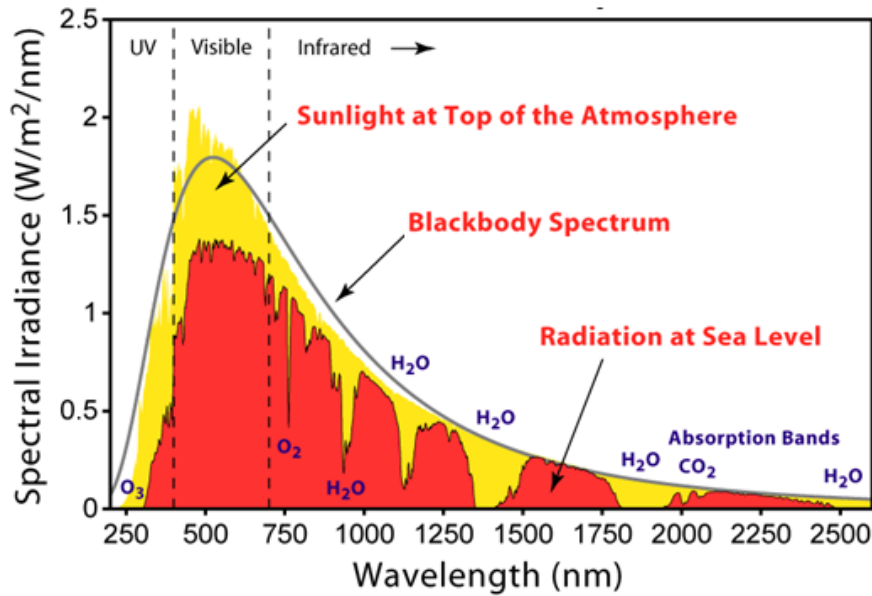


**Figure I.6:** Spectral distribution of the sun and of a blackbody emitter.

Photovoltaic consists into the direct conversion of the solar energy into electricity. The core of these systems is represented by a light absorbing material, capable of absorbing photons and generate free electricity via the photovoltaic effect. In its easier formulation, the conversion is accomplished using a p-n junction, a device realized assembling two different doped semiconductor layers. More specifically, one layer is doped with a lower valence cation, while the other one is doped with a higher valence cation (e.g., Ga and P in the case of Si layer). Current available devices suffer of a relatively short life-time (due to degradation problems) and of a decadency of efficiency over the time. Moreover, an effective storage of the energy produced with photovoltaic devices is still highly expensive. The research in the photovoltaic sector is greatly active to overcome the aforementioned drawbacks and is also focused on enhancing the solar-to-electric conversion efficiency. Actually, the average conversion efficiency for commercial solar cells is around 12–18%. Multi-junction cells can have far larger efficiencies thanks to the combination of different semiconductor materials able to use different ranges of the solar spectrum, but their complexity and related costs are higher too. Laboratory multi-junction solar cells claim efficiencies as large as 40%, with a current world record of 44.7%. Nowadays the solar photovoltaic is already an important reality in the worldwide economy, with a production of over 170 GW of energy (see Figure I.2). A lot of commercial plants exist all over the world and their number is readily increasing as the price of photovoltaic systems is rapidly declining. Comprehensive reviews on photovoltaic systems can be found in the literature (*El Chaar et al.*, 2011, *Parida et al.*, 2011).

Concentrating Solar Power systems instead rely on the concentration of the solar energy by the use of optical mirrors. The concentrated solar energy can be used to heat a working fluid at the high temperatures required to drive a thermodynamic cycle (e.g., Rankine, Brayton, Stirling) and produce energy. Reflection and concentration are achieved by sun-tracking mirrors, called heliostats, which collect and concentrate the incident solar radiation onto a solar receiver. Different types of CSP systems are currently applied at pilot and commercial scale and are generally distinguished in one-axis and two-axis tracking technologies. A crucial parameter which characterizes all these systems is the concentration ratio, defined as the mean solar radiation power flux over the focused area normalized to the total incident solar radiation (*Romero and Steinfeld*,

2012). This parameter limits the maximum achievable temperatures in the solar receiver, as easily shown from an energy balance performed on a perfect blackbody receiver (Eq. I.1):

$$\alpha IC = \varepsilon \sigma T^4 \quad (\text{I.1})$$

$\alpha$  and  $\varepsilon$  are the absorption and emission coefficients, and are both unitary for a perfect blackbody receiver.  $I$  and  $C$  are, respectively, the incident solar radiation and the concentration ratio, while  $\sigma$  is the Stefan–Boltzmann coefficient.  $T$  is the maximum theoretically achievable temperature, sometimes referred as the stagnation temperature.

Main one-axis technologies are the parabolic trough collector and the linear Fresnel reflector. Parabolic trough systems (Figure I.7-a) use reflectors of parabolic shape to focus the solar radiation along a receiver located on the focal line of the collectors. A long pipe receiver can be placed at the focus for the heating of a heat transfer fluid. On the contrary, linear Fresnel reflector systems (Figure I.7-b) are composed of very long rows of parallel flat or slightly curved mirrors that focus the solar radiation on an elevated long receiver fixed in space above the mirror field. The receiver is usually a metal absorber tube embedded in an evacuated glass tube to reduce heat losses (Mills, 2004). Concentration ratios achieved are not too high, in the order of 30–100 for both systems.

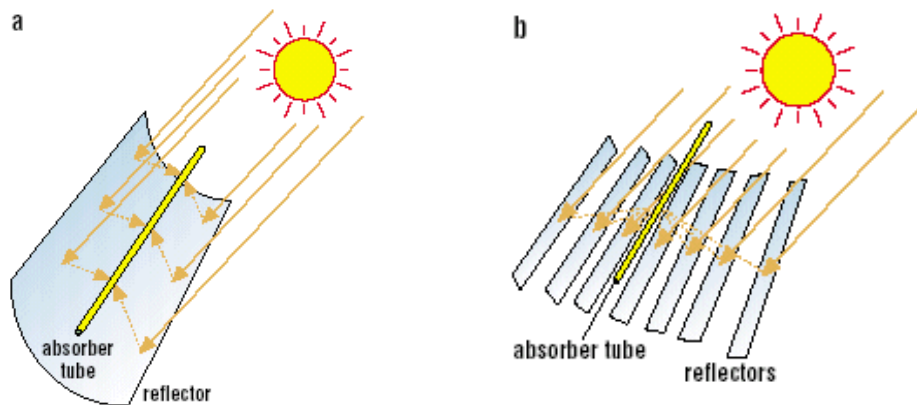


**Figure I.7:** One-axis tracking technologies. a) Parabolic trough systems; b) Linear Fresnel reflector.

Main two-axis technologies are instead the parabolic dish, the solar tower system and the beam down tower (also known as double concentration system). Parabolic dish systems (Figure I.8-left) are point focus collectors that make use of a parabolic concave mirror (the dish) to concentrate the solar radiation by tracking the sun along two axis. The receiver is located at the focal point of the dish and is generally coupled with a Stirling engine or a Brayton mini-turbine. These systems are generally autonomous modules that produce energy in the 5–25 kW power range. Concentration ratios are high (1000–3000). Differently, in the solar tower system (Figure I.8-centre) a field of hundreds/thousands of large two axis tracking mirrors are installed around a tower, on the top of which the receiver is mounted. Since large heat losses are always involved in the heat transport from the solar receiver to the energy converter, this system requires that turbine and/or other equipment are installed close to the receiver, and hence must be supported on the top of the tower. Concentration ratio ranges from 300 to 1500. To overcome the drawbacks related to the solar tower system, the beam down tower has been developed. This system (Figure I.8-right) is quite similar to the solar tower system but has an additional mirror that reflects downwards the

concentrated beam arising from the heliostat field. The second mirror is a reflective surface characterized by two foci, hence an hyperbole or an ellipse. Hyperboloidal mirrors are generally preferred because they require lower mounting height and inferior dimension (*Segal and Epstein, 2000*). An additional concentrator close to the receiver may be required if the additional mirror causes a magnification of the sun image. The receiver can then be coupled with a Compound Parabolic Concentrator (CPC) to reach larger concentration ratios, in the order of 5000–10000 (*Kodama, 2003*).

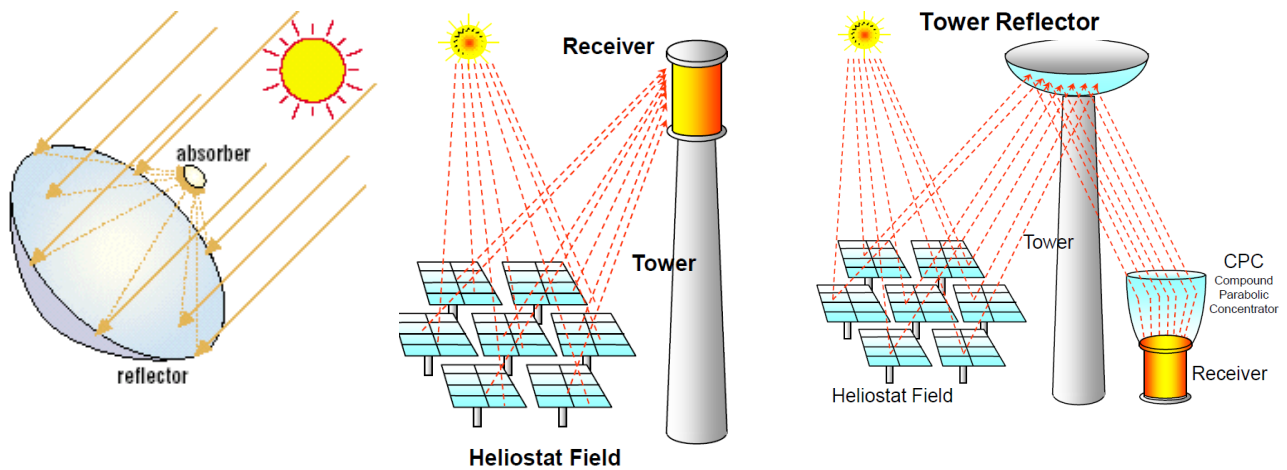


**Figure I.8:** Two-axis tracking technologies. Left: Parabolic dish; Centre: Solar tower system; Right: Beam down tower with CPC (double concentration system).

### I.3 Thermal Energy Storage

A great advantage of the CSP technology over its direct photovoltaic competitor is that CSP plants can be easily integrated with Thermal Energy Storage (TES) systems. Thermal storage consists in the collection of the excess heat produced by CSP systems into storage mediums able to release the absorbed energy when required (for instance, after the sunset or during cloudy days). TES systems play then a key role in the process, as they allow to correct the mismatch between the discontinuous solar energy supply and the continuous electricity demand, enabling the production of energy at a stable rate. Moreover, their use permit to uncouple the processes of collection and production of energy: it is therefore possible to correct the temporal mismatch existing between the fraction of the daytime in which energy is produced and the fraction of the daytime in which energy is actually required. Depending on the nature of the TES system applied, the stored energy can be also transported and used in different location and/or period of time, amplifying in this way the potentialities of solar energy. Used in combination with fossil fuel backup, TES systems can keep a CSP plant running under full-load conditions also after the sunset, setting the stage for the development of a base-load solar power plant. The energy storage process involves at least three steps: 1) charging, 2) storage, and 3) discharging. During the charging step, the energy coming from the sun is collected into a storage medium. This energy is then stored until it becomes necessary, when it is released in the discharging step. Three different mechanisms are currently studied, and they are based on sensible, latent and thermochemical heat storage.

In sensible heat storage, the solar energy is used to increase the temperature (hence the energy content) of a fluid or solid medium. The stored energy ( $Q_{stored}$ ) is directly connected to the

amount of the storage medium ( $m$ ), to its thermal capacity ( $C_p$ ) and to the experienced temperature increment (Eq. I.2):

$$Q_{stored} = mC_p\Delta T \quad (I.2)$$

During the discharging step, the energy is released at unsteady temperature as the temperature of the storage medium progressively decreases. Materials are chosen by taking into account several parameters, such as the energy density, the thermal diffusivity, and the mechanical/thermal stability. Concerning solid media, inexpensive materials such as rock, sand, concrete and cast ceramics have been extensively studied mainly due to their low cost and average thermal conductivity, which ensures good heat transfer rate without preventing the use of thermocline storage systems. As liquid media, molten salts (mixtures of two or more nitrate salts, such as  $\text{Ca}(\text{NO}_3)_2$ ,  $\text{NaNO}_3$ ,  $\text{KNO}_3$ ) and mineral or synthetic oils are investigated. The high freezing point of most molten salts is a relevant problem because heat must be supplied also in non-functioning periods to avoid the salt solidification (*Fernandes et al.*, 2012; *Gil et al.*, 2010).

In latent heat storage, the solar energy is used to achieve a phase transformation of a solid or liquid medium. Among them, the solid-liquid transition is considered to be the more efficient because solid-solid transitions generally feature quite low latent heat values while liquid-gas transitions require large volume of recipient (*Fernandes et al.*, 2012). The stored energy is related to the latent heat of the phase transformation involved ( $\Delta_{transf}H$ ) and to the amount of the storage medium (Eq. I.3):

$$Q_{stored} = m\Delta_{transf}H \quad (I.3)$$

During the discharging step, energy is released at steady temperature as phase transitions are isothermal processes. Both organic and inorganic compounds are used for latent heat storage. As inorganic materials, salt like  $\text{NaNO}_3$ ,  $\text{KNO}_3$ ,  $\text{KOH}$ ,  $\text{NaCl}$ ,  $\text{Na}_2\text{CO}_3$  have been investigated. On the other hand, paraffins and fatty acids have been investigated as organic materials. Two relevant drawbacks of the latent heat storage systems are the low thermal conductivities, that lead to slow charging-discharging rates, and the possible formation of solid deposits on the heat transfer surface. Thermal conductivities can be partially enhanced by using composite materials, in which the properties of a material featuring a high latent heat are combined with the ones of a second material owning a good thermal conductivity. For this purpose, graphite is commonly used as additive. Several reviews concerning latent heat storage materials and technologies can be found in the literature (*Herrmann and Kearney*, 2002; *Gil et al.*, 2010).

Lastly, in thermochemical heat storage the energy arising from the sun is used to perform an endothermic reversible chemical reaction. Reaction products must be separated and can be stored at any temperature. The stored energy is dependent on the latent heat of the performed reaction ( $\Delta_{reaction}H$ ) and on the amount of converted material (Eq. I.4):

$$Q_{stored} = m\Delta_{reaction}H \quad (I.4)$$

During the discharging step, the reaction products are mixed back and reacted in order to release the stored energy and regenerate the original reagents. Energy is released at steady temperature.

Thermochemical storage systems are technologically more complex than sensible and latent heat storage ones but, at the same time, own some peculiarities which give them huge advantages and that strongly encourage the research in this field. Indeed, the theoretical stored energy is significantly larger and both the storage period and the transport distance are theoretically unlimited. This two features virtually allow to transport the solar energy into regions different from the production site where the CSP plant is located. The main properties of the three different storage mechanisms are briefly summarized in Table I.1.

	Energy Storage Technology		
	Sensible heat	Latent heat	Thermochemical
<b>Volumetric density</b>	Small (50 kWh m <sup>-3</sup> )	Medium (100 kWh m <sup>-3</sup> )	High (500 kWh m <sup>-3</sup> )
<b>Gravimetric density</b>	Small (0.02 kWh kg <sup>-1</sup> )	Medium (0.07 kWh kg <sup>-1</sup> )	High (0.7 kWh kg <sup>-1</sup> )
<b>Storage temperature</b>	Charging value	Charging value	Ambient
<b>Storage period</b>	Limited (thermal losses)	Limited (thermal losses)	Theoretically unlimited
<b>Transport distance</b>	Small	Small	Theoretically unlimited
<b>Technology</b>	Simple	Medium	Complex

**Table I.1:** Main properties of the three energy storage technologies (*Pardo et al.*, 2014b).

## I.4 Thermochemical Energy Storage

Thermochemical storage can offer several advantages over sensible and latent heat storage. The choice of an appropriate reaction is the main key for the success of this heat storage mechanism. Virtually any reaction can be chosen, but several parameters need to be taken into account. The chemistry of the reaction itself is obviously of fundamental importance: good selectivity and reversibility are required, as well as high reaction rates, optimal operating conditions and large reaction enthalpies. A good material stability and resistance towards chemical poisons are also required, so that several cycles can be accomplished before deactivation phenomena take place. Lastly, materials toxicity and cost have also to be accounted for. It is quite impossible to find a chemical reaction or a chemical compound able to fully satisfy all the expectations, thus the best system will be the one which better fits the different properties. Among the possible reactions, a first important line should be marked between “pure” chemical reactions and sorption processes.

The word “sorption” has been used in the literature as a general term to cover both adsorption and absorption processes. Adsorption is a surface process and, in thermochemical storage application, it is generally referred to the gas–solid adsorption. It can be further divided into physical adsorption, in which intermolecular forces (van der Waals) are involved, and chemical adsorption, in which covalent forces are involved. Chemical adsorption provides higher heat of reaction due to the stronger nature of covalent forces with respect to van der Waals ones. More specifically, when the adsorption has a physical nature, the reaction heat is of the same order of magnitude of the latent heat of condensation-liquefaction of the adsorbed gaseous species, thus hardly exceeding values of 40–50 kJ mol<sup>-1</sup>. Differently, absorption is defined as a phenomenon in which a liquid or a gas penetrates into the surface layer and enters the bulk structure of a solid or a liquid: in thermochemical storage application it is generally referred to liquid-gas systems. The sorption process can be generalized by the reaction:



where A is the sorbent and B the sorbate. The chemical nature of  $A \cdot (m+n)B$  differs whether the considered process is a gas–solid adsorption or a gas-liquid absorption. In the former case, the reaction describes the enrichment of the B species on the A surface. Differently,  $A \cdot (m+n)B$  represents a solution with a lower concentration of A than  $A \cdot mB$ . To improve sorption properties, composite sorbents called composite salt porous matrix have been proposed. These materials are made up by the combination between a salt hydrate and an additive characterized by a porous structure and a high thermal conductivity. The additive can have or not sorption properties. Materials such as expanded graphite, activated carbon as well as silica gel, alumina and aerogel are currently used as host matrix, while the salts can be chlorides, sulphates or nitrates such as  $\text{CaCl}_2$ ,  $\text{MgSO}_4$  and  $\text{LiNO}_3$ . When inert matrixes are used, advantages in terms of improved heat and mass transfers are obtained. Differently, when absorbent matrixes are used, the sorption process becomes a combination between absorption and adsorption, as both chemical reaction and liquid absorption occur. Sorbates commonly used in chemical sorption processes are water, ammonia and hydrogen. The sorption processes investigated in the literature are mostly characterized by relatively low temperatures for the charging-discharging process. These processes are indeed used to store low grade (<100 °C) and medium grade (100–400 °C) heat. The release of energy is performed at temperatures generally lower than 200–250 °C. As a consequence, the application fields for sorption processes are limited to buildings heating/cooling, hot water production and air-heating systems rather than electricity production through thermodynamic cycles (where temperature values of at least 450–500 °C are required). Several reviews concerning sorption processes can be found in the literature (*N'Tsoukpoe et al.*, 2009 and 2014; *Cot-Gores et al.*, 2012; *Yu et al.*, 2013). An exhaustive graph reporting the energy storage densities and the operative temperatures for most of the investigated sorption processes is reported in Figure I.9.

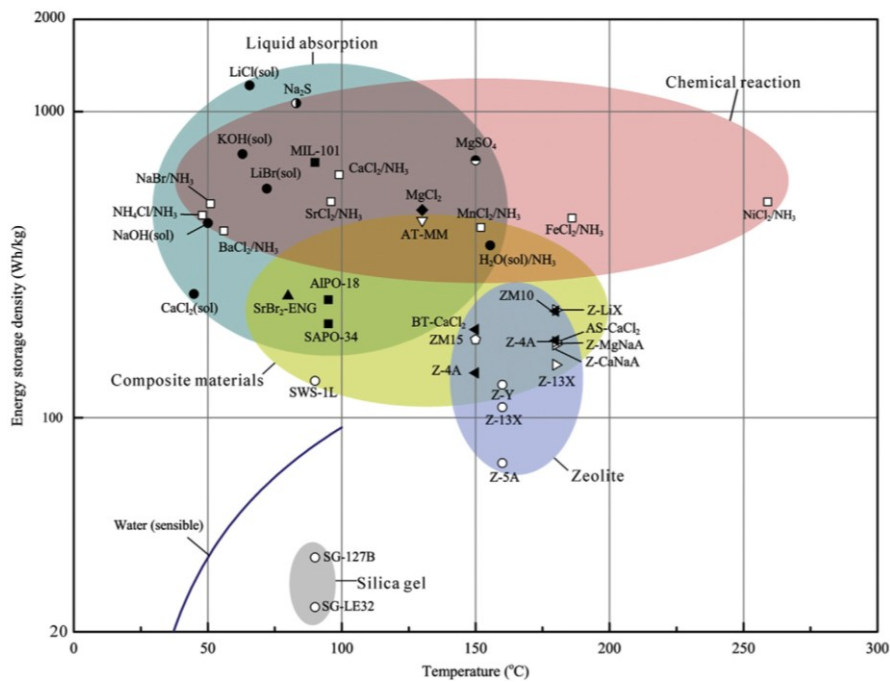


**Figure I.9:** Energy storage densities of sorption materials. Sorbate is  $\text{H}_2\text{O}$  if not specified (*Yu et al.*, 2013).

Sorption processes can be further distinguished into open and closed systems. The former can exchange both mass and energy with the surrounding environment, while the latter only energy. Closed systems are technologically more expensive, and are limited by heat transfer rate due to an indirect contact between the storage material and the heat source. However, a wider range of compounds can be used in closed systems, as the produced species are not released into the environment or diluted by the flow of process gases. On the contrary, open systems are less expensive and can benefit of larger heat and mass transfer coefficients, but they are more limited in the choice of the sorbate due to the direct release in the environment of the produced species.

“Pure” chemical reactions can be distinguished from the sorption processes basically due to the formation of new chemical compounds. From trivial thermodynamic considerations, it can be shown that, at equilibrium conditions:

$$\Delta H = T_{eq}\Delta S \quad (I.5)$$

A direct consequence of Eq. I.5 is that in order to obtain large reaction enthalpies, processes with large entropies variation are required, hence processes in which gaseous species are released. The equilibrium temperature ( $T_{eq}$ ) (also referred as the turning temperature) is a parameter of fundamental importance, as it sets the threshold temperature for the specific process at which is referred: temperatures higher or lower than  $T_{eq}$  will shift the reaction towards opposite directions. Several chemical reactions have been proposed for thermochemical storage. Decomposition processes are the most studied systems (*Pardo et al.*, 2014b): heat is used to dissociate a chemical compound into two products, often a solid one and a gaseous one which must be separated and stored. When energy is required the inverse reaction is accomplished, so as to release the heat absorbed during the decomposition process. As previously discussed for the sorption process, both closed and open system can be here realized, with almost the same advantages and drawbacks. Following the path driven by several authors worldwide, thermochemical storage reactions can be classified into several systems. Hydrides, hydroxides, carbonates and oxides-based systems will be briefly described in the following, as they represent some of the more interesting classes of materials for thermochemical storage. Lastly, a peculiar strategy of TES in which the solar energy is used to produce solar fuels will be documented.

#### **I.4.1 Hydrides**

This class of materials uses  $H_2$  as a working medium and has been initially investigated for the storage of  $H_2$  in solid state. The general reaction can be schematized as follows:



$MgH_2$  is one of the most studied compounds. It is characterized by a  $\Delta H$  of  $75 \text{ kJ mol}^{-1}$  and by a working temperature of  $250\text{--}500 \text{ }^\circ\text{C}$  for an  $H_2$  partial pressure of  $1\text{--}100 \text{ bar}$ . The  $H_2$  storage capacity is the largest among reversible binary hydrides ( $\sim 7.6\%_{\text{wt}}$ ) and the price of the raw material is quite low. The reaction has been proved to be highly reversible, with more than 500 cycles achieved. The main drawbacks of this system are a slow reaction kinetics (partially solved through the doping with transition metals like Fe or Ni), and the high operative pressures. Other studied metal hydride compounds are  $NaMgH_3$  and  $Mg_2FeH_6$ . The former is characterized by a slightly

larger reaction enthalpy ( $86 \text{ kJ mol}^{-1}$ ) and by a lower  $\text{H}_2$  dissociation pressure with respect to  $\text{MgH}_2$ . Long-term behaviour of this material is unknown and currently under investigation.  $\text{Mg}_2\text{FeH}_6$  is instead characterized by a  $\Delta H$  of  $77 \text{ kJ mol}^{-1}$ . Its main advantage with respect to the  $\text{MgH}_2/\text{Mg}$  system is the lower dissociation pressure of 66 bar at  $500 \text{ }^\circ\text{C}$  (instead of 100 bar for  $\text{MgH}_2$ ) and the superior cycle stability under high temperature and pressure conditions (*Felderhoff and Bogdanović, 2009*). A metal hydride system that can be exerted at high operating temperature is instead  $\text{CaH}_2$ . The operative temperature is indeed around  $900 \text{ }^\circ\text{C}$  and the reaction enthalpy, much larger than for the previous compounds, is equal to approximately  $180 \text{ kJ mol}^{-1}$ . The performances of this material as heat storage compound for CSP are under investigation (*Felderhoff et al., 2013*). In Table I.2 the properties of the described metal hydrides are briefly summarized.

	<b>H<sub>2</sub> content</b> [%wt]	<b><math>\Delta H</math></b> [kJ mol <sup>-1</sup> H <sub>2</sub> ]	<b>Heat storage density</b> [kW h kg <sup>-1</sup> ]	<b>T<sub>eq</sub> at 1 bar</b> [°C]
<b>MgH<sub>2</sub></b>	7.7	75	0.78	280
<b>NaMgH<sub>3</sub></b>	4.0	86	0.47	380
<b>Mg<sub>2</sub>FeH<sub>6</sub></b>	5.5	77	0.55	320
<b>CaH<sub>2</sub></b>	4.8	181	1.19	950

**Table I.2:** Main parameters of the most relevant metal hydrides for thermochemical energy storage.

In heat storage application, metal hydrides have to be used in closed systems so that the  $\text{H}_2$  is preserved during a great number of cycles. To avoid the use of a compressor to liquefy the  $\text{H}_2$  during the storage step, low temperature  $\text{H}_2$  absorbing alloys can be conveniently used. These compounds are typically hydrides on Fe-Ti or La-Ni basis and allow the availability of  $\text{H}_2$  at ambient temperatures. Metal hydrides are interesting materials for thermochemical storage applications. However, these systems often have to work at relatively high pressure and the storage of  $\text{H}_2$  is still a matter of concern, even though the use of low temperature metal hydrides seems to be a promising strategy. Moreover, as these systems work in closed conditions, the indirect path of heat transfer (solid/wall) strongly limits the global performances.

#### **I.4.2 Hydroxides**

Metal hydroxides are an interesting class of materials for thermochemical storage. When heated to an appropriate temperature, water (steam) is released following an endothermic reaction, while the metal hydroxide is converted into the corresponding metal oxide. As water is a harmless gas, it can be released to the atmosphere without almost any concerning: open chemical storage systems can then be easily conceived. The two key parameters for these systems are the reaction temperature and the water partial pressure, which are thermodynamically related by Eq. I.6:

$$P_{\text{H}_2\text{O}} = P_0 \exp\left(\frac{-\Delta G}{RT}\right) = P_0 \exp\left(\frac{-\Delta H}{R} \frac{1}{T} + \frac{\Delta S}{R}\right) \quad (\text{I.6})$$

where  $P_0 = 1.013 \cdot 10^5 \text{ Pa}$ ,  $P_{\text{H}_2\text{O}}$  is the water vapour pressure and  $T$  the reaction temperature. The plot of Eq. I.6 for some metal hydroxides is reported in Figure I.10.

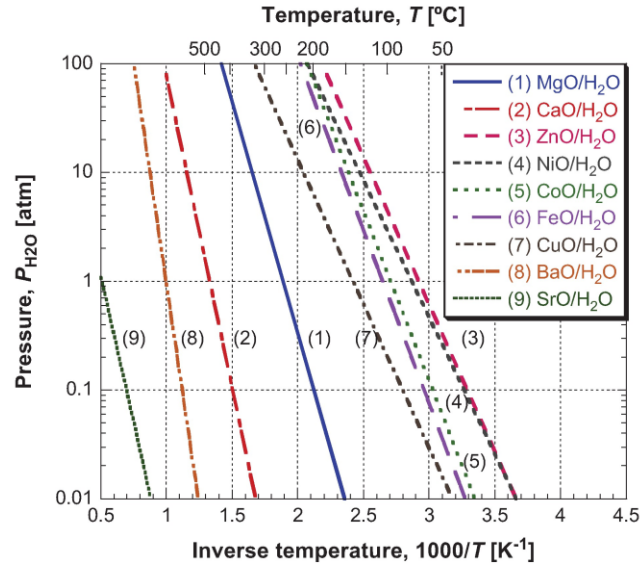


**Figure I.10:** Equilibrium correlation for some metal oxide/water reactions (*Kato et al.*, 2009).

It is possible to observe that many metal hydroxides decompose at relatively low temperatures. Hydroxides of the alkali metal group are not reported in the graph, but according to some authors all of them react in liquid state and only LiOH has been described as an interesting material for thermochemical storage (*Felderhoff et al.*, 2013). If high-grade heat needs to be produced, the more interesting compounds appear to be the alkaline-earth metal hydroxides, which react according to the following scheme:



The basic strength of an alkaline-earth metal hydroxide is lower than that of the corresponding alkali metal of the same period, and it increases when moving down a group: while  $Be(OH)_2$  is an amphoteric compound,  $Ba(OH)_2$  is as strong as an alkali metal hydroxide. The basic strength should not be neglected when dealing with metal hydroxides, as special attention could be required in the choice of the reactor materials. It is also important to underline that, in order to obtain a good heat storage efficiency, it is of fundamental importance to recover the latent heat of the steam produced during the decomposition reaction (at least in some extent), as it represents a relevant fraction of the total energy (nearly 50% for  $Mg(OH)_2$  and 33% for  $Ca(OH)_2$  case).

Among the alkaline-earth metal hydroxides, two systems are mainly studied in the literature:  $Mg(OH)_2/MgO$  and  $Ca(OH)_2/CaO$ . Their main thermodynamic parameters are reported in Table I.3.

Reaction	$T_{eq, 1 \text{ bar}}$ [K]	$T_{exothermic}$ [K]	$T_{endothermic}$ [K]	$\Delta^R H$ [kJ mol <sup>-1</sup> ]
$CaO_s/Ca(OH)_2$	752	675	800	109
$MgO_s/Mg(OH)_2$	531	450	550	81

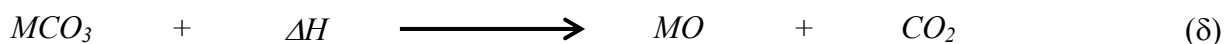
**Table I.3:** Main thermodynamic parameters for the  $Mg(OH)_2/MgO$  and  $Ca(OH)_2/CaO$  systems.

*Ervin* (1977) was one of the first to study both the  $Mg(OH)_2$  and  $Ca(OH)_2$  systems, highlighting their main advantages and drawbacks. A first important evidence he claimed was the need to use pure steam in order to obtain a rapid hydration. A different behaviour toward hydration was also highlighted:  $MgO$  was found to be inert to hydration in highly superheated steam, while  $CaO$  was

able to hydrate rapidly also at temperature very close to the equilibrium value. Concerning the cycling stability, *Ervin* reported for both systems a good behaviour, achieving 500 cycles for  $\text{Mg}(\text{OH})_2$  and 211 cycles for  $\text{Ca}(\text{OH})_2$ . For the former, the reaction yield decreased from 95% to 60–70% after the first 40 cycles, and then kept constant. Differently, for  $\text{Ca}(\text{OH})_2$  the reaction yields remained constantly equal to 95%, although the reaction rates decreased progressively during the cycles. From its preliminary test, *Ervin* concluded that  $\text{CaO}$  was a better material than  $\text{MgO}$ , thanks to its higher energy density storage, higher working temperature and lower price. The  $\text{Ca}(\text{OH})_2/\text{CaO}$  reaction was also studied by *Schaube* and co-workers (2012) in TGA experiments with high  $\text{H}_2\text{O}$  partial pressure. Data of heat capacity, thermodynamic equilibrium, reaction enthalpy and kinetics were collected and kinetic expressions were derived. The authors also confirmed the good cycling stability of the material achieving more than 100 cycling tests. In another work, *Schaube* and co-authors (2013) tested the  $\text{Ca}(\text{OH})_2/\text{CaO}$  system in a reactor with direct heat transfer between the gaseous reactant and the solid material, using samples of about 60 g. Working in fixed bed conditions and with a fine material ( $d_{50}=5.25 \mu\text{m}$ ), they again proved the good cycling stability of the material but also highlighted a tendency towards agglomeration. Experimental tests with greater amount of material were instead performed by *Schmidt* and co-workers (2014) in an indirectly operated reactor based on a plate heat exchanger concept. They worked with 20 kg of material achieving several hydration/dehydration cycles without degradation of the material performance. However, they experienced a material conversion of 77%, quite lower than the values obtained by other authors, which was explained through a slight material carbonization during handling operations. Tests for the  $\text{Ca}(\text{OH})_2/\text{CaO}$  system in a fluidized bed reactor were instead performed by *Pardo* and co-workers (2014a). They worked in an indirect heating configuration, supplying the heat through electrical resistance fixed to the outlet shell. A fine  $\text{Ca}(\text{OH})_2$  powder with particle diameter of  $4 \mu\text{m}$  was used, and inert easy-to-fluidize particles were added to the sample (70%<sub>wt</sub> of an  $\text{Al}_2\text{O}_3$  powder with  $180 \mu\text{m}$  particle diameter) to achieve a good fluidization. The decomposition reaction was performed at 460–480 °C while the hydration at 350–380 °C with a  $\text{H}_2\text{O}$  partial pressure of 31.1 kPa (and a total pressure of 134 kPa). The material was tested for 50 cycles, with a mean conversion of 80%: 50 min were required to accomplish the decomposition step and 28 min were required for the hydration step. The energy density value estimated by the author was  $60 \text{ kWh m}^{-3}$  if the mixture with the  $\text{Al}_2\text{O}_3$  was considered, thus only 10% of the theoretical value. This value was found to increase up to  $156 \text{ kWh m}^{-3}$  if a solid separation between inert and  $\text{CaO}$  was performed, although evaluation on the energy required to separate the two materials was not accomplished.

### **I.4.3 Carbonates**

This class of material is quite similar to the hydroxide one. The main difference is that the working gas is  $\text{CO}_2$  instead of  $\text{H}_2\text{O}$ . The general reaction is:



The decomposition reaction, generally referred as calcination, is a heavily endothermic reaction. The two key parameters for these processes are the  $\text{CO}_2$  partial pressure and the temperature of the system. Compared to metal hydroxides, metals carbonates generally feature higher decomposition temperatures and enthalpies of reaction. One major problem is related to the storage of the  $\text{CO}_2$

produced during the decomposition step. Liquefaction by compression leads to loss of energy, thus alternative strategies involving the capture on appropriate adsorbents or on metal oxides are currently investigated (*Felderhoff et al.*, 2013). Carbonates of alkali and alkaline-earth metals become more stable moving down a group: both the temperature required for the decomposition reaction and the reaction enthalpy increase. An explanation for this trend can be found in the polarizing effect of the metal cation: going down a group the charge density of the cation decreases due to the increase in the atomic radius, hence the carbonate ion becomes less polarized. The lower polarized the carbonate ion, the lower the carbon dioxide tendency to break free and leave the metal oxide. On the contrary, a high polarization of the chemical bond will promote CO<sub>2</sub> release. This explanation also accounts for the higher stability of the alkaline carbonates with respect to the correspondent alkaline-earth ones (alkaline ions own indeed a lower charge and a coarser diameter). A plot reporting the decomposition enthalpy values for several metal carbonates is reported in Figure I.11. Taking into account Eq. I.5 and by further considering that the  $\Delta S$  values are nearly the same for all the carbonate decompositions (as they primarily arise from the formation of a gaseous product), the trend highlighted in Figure I.11 can be considered approximately valid also for the decomposition temperature of the compounds.

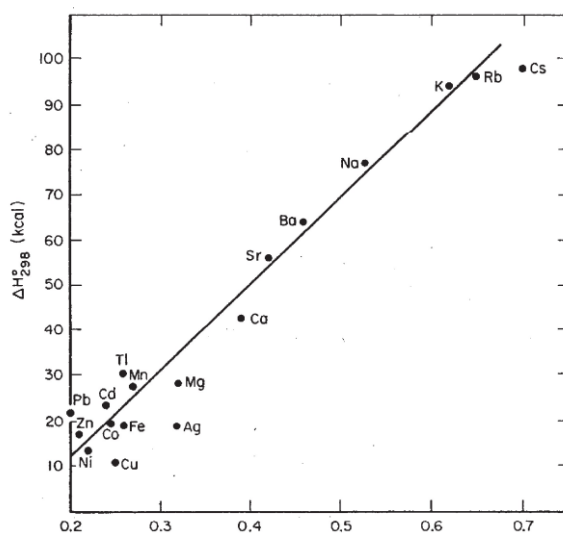


**Figure I.11:** Decomposition enthalpies as a function of cation  $r^{1/2}/Z^*$ .  $r$  is the cation radius and  $Z^*$  the effective nuclear charge as calculated from Slater's rule (*Stern and Weise*, 1969).

Among the alkaline carbonates, only the lithium one can be decomposed at Bunsen temperatures (1000–1400 °C) while the other ones require higher temperatures and melt before a full decomposition could occur. Calcination/carbonation reactions are instead possible for MgCO<sub>3</sub> and CaCO<sub>3</sub>. SrCO<sub>3</sub> decomposes at reasonable yield only at temperatures above 1000 °C, but it is also reported a considerable sintering before the decomposition is accomplished (*Glasson and Sheppard*, 2007). The most studied carbonate compound for thermochemical storage is calcium carbonate (CaCO<sub>3</sub>), which is found in nature as calcite or aragonite. It reacts according to the following reaction:



The working temperature ranges between 700 and 1000 °C with CO<sub>2</sub> partial pressures between 0 and 10 bar. The storage capacity of the solid is 0.6 kWh kg<sup>-1</sup> and 670 kWh m<sup>-3</sup> (50% of porosity). Experimental tests performed with particles of 10 μm highlighted the formation, during the carbonation, of a passivation layer that leads to reaction limitation by decreasing the CO<sub>2</sub> diffusion. Submicron particles have been tested to reduce this phenomenon and even though the increase in reactivity was high, the volumetric energetic density of the material does not exceed 10% of the theoretical value due to the strong diminution of the bulk density (*Pardo et al.*, 2014b). Several works can be found in the literature which are mainly focused on the use of the solar energy to perform the calcination reaction. *Meier* and co-workers (2004) developed and tested a 10 kW rotary kiln calcination reactor. Using limestone particles of 1–5 mm, they obtained a highly calcined product (>95%) and a thermal efficiency of 20%. Other tests on the CaCO<sub>3</sub> calcination were performed by *Flamant* and co-workers (1980) in a small fluidized bed directly irradiated through a transparent wall. They achieved a thermal efficiency of 20% for a partial 80% decarbonation of the material and of 10–15% for a complete decarbonation. *Aihara* and co-workers (2001) tried to improve the reversibility of the calcination reaction by doping the material with an inert framework of titanium oxide (CaTiO<sub>3</sub>). By using TGA experiments, they showed a stabilization of the reaction reversibility, and were able to perform 10 cycles at 1023 K without the insurgence of sintering phenomena. They claimed that the addition of an inert material with a high melting-point is effective in the improvement of the reversibility of the cyclic reaction through a diminution of the sintering phenomena. Further, the carbonation/calcination reactions of CaCO<sub>3</sub> have been widely investigated in the last years in carbon capture and sequestration technologies. Thus, several experimental feedbacks can be found in the literature even though most of the performed experiments do not deal with the use of solar reactors. CaCO<sub>3</sub> is a very interesting material for thermochemical storage. The theoretical energy density is high, and the raw material is cheap because it is one of the most abundant compounds on Earth. Its main drawbacks are related to agglomeration and sintering phenomena, to a not high reactivity and to a need of CO<sub>2</sub> storage.

#### **I.4.4 Oxides**

Metal oxides are an interesting class of materials, too. The general reaction scheme is:



Air can be used as heat transfer fluid and reactant for both the forward and backward reaction. Unlike the other so far discussed metal oxide systems, there is no need to separate or condense the gas obtained from the decomposition step, as a simple O<sub>2</sub>-rich or O<sub>2</sub>-lean air stream is produced. An extensive screening work concerning the thermochemical storage capabilities of these materials was done by the General Atomics in collaboration with the German Aerospace Center (*Wong*, 2011). They identified Co<sub>3</sub>O<sub>4</sub> and Mn<sub>2</sub>O<sub>3</sub> as the most interesting systems as characterized by a good combination of properties such as interesting working temperatures (800–1000 °C) and accessible costs. The Co<sub>3</sub>O<sub>4</sub>/CoO system is an interesting redox couple with an high storage energy density (~200 kJ mol<sup>-1</sup>). It has been intensively studied at the German Aerospace Center in both pure form (*Agrafiotis et al.*, 2014a) and with dopant incorporation (*Block et al.*, 2014). By performing tests in TGA analysis, it was shown that Co<sub>3</sub>O<sub>4</sub> can operate in a cyclic mode within the temperature range 800–1000 °C. It was also highlighted that the re-oxidation step is slower than the reduction step and

a narrowing of the operation temperature range was suggested to reduce the kinetics difference. Concerning the dopant incorporation, it was shown that the use of iron oxide dopant can increase the microstructural stability, but the reaction enthalpies linearly decrease with the iron oxide content. Mixtures with low dopant incorporation are suggested in order to keep the reaction enthalpies to large values and to benefit of a superior reaction reversibility. *Carrillo* and co-workers (2014) performed experiments on Mn and Co pure and mixed oxides. They reported a worsening of the performance for both materials when mixed oxides were considered, as the cyclability and the kinetics of the mixed oxides were never as good as the ones of pure compounds. Moreover, they also stated that even though the reaction enthalpy of the  $\text{Mn}_2\text{O}_3/\text{Mn}_3\text{O}_4$  redox couple is far lower than that of the  $\text{Co}_3\text{O}_4/\text{CoO}$  one,  $\text{Mn}_2\text{O}_3$  can benefit of an excellent cycling stability, a low toxicity ( $\text{CoO}_3$  is a suspicious carcinogenic material) and a far lower cost which makes it a good candidate for thermochemical storage applications. A 100 Wh particle-based reactor is under development to study the thermochemical heat storage performance of  $\text{Mn}_2\text{O}_3$  (*Álvarez de Miguel et al.*, 2014). Experimental tests on  $\text{CuO}/\text{Cu}_2\text{O}$  were instead performed by *Alonso* and co-workers (*Alonso et al.*, 2015) in a solar rotary kiln under both argon and air atmosphere. A strong temperature control is required as the melting point of  $\text{Cu}_2\text{O}$  ( $\sim 1230$  °C) is near to the working reduction temperature ( $\sim 1000$  °C). The authors obtained a good conversion in Ar atmosphere, but observed a severe coalescence of the particles which affected the subsequent oxidation step when performing the test in air.

#### **1.4.5 Solar Fuels Production**

The thermochemical storage processes described so far are mainly intended for a local energy storage, as the energy is mostly recovered in the same plant in which it is stored. However, as previously mentioned, thermochemical energy storage processes can also be applied to synthesize solar fuels, which can then be not only used in the production site but also transported in different location, so as to take advantage from the solar energy in places where a CSP plant could not be built. Two main strategies for solar fuel generation can be clearly distinguished.

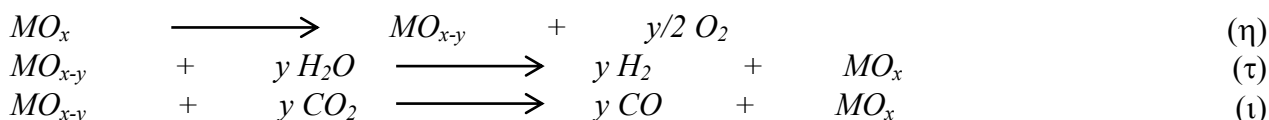
The first strategy is aimed at upgrading the potentialities of existing fuels, fossil and non, through cracking, gasification and reforming processes (*Yadav and Banerjee*, 2016). Several experimental and modelistic works can be found in the literature on  $\text{CO}_2/\text{H}_2\text{O}$  gasification of coal/coal cokes in fluidized bed reactors (*von Zedtwitz and Steinfeld*, 2005; *von Zedtwitz et al.*, 2007; *Gokon et al.*, 2012; *Kodama et al.*, 2002; *Gokon et al.*, 2015a), steam gasification of charcoal (*Müller et al.*, 2003), solar methane reforming (*Agrafiotis et al.*, 2014b) and biomass char steam gasification (*Gordillo and Belghit*, 2011). More ambitious processes are instead devoted to the production of liquid fuels through the combination of a Fischer-Tropsch process with lignite gasification (*Guo et al.*, 2015) or to the production of liquid fuels together with electricity by solar gasification of coal (*Kaniyal et al.*, 2013).

The second strategy for solar fuels production is instead targeted at the obtainment of  $\text{H}_2$  or CO through the splitting of  $\text{H}_2\text{O}$  or  $\text{CO}_2$  molecules, namely at the conversion of inherently cheap materials into high-value fuels. This is an ambitious and complex process: the direct thermolysis is not a viable route, as it requires temperatures in the order of 4330 K for  $\text{H}_2\text{O}$  and of 2700 K for  $\text{CO}_2$ . Moreover, a concomitant production of  $\text{H}_2$  and  $\text{O}_2$  at high temperatures would give rise to the formation of an explosive mixture. Thermochemical multi-step splitting cycles have been proposed with the aim of both reducing the high required temperature and producing the two gases ( $\text{H}_2/\text{CO}$

and O<sub>2</sub>) in distinct environments. Several authors have screened different cycles during last years in order to identify the more promising and reliable ones (*Abanades et al.*, 2006; *Kodama and Gokon*, 2007) and several update comprehensive reviews can be found in the literature (*Scheffe and Steinfeld*, 2014; *Yadav and Banerjee*, 2016). Cycles composed of more than two steps can be performed at lower temperatures but, at the same time, an increased number of operations easily brings to lower global efficiencies: two and three-step cycles are then the more realistic candidates.

Three-step cycles can decompose H<sub>2</sub>O at temperatures ranging in the 298–1000 K interval, which is not possible for the two-step cycles due to thermodynamic limitations. However, the three-step cycles described in the literature make use of complicated processes for practical solar application (e.g., chemical and electrochemical reaction in the same cycle) and most of them also use corrosive reactants like strong acids (e.g., H<sub>2</sub>SO<sub>4</sub>, HCl) or strong bases (e.g., NaOH) that would result in a difficult and expensive reactor construction (*Kodama and Gokon*, 2007; *Charvin et al.*, 2007a).

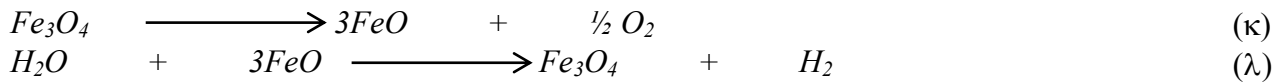
Two-step thermochemical cycles that make use of metal oxide redox pair are the more investigated processes in the literature. The chemical reactions involved in such cycles are:



The first step consists in a reduction of the metal oxide accomplished by the only use of heat: a metal oxide in a high oxidation status is hence reduced to a lower valence status ( $y < x$ ) or to the pure metal form ( $y = x$ ) while O<sub>2</sub> is released. In the second step, the reduced metal oxide reacts with H<sub>2</sub>O to produce H<sub>2</sub> and regenerate the initial metal oxide according to the reaction (θ), or, alternatively, with CO<sub>2</sub> to produce CO according to the reaction (i). It is easily to recognize that the sum of the reaction (η) and (θ), or (η) and (i), gives rise to the “pure” splitting of the H<sub>2</sub>O or CO<sub>2</sub> molecule: the metal oxide actually works as a catalyst. The first reaction is generally referred as Thermal Decomposition (TD) or Thermal Reduction (TR) step: it is strongly endothermic and requires high temperatures. The second reaction is instead generally referred as re-oxidation or, if performed with H<sub>2</sub>O, Water Decomposition (WD) step: it is slightly exothermic and can be performed at lower temperatures. The choice of the redox pair is obviously crucial for the success of the process. The metal oxide, in its oxidized form, should have an accessible reduction temperature (i.e., not too high) while, at the same time, the reduced form of the metal oxide should be able to react with H<sub>2</sub>O or CO<sub>2</sub> at an acceptable temperature (i.e., not too low). As the reoxidation step is exothermic, if the Δ*G* of the reaction equals zero at too low temperatures, it would be difficult or impossible to perform the reaction with satisfactory kinetic rates. Several evaluated metal oxide systems (Mn<sub>3</sub>O<sub>4</sub>/MnO, Co<sub>3</sub>O<sub>4</sub>/CoO, Nb<sub>2</sub>O<sub>5</sub>/NbO<sub>2</sub>, CdO/Cd, WO<sub>3</sub>/W) were rejected because one of the two temperatures was not accessible (*Kodama*, 2003; *Kodama and Gokon*, 2007). Some of the more interesting metal oxide systems will be briefly described in the following.

#### 1.4.5.1 Fe<sub>3</sub>O<sub>4</sub>/FeO and Ferrites

One of the first studied metal oxide system is the one based on the Fe<sub>3</sub>O<sub>4</sub>/FeO redox pair which involves, for the H<sub>2</sub>O splitting, the two following reactions:



Negative values of  $\Delta G$  are obtained at temperatures above 2500 K and under 1000 K for the two reactions at a pressure of 1 bar (Kodama, 2003). Melting points of  $\text{Fe}_3\text{O}_4$  and  $\text{FeO}$  are, respectively, 1600 °C and 1400 °C and these values should not be exceeded in order to avoid the use of quenching operation that would result in high energy losses. Charvin and co-workers (2007b) investigated the  $\text{Fe}_3\text{O}_4/\text{FeO}$  cycle for  $\text{H}_2\text{O}$  splitting. They performed the TR step with small quantities of sample in a solar furnace under a continuous flow of  $\text{N}_2$ , reaching chemical conversions above 90% at a temperature of 1700 °C. Melting of the sample was observed but without relevant losses due to metal volatilization.  $\text{H}_2\text{O}$  splitting tests performed in a fixed bed electrically heated in the 480–675 °C range, after the milling of the sample, showed re-oxidation conversions up to 80%. On the other side, Abanades and Villafan-Vidales (2013) tested the  $\text{Fe}_3\text{O}_4/\text{FeO}$  redox couple for  $\text{CO}_2$  splitting. TR was achieved in a solar furnace, while re-oxidation tests were performed both in isothermal (600–800 °C) and dynamic Thermal Gravimetric Analysis (TGA) apparatuses with different inlet  $\text{CO}_2$  mole fractions. The re-oxidation reaction appeared to be very temperature-dependent, as both the kinetics and the chemical conversion increased with the temperature. A maximum re-oxidation yield of 95% was obtained in dynamic TGA. The authors also highlighted that elemental C was not formed during the re-oxidation step. In order to reduce the temperature required for the TR step, solid solutions between  $\text{Fe}_3\text{O}_4$  and  $\text{M}_3\text{O}_4$  (M=Mn, Ni, Co) have been proposed, with the intent of combining the good  $\text{H}_2$  yield of the  $\text{Fe}_3\text{O}_4$  system with the lower reduction temperature of some  $\text{M}_3\text{O}_4$  systems. Partial substitution of the iron in the  $\text{Fe}_3\text{O}_4$  by Mn, Co, Mg, Ni is possible to form mixed metal oxides  $(\text{Fe}_{1-x}\text{M}_x)_3\text{O}_4$ , compounds generally known as ferrites. Moreover the use of an inert support, like *m*- $\text{ZrO}_2$ , has been proposed to reduce the deactivation caused by sintering phenomena. On this topic, Kodama and co-workers (2005) studied Co(II) ferrites supported on *m*- $\text{ZrO}_2$  for  $\text{H}_2\text{O}$  splitting. TR experiments were performed at 1400 °C under a flow of  $\text{N}_2$  in an IR furnace, while WD in a small packed bed at 1000 °C under a flow of  $\text{H}_2\text{O-N}_2$  (47%  $\text{H}_2\text{O}$  content). A higher reactivity in terms of kinetics, chemical conversion and cycling stability was claimed by the authors for the supported ferrite, with conversion values between 40 and 60% among six cycles. The role of the *m*- $\text{ZrO}_2$  support in alleviating sintering phenomena was further confirmed by tests performed with unsupported sample. Lower reduction temperatures (1300 °C) were also tested, obtaining poor reduction yields. In a different work, Ni(II) ferrites supported on *m*- $\text{ZrO}_2$  were tested (Kodama *et al.*, 2008). Reduction yields ranging from 60 to 80% with good cycling stability were obtained for samples of  $\text{NiFe}_2\text{O}_4/m\text{-ZrO}_2$  with a loading of 20%<sub>wt</sub>. The authors tested this material in a small fluidized bed reactor conceived to work in CSP mode with beam down optics (Gokon *et al.*, 2011). The reactor was made of stainless steel and had a central Inconel draft tube located inside the fluidized bed region. By repartitioning the gas flow rate between the inside and the outside of the tube, the authors forced the particles to move upwards in the draft tube and downwards in the annulus regions of the bed, highly enhancing the axial heat transfer coefficient. A window was installed in the ceiling of the reactor to let the solar radiation enter, simulated by an array of 3 Xe-lamps of 6 kW each: peak and average flux densities were, respectively, 2500 and 1500  $\text{kW m}^{-2}$  at full power. A scheme of the reactor use by Gokon and co-workers is reported in Figure I.12.

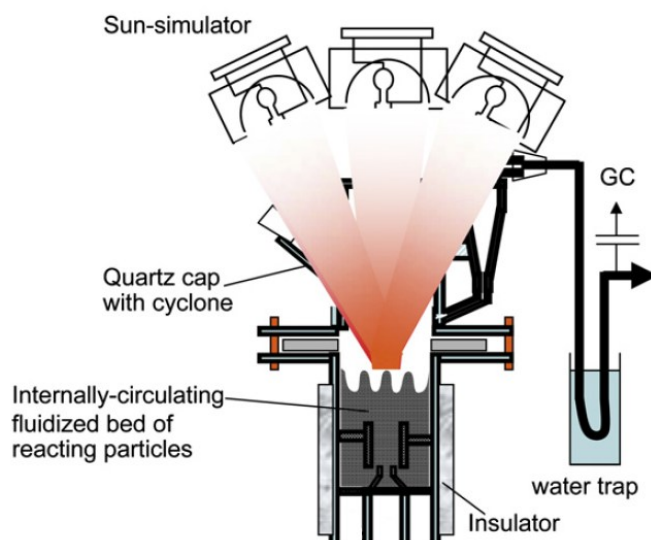
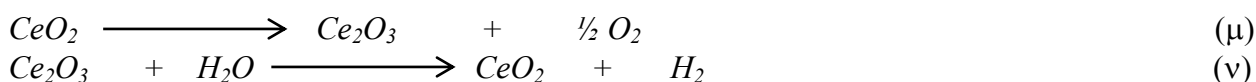


**Figure I.12:** Scheme of the fluidized bed reactor used by *Gokon* and co-workers (2011) for the  $\text{H}_2\text{O}$  splitting test with  $\text{NiFe}_2\text{O}_4/m\text{-ZrO}_2$  particles.

The reactor was used for both the TR and the WD step by switching the fluidizing gas: pure  $\text{N}_2$  for TR and a mixture of  $\text{H}_2\text{O}:\text{N}_2$  (50–80% of  $\text{H}_2\text{O}$ ) for WD. An irradiation time of 15 min at an estimated thermal power of 2.4 kW was used for TR, obtaining temperatures at the surface of nearly  $1550\text{ }^\circ\text{C}$  in the draft tube zone and of  $1150\text{ }^\circ\text{C}$  in the annulus region. A lower thermal power of 1.6 kW was used for the WD step, but reaction times of 90 min were required, highlighting a slow kinetics of the material. The obtained reduction yields (40%) were far lower than the one achieved in small scale (70%) and the estimated energetic efficiencies were very low ( $\sim 1\%$ ). Such low efficiency values were partially explained because of an insufficient thermal insulation and a too long reaction time for the WD step.

#### I.4.5.2 $\text{CeO}_2/\text{Ce}_2\text{O}_3$

The cerium oxide cycle is a relatively novel two-step cycle based on the two following reactions:



Melting points are of nearly  $1700\text{ }^\circ\text{C}$  for  $\text{Ce}_2\text{O}_3$  and  $1950\text{ }^\circ\text{C}$  for  $\text{CeO}_2$ . *Abanades and Flamant* (2006) were the firsts authors to suggest the use of  $\text{Ce}_2\text{O}_3$  as metal oxide for thermochemical splitting cycles. They performed the TR of pure  $\text{Ce}_2\text{O}_3$  in a solar furnace under a continuous flow of  $\text{N}_2$  at reduced pressure (100–200 mbar), obtaining a nearly complete reduction but with a relevant sublimation of the sample. Subsequent WD was accomplished in an electrically heated fixed bed reactor with excellent re-oxidation kinetics. With the aim of reducing the temperature required for the TR step, the possibility of using mixed cerium oxides was investigated (*Abanades et al.*, 2010). The addition of many metal oxides (Al, Mn, Fe, Co, Cu, Zn) did not produce improvements and only the Zr solid solution brought to some advantages in the TR step. However, authors found that even though the TR step with the Ce-Zr solid solution could be performed at lower temperatures, the re-oxidation step was strongly penalized, with higher required temperature and slow reaction

kinetics. The importance of the synthesis route in Zr-doped ceria samples was highlighted too, as it determines the morphology of the powders and their resistance toward sintering (*Le Gal et al.*, 2011). A slight improvement in long-term cycling was observed by *Call* and co-workers (2015) adding small quantities of Lanthanide oxides to the Zr-doped ceria samples. The  $\text{CeO}_2/\text{Ce}_2\text{O}_3$  metal oxide system was also studied by *Gokon* and co-workers (2013), which tested  $\text{CeO}_2/\text{Ce}_2\text{O}_3$  in the  $\text{H}_2\text{O}$  splitting cycle and compared the performance with the ones of  $\text{NiFe}_2\text{O}_4/m\text{-ZrO}_2$  systems. The authors highlighted a good sintering resistance of the  $\text{CeO}_2$  sample, a fast re-oxidation kinetics and an excellent stability upon repeated cycles. In terms of  $\text{H}_2$  produced, the amount obtained using  $\text{NiFe}_2\text{O}_4/m\text{-ZrO}_2$  was slightly higher but with far slower kinetics. Authors recognized  $\text{CeO}_2$  as a promising redox material for thermochemical two-step water splitting. *Gokon* and co-workers (2015b) also tested several doped cerium oxides (5–15% mol content) in the water splitting cycle. They stated that a low content of Fe or Mn dopant (5% mol) can enhance the produced  $\text{H}_2$  quantities if working at higher re-oxidation temperature and steam partial pressure. On the contrary, larger dopant quantities always brought to a too slow re-oxidation rate. Cerium oxide was tested for  $\text{H}_2\text{O}$  and  $\text{CO}_2$  splitting by *Chueh* and co-workers (2010) in a solar reactor subjected to concentrated radiation under realistic operating conditions relevant to large-scale industrial implementation. The reactor was a cavity receiver with a windowed aperture through which concentrated solar radiation could enter (Figure I.13). A monolithic cylindrical structure of cerium oxide with a porosity of 80% was synthesized by the authors and positioned inside the reactor. The incident solar radiation was characterized by a mean flux of  $1500 \text{ kW m}^{-2}$  and a total thermal power of 1.9 kW. The temperature of the ceria cylinder ranged between  $1420 \text{ }^\circ\text{C}$  and  $1620 \text{ }^\circ\text{C}$  during the TR. No carbonaceous species were deposited during the  $\text{CO}_2$  dissociation, thus a selectivity toward CO production of 100% was obtained. A faster rate of fuel production with respect to that of  $\text{O}_2$  release was observed and this was attributed to a limited heating rate. Efficiency factors lower than 1% were estimated by taking into account the fuel produced, the incident energy and the energy needed to produce the inert gas. The high cycling material stability was confirmed performing more than 500 cycles in a differential reactor system. A 3D model to study the reactor performance, together with an analysis targeted at improving the geometrical design of the reactor, has also been presented (*Furler and Steinfeld*, 2015).

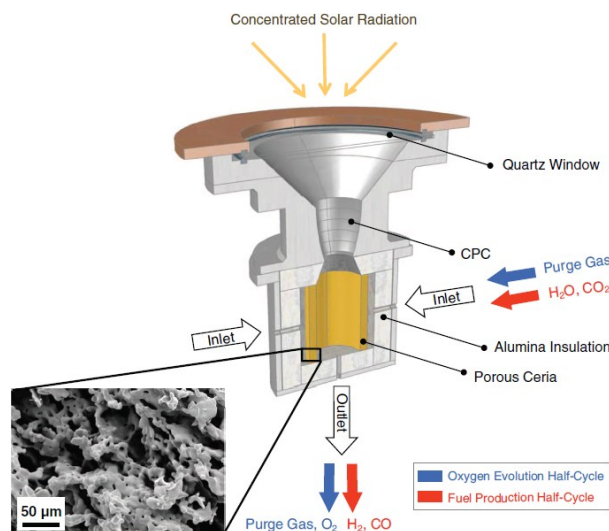
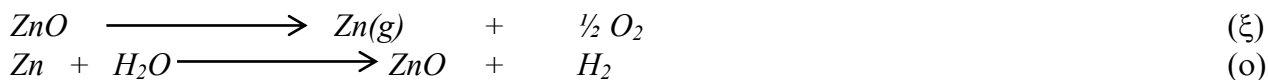


**Figure I.13:** Scheme of the cavity receiver reactor tested by *Chueh* and co-workers (2010).

### 1.4.5.3 ZnO/Zn

The ZnO/Zn system is another potential candidate for thermochemical splitting cycles and has been widely studied at the Paul Scherrer Institute (PSI). The two reactions involved, referred to the H<sub>2</sub>O decomposition, are the following:



$\Delta G^0$  of thermal decomposition reaction equals zero at about 2200 K and the reaction proceeds at reasonable rates starting from 2000 K. Numerical analyses in realistic process conditions were performed to estimate the maximum solar-to-chemical energy conversion efficiencies of this cycle, and results showed values of 35% for H<sub>2</sub>O and 39% for CO<sub>2</sub> splitting (*Loutzenhiser et al.*, 2010). As the zinc boiling point is relatively low (~1200 K), Zn is present in the vapour phase after the TR step. A separation step at high temperature or a quenching of the products is then needed to avoid the recombination reaction (*Müller and Steinfeld*, 2008). Several reactor configuration for the TR step were experimentally examined, like entrained flows, packed beds, and a rotating cavity receiver. A vortex-flow solar reactor was designed and built at PSI to decompose ZnO particles into Zn and O<sub>2</sub>: ZnO is directly exposed to the high-flux solar irradiation and acts as radiant absorber, thermal insulator and chemical reactor simultaneously (*Steinfeld and Meier*, 2004). With respect to the oxidation step, analysis demonstrates that faster reaction rates and greater conversions are obtained above the Zn melting point (693 K). Reactions mechanism for both CO<sub>2</sub> and H<sub>2</sub>O showed a fast interface-controlled regime followed by a transition to a slow diffusion-controlled regime, limited by the Zn ion migration across the ZnO surface layer.

### 1.4.5.4 Perovskites

Another interesting class of materials which is being intensively studied in the last three/five years is that of the nonstoichiometric perovskite oxides (ABO<sub>3-δ</sub>). According to the first collected experimental and modelistic data, this class of non-volatile oxides shows good potentialities concerning the thermochemical splitting of H<sub>2</sub>O or CO<sub>2</sub>. *Scheffe* and co-workers (2013) investigated the performance of lanthanum-based perovskites corresponding to the La<sub>1-x</sub>Sr<sub>x</sub>MnO<sub>3-δ</sub> general formula. They found that such compounds can be reduced to a greater extent with respect to ceria oxides under the same reaction conditions. More specifically, at reduction temperatures of 1600 K, six times larger O<sub>2</sub> release yields can be obtained, while the increase is reduced down to twice when temperatures as high as 1800 K are considered. However, the authors also highlighted that the investigated compounds require quite low temperatures (~400 K) in order to obtain a good re-oxidation yield, and this is a relevant drawback as the redox cycle would involve two steps performed at far different temperatures. The authors also noticed that higher re-oxidation yields at higher temperature could be obtained increasing the steam concentration during the re-oxidation step, but an important heat recuperation system of the excess heat would then be required. *McDaniel* and co-authors (2013) instead studied the performance toward H<sub>2</sub>O and CO<sub>2</sub> splitting of Sr- and Mn- doped LaAlO<sub>3-δ</sub> perovskite compounds synthesized through a modified Pechini method. Performing the redox cycle at a reduction temperature of 1350 °C and at an oxidation temperature of 1000 °C they measured nine times larger yields for H<sub>2</sub> splitting (and six times larger for CO<sub>2</sub>) with respect to cerium oxides. However they underlined that in their reactor the H<sub>2</sub>O/H<sub>2</sub> or

CO<sub>2</sub>/CO ratio was always greater than 100 thanks to a constant flow of H<sub>2</sub>O or CO<sub>2</sub> that swept away the product gases, confirming the importance for these compounds of large steam/CO<sub>2</sub> concentrations and the consequent essential relevance of heat recovery. An important durability test was also performed, showing a stable CO production over 80 reaction cycles. The versatility of perovskite structured materials is by far higher than that of cerium oxides or ferrite based compounds. A first degree of freedom is given by the choice of the A and B cations which form the basic structure of the perovskite oxide. Further, dopants can be substituted on both the A and B cation sites and this opens an extremely wide composition space. Several works can already be found in the literature with different cations and dopant incorporation (*Demont et al.*, 2014; *Jiang et al.*, 2014; *Demont and Abanades*, 2015; *Babiniec et al.*, 2015). The research is highly active for the synthesis of materials that could lead the solar fuels production toward an economic viable route.

## I.5 The Role of Fluidized Bed as Solar Thermal Receiver

A critical point of CSP systems is the development of the receiver, as it owns the crucial task of collecting and transferring all the received solar energy. A good receiver should ensure the lowest possible heat losses and minimize the local overheating, so as to avoid the thermal stresses that could lead to irreversible modifications in the chemical/physical properties of the process materials. The global efficiency of a CSP plant is highly dependent on the receiver performance, as it affects all the successive steps of the process. Gas–solid fluidized bed systems have been proposed as convenient tools for the development of solar receivers thanks to their large heat transfer coefficients (several hundreds of W m<sup>-2</sup> K<sup>-1</sup>) and thermal diffusivities ( $\sim 10^{-2}$  m<sup>2</sup> s<sup>-1</sup>), associated with convective transfer due to bubble-induced and/or gulfstream motion of fluidized solids (*Borodulya et al.*, 1982; *Bachovchin et al.*, 1983; *Aprea et al.*, 2013; *Solimene et al.*, 2014). Moreover, gas–solid fluidized bed can be easily integrated with thermo-chemical processes (*Angrisani et al.*, 2013). Different configurations can be considered as regards the interaction between the incident radiative flux and the fluidized bed.

Indirect heating is accomplished by focusing solar radiation onto a cavity or an exposed surface whence heat is transferred to the fluidized bed. This heating configuration is inherently simple, but possible uneven irradiation on temperature-sensitive surfaces may lead to exceedingly large local radiative fluxes, overheating and unacceptable thermo-mechanical stresses acting on the solar irradiated wall of the reactor. Different concepts of indirectly-heated dense gas–solid fluidized bed receivers have been recently proposed. *Chirone* and co-workers (2013) and *Salatino* and co-workers (2016) documented the use of unevenly and unsteadily fluidized beds accomplishing three basic tasks: 1) collection of concentrated solar radiation; 2) thermal energy transfer to end-use; 3) thermal energy storage. This concept led to the successful demonstration of a 150 kW<sub>th</sub> (peak) solar receiver. An external-circulating dense dual fluidized bed rated at about 150 kW<sub>th</sub> maximum power has instead been developed and demonstrated by *Flamant* and co-workers (2013) and *Benoit* and co-workers (2015). The use of dense particle suspensions as heat transfer fluid was investigated by *Spelling* and co-workers (2015) too. Higher performance in term of both thermal efficiency and energy storage density with respect to conventional molten-salt systems were highlighted by the authors through a detailed techno-economic analysis performed on a 50 MW<sub>el</sub> CSP plant.

An alternative option can be represented by direct irradiation of the fluidized bed through transparent walls or windows (direct heating). Direct absorption of solar energy permits higher

operating temperatures (Alonso and Romero, 2015), hence availability of high-grade thermal energy. Directly-irradiated fluidized bed reactors are very promising in the context of solar chemistry and CSP applications, as they can be operated at process temperatures high enough to perform thermochemical storage with high energy density and production of solar fuels. The key drawback of direct heating across transparent media is the need to keep the medium clean and scratch free, as any deterioration of the medium transmittance drastically reduces the efficiency of the system and increases the medium temperature (Koenigsdorff and Kienzle, 1991; Sasse and Ingel, 1993; Werther et al., 1994). Several studies can be found in literature concerning the direct heating of fluidized beds by high-density radiative flux generated by concentrated solar radiation. In the past, several authors had already recognized fluidized beds as reactors capable of achieving high absorption of the solar energy, large heat transfer coefficients, and easy operation in continuous mode. The performance of packed and fluidized beds as solar receiver were investigated through both experimental tests and modelling approach (Olalde et al., 1980; Flamant, 1982; Flamant and Olalde, 1983; Bachovchin et al., 1983). Comparison between the two modes of operation showed the superior heat distribution of the fluidized bed mode. Through experimental data, the authors highlighted that in order to heat the fluidizing gas at a temperature of 1000 K the surface temperatures of the packed bed were extremely higher than those for the fluidized bed, resulting in four times larger radiation losses. Penetration distances of the solar radiation were experimentally measured, obtaining values equal to 3–15 times the mean particle diameter (250  $\mu\text{m}$ ), where the higher values accounted for the larger inlet gas velocities. Flamant and co-workers (1980) also studied the radiant heat transfer in solar fluidized bed and tested a small fluidized bed reactor (36 mm internal diameter, 300 mm height) made of transparent silica wall to perform  $\text{CaCO}_3$  decarbonization. They highlighted the ability of the fluidizing bed in radially equalizing the received heat, as small radial temperature differences were found despite a Gaussian distribution of the impinging flux in the focal zone. Regarding instead the axial distribution, the existence of three different zones was reported: two at the extremities (i.e., near the distribution grid and near to the upper surface) characterized by a strong thermal gradient, and a central one accounting for 80% of the whole bed characterized by constant temperature and absence of thermal gradient. Thermal efficiencies of 20% were reported for a partial 80% decarbonation of the material, and values of 10–15% for a complete decarbonation. The research on the use of fluidized bed reactors as both solar receiver and solar reactor is highly active at the current days and several works can be found in the international literature (Gokon et al., 2012; Matsubara et al., 2014; Gokon et al., 2015a).

## **I.6 Current CSP Plants in the World**

At the present days, the global capacity of the CSP plant in the world is of approximately 4.4 GW (Figure I.2). Although parabolic trough plants represent the bulk of existing capacity, 2015 was a notable year in terms of CSP technologies diversification. Capacities of newly deployed parabolic- trough and tower plants grew closer (46% for the parabolic trough technology and 41% for the tower technology), while the world's largest linear Fresnel plant (125 MW, 13% of global added capacity) was built in India, further diversifying the mix of added technologies.

One of the world's largest solar power plants (currently the second plant for capacity) is the 354 MW Solar Energy Generating Systems (SEGS) in California. The installation is based on the parabolic trough technology: the concentrated solar energy heats a central tube filled with synthetic

oil whose absorbed heat is used to produce steam, which eventually drives a Rankine cycle steam turbine to generate electricity. The plant is hybridized with natural gas to supply energy if needed during the night or the absence of sunlight (Figure I.14).



**Figure I.14:** The 354 MW SEGS in California.

Several CSP plants are currently operated in Spain, one of the countries with the highest installed capacity. The Solnova Solar Power Station, for example, is a large Spain CSP power station made of 5 separate units of 50 MW (total capacity of 250 MW) and based on the parabolic trough technology. Spain also owns several CSP plants based on solar tower, such as PS10, PS20 and Gemasolar (also known as Solar Tres). The PS20 plant consists of a solar field of nearly 1250 mirrors of 120 m<sup>2</sup> each, which reflects the solar radiation on the top of a 165 m high tower. Steam at high pressure (45 bar) is produced, which is then used to drive a Rankine cycle and produce electricity. The plant has a saturated water thermal storage system with a thermal capacity of 20 MWh rated for 1 hour operation. The nominal capacity of the plant is 20 MW and the capacity factor is of nearly 27%. Its annual energy generation is of approximately 50 GWh. The PS10 plant represents a previous version of PS20, characterized by lower efficiency and thermal storage capacity (Figure I.15).



**Figure I.15:** The PS10 (foreground) and the PS20 (background) Solar Power Plant.

The Gemasolar Thermosolar Plant (Figure I.16), as PS20, is based on the solar tower technology. It consists of nearly 2500 mirrors of 120 m<sup>2</sup> each and has a nominal capacity of 20 MW. The main difference with PS20 is that the Gemasolar plant uses molten salts as both heat transfer fluid and energy storage medium. Thanks to this unique features, the plant can produce electricity for up to 15 h in total absence of light. The capacity factor of the plant, approximately 63%, is considerably higher than the PS20 one. The annual energy generation is of nearly 110 GWh. During summer 2013, the plant was able to operate 24 h per day for 36 consecutive days.



**Figure I.16:** The Gemasolar Thermosolar Plant.

The current world's largest solar power plant is the Ivanpah Solar Power Facility (California), based on the solar tower technology and in operation since February 2014. It deploys 173500 heliostats, each of them hosting 2×15 m<sup>2</sup> mirrors. Each mirror focuses the solar energy on the boilers located on three solar power towers of 130 MW each. The boilers generate high-pressure steam (160 bar) used to drive steam turbines and produce energy through a Rankine cycle. The solar towers are 139 m height. The nominal capacity of the plant is 392 MW and its capacity factor in 2014 was 30% (Figure I.17).



**Figure I.17:** The Ivanpah Solar Power Facility.

The beam down tower technology is still not available at commercial scale, but some demonstrative plants are currently in operation. One of them is the Masdar's beam down optical tower (Figure I.18), made of 33 heliostats of 8.5 m<sup>2</sup> each and arranged in three concentric rings. The ground mirrors reflect the solar radiation onto a central tower 16 m height and with 45 fixed, flat mirrors which reflect the radiation downwards. The plant has a nominal power of 100 kW<sub>th</sub> (Mokhtar *et al.*, 2014).



**Figure I.18:** The Masdar's Beam Down Optical Tower.

Another demonstration plant based on the beam down tower technology is the Solar Thermoelectric Magaldi (STEM) plant, illustrated in Figure I.19. The system is based on an indirectly-heated dense gas–solid fluidized bed receiver designed so as to achieve the three basic tasks of i) collection of concentrated solar radiation; ii) thermal energy transfer to end-use and iii) thermal energy storage. Silica sand is used as solid bed material. The plant is rated for 100 kW<sub>th</sub> and has a daily storage capacity of 4–5 h (Chirone *et al.*, 2013).



**Figure I.19:** The Solar Thermoelectric Magaldi (STEM) Plant, Buccino (Italy).

## I.7 Alternative Strategies for CO<sub>2</sub> Reduction: the Calcium Looping Cycle

On a parallel line, the global warming due to anthropogenic CO<sub>2</sub> emissions is stimulating the development of novel combustion and gasification technologies ready for Carbon Capture and Sequestration (CCS) (Li and Fan, 2008; Boot-Handford et al., 2014). Although the share of renewable energy sources is steadily increasing, current outlooks still foresee extensive use of fossil fuels for many decades. Carbon-free technologies are far from full replacement of fossil fuel combustion (Hoffert et al., 2002; Muradov and Verizoglu, 2008): in the near-to-medium term, authoritative outlooks anticipate a transitional era during which renewable energy sources will co-exist with fossil fuels, and CCS technologies can play an important role in reducing CO<sub>2</sub> emissions. Moreover, countries with large coal reserves could still find the use of gasification/combustion plants coupled with CCS technologies as cost-effective (Viebahn et al., 2007).

One of the most promising CCS technology is the Calcium Looping (CaL) cycle (Figure I.20), based on the alternated temperature-swing uptake (in a carbonator) and concentrated release (in a calciner) of CO<sub>2</sub> from a calcium-based sorbent, most typically limestone due to its abundance in nature and low cost. This technology has reached the maturity of the demonstration stage, and several reviews and studies on this topic can be found in the literature (Blamey et al., 2010; Dean et al., 2011; Dieter et al., 2014; Lisbona et al., 2013; Stanmore and Gilot, 2005; Vorrias et al., 2013; Coppola et al., 2014, 2015). In the carbonator, the CO<sub>2</sub> in the flue gas generated from a combustion plant is captured by CaO at around 650–700 °C following an exothermic reaction. Thus, the carbonator emits a CO<sub>2</sub>-depleted flue gas and a spent sorbent stream consisting of a mixture of CaCO<sub>3</sub> and CaO. The spent sorbent is eventually fed to the calciner where the endothermic regeneration is carried out at around 850–950 °C. This step yields a CO<sub>2</sub>-rich flue gas (ready for further processing and final storage) and regenerates the CaO-based sorbent. The heat required to sustain the endothermicity of the calcination step is usually supplied by burning auxiliary fuel in the calciner in an oxyfiring mode, so as to avoid dilution of the CO<sub>2</sub>-rich stream generated in the calciner itself. This option requires coupling of the CaL plant with an Air Separation Unit (ASU) to provide oxygen-rich feeding to the calciner. An additional issue arises if a solid auxiliary fuel such as coal is used, resulting in the need to separate ash residues from the regenerated sorbent before recycling to the carbonator. CaL is most typically carried out in a Dual Interconnected Fluidized Bed (DIFB) reactor arrangement, which enables easy solid transfer from one reactor to the other and a convenient environment for the progress of the heterogeneous gas–solid reactions.

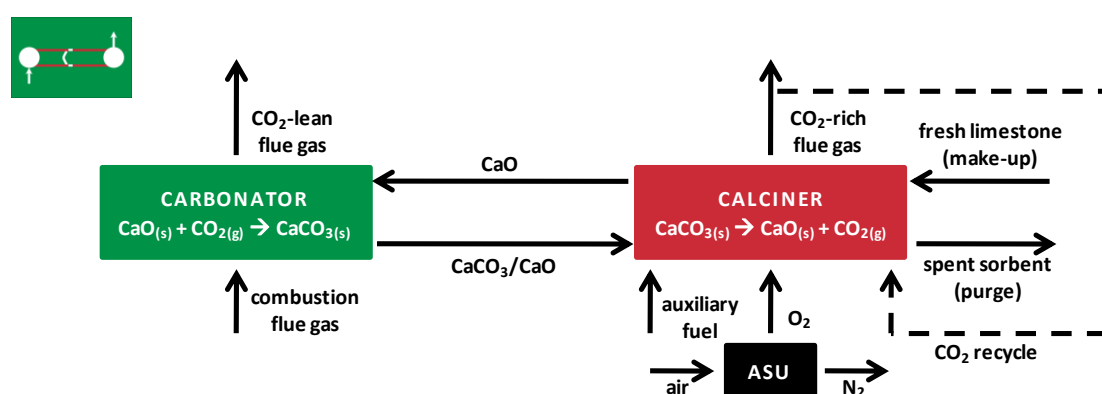


Figure I.20: The calcium looping process.

In the CaL process, the sorbent CO<sub>2</sub> uptake rate and capacity are progressively decreased by deactivation phenomena occurring over iterated looping. Sintering phenomena due to severe thermal history (*Alonso et al.*, 2010) and reaction of the sorbent with SO<sub>2</sub> (which could come from a non-desulphurized flue gas and/or from the auxiliary fuel used in the calciner, see *Coppola et al.*, 2012) both concur to deactivate the sorbent. Moreover, during FB processing, sorbents undergo attrition and fragmentation phenomena that result in the change of the particle size distribution of the sorbent in the reactor, and eventually in a net calcium loss from the circulating loop as elutriable fines (*Charitos et al.*, 2010; *Chen et al.*, 2013; *Coppola et al.*, 2012, 2013; *Valverde and Quintanilla*, 2013). Optimal management of the CaL cycle implies continuous make-up of fresh limestone to compensate for material deactivation and loss by attrition.

Integration of solar energy supply systems in a CaL cycle, with specific reference to the heat required by the calciner, would offer different technical, economical and environmental advantages with respect to a classical CaL cycle. Oxyfiring of supplementary fuel, and the associated complexity and cost of an ASU, are avoided, and so is the generation of solid (ash) and gaseous pollutants from the calciner. No excess oxygen is present in the CO<sub>2</sub>-rich stream issuing from the calciner. Issues related to sorting out fuel ash from the sorbent material are absent. Finally, the possible detrimental interference between CO<sub>2</sub> and SO<sub>2</sub> capture (*Coppola et al.*, 2012) is completely ruled out. The use of solar energy to sustain limestone calcination has been studied in the past (*Badie*, 1980; *Flamant et al.*, 1980; *Imhof*, 1991, 1997, 2000), and it has been proven that solar energy can be conveniently used to calcine limestone in a FB reactor. A lab-scale FB reactor, equipped with a high-pressure Ar arc to simulate the source of solar energy system, has been used to uptake CO<sub>2</sub> from ambient air with Ca-based sorbents (*Nikulshina and Steinfeld*, 2009; *Nikulshina et al.*, 2009). *Matthews and Lipiński* (2012) made instead thermodynamic analysis of an ideal solar driven CaL cycle, estimating the solar energy requirements as a function of the CO<sub>2</sub> molar fraction in the input gas, of the gas and solid phase heat recovery and of the carbonation and of the calcination operative temperatures. On the other hand, *Zhang and Liu* (2014) proposed an hybrid calcination-carbonation process in which the concentrated solar energy is used to supply only part of the energy required for the calcination reaction, so as to reduce the fossil fuel consumption in the calciner. These authors made a sensitivity analysis on the process performance to obtain the effect of the key parameters such as the heat recovery efficiency and the capacity of the CSP. On the same topic but with a different aim, *Edwards and Materić* (2012) suggested using CaL cycles coupled with CSP for thermal energy storage and transportation. These authors proposed the CaO/CaCO<sub>3</sub> cycle as a mean to accomplish thermochemical energy storage with high energy density and high temperature, which can be conveniently combined with power generation in a Brayton cycle. A general review of the research on CaO-based CO<sub>2</sub> capture, with a particular focus on the use of solar energy to accomplish the calcination reaction can be found in the literature (*Reich et al.*, 2014).

## **I.8 Aim of the PhD Thesis**

The analysis of the literature has highlighted the importance of solar energy as a renewable energy source and the basic features of the Concentrating Solar Power technology. The role of Thermal Energy Storage systems has been widely discussed. Finally, the potentialities of fluidized bed reactors have been briefly described, highlighting how the high thermal conductivity and diffusivity in such reactors can help in absorbing the concentrated solar energy and in equalizing the heat received, avoiding thermo-mechanical stresses to both reactor walls and reactive material.

The aim of this PhD Thesis will be the investigation of gas–solid fluidized beds as solar receiver/reactor in Concentrating Solar Power systems. The coupling of Thermal Energy Storage systems together with solar receivers appear to be of fundamental importance to overcome the key drawbacks arising from the intrinsic intermittent nature of the solar energy; in particular, the thermochemical energy storage strategy seems to be a turning point to the deployment of CSP plants. Bearing this in mind, the study of directly irradiated fluidized bed systems will be performed in this PhD Thesis, as this configuration permits to obtain the high operating temperatures required to perform high grade thermochemical processes.

Having recognized the importance that Carbon Capture and Sequestration technologies will have in the near-to-medium term, a model activity will be realized to address the potential advantages arising from the coupling of a CaL process for CO<sub>2</sub> capture from combustion flue gases with a CSP system, with the aim of supplying all the thermal energy required by the calciner through a renewable source. The influence of the main operating parameters on the carbonation efficiency, the loss of elutriated sorbent and the thermal power will be investigated by means of model computations, together with an estimate of the heliostat field that would be required for such a system.

With the aim of eventually studying the performance of Ca-based sorbent for CO<sub>2</sub> capture in solar reactors, and by further considering that the direct heating configuration deals with high density solar radiations, a deep characterization of the direct interaction between a concentrated simulated solar radiation and the surface of a fluidized bed will be performed. Both experimental and model approaches will be employed to investigate the main heat transfer phenomena involved in a directly irradiated gas–solid dense fluidized bed. Possible improvements of the interaction between radiative flux and fluidized particles induced by tailoring the hydrodynamics of the bed will be assessed as well.

The knowledge acquired on the interaction between a concentrated solar radiation and a fluidized bed will then be employed for the design of a directly irradiated solar fluidized bed reactor suitable for the study of thermochemical processes, with special reference to the calcination and carbonation reactions. A commercial limestone will be selected and its performances in term of CO<sub>2</sub> capture capacity and cycling stability when subjected to high intensity solar radiation will be studied.

# Chapter II. A Model of Integrated Calcium Looping for CO<sub>2</sub> Capture and Concentrated Solar Power

## II.1 Introduction

In the present Chapter, an integrated scheme of continuous CaL sustained by CSP for CO<sub>2</sub> capture from combustion flue gases issued by a power plant is described. Integration of a steady CaL cycle with CSP system must take into account the inherent unsteadiness and cyclic character of solar irradiation. Here, a simple scheme of integrated CaL-CSP process is suggested based on the storage of the excess incident solar power during the daytime as calcined sorbent, which is eventually utilized in the CaL loop during the nighttime. The potential of this scheme is assessed by means of model computations. The model is based on a population balance on sorbent particles in the DIFB reactor with storage over the daily cycle. The influence of the main operating parameters on carbonation efficiency, loss of elutriated sorbent and thermal power is determined. A quantitative assessment of the coupling between the CaL cycle and the CSP system is given for a reference base case.

## II.2 The Model

### II.2.1 Outline of the CaL-CSP Integrated Scheme and Main Assumptions

Figures II.1-a and II.1-b show the conceptual scheme of the integrated CaL-CSP system. The two figures correspond to daytime and nighttime operational schemes, respectively. Figure II.1-c outlines the DIFB system, equipped with additional storage vessels for the calcined and carbonated sorbent. Key model variables are reported in Figure II.1, as well. In Figure II.1-a (day operation), the carbonator (termed “CARB”) is fed with the CO<sub>2</sub>-containing gaseous stream and with the CaO stream coming from the calciner (termed “CALC”). A CO<sub>2</sub>-lean flue gas (together with the elutriated fines) leaves the carbonator at the exhaust, and the carbonated sorbent (CaCO<sub>3</sub>/CaO mixture) is drained from the bed and fed to the calciner. During the daytime, the calciner is sustained by the solar source. It is fed by partial recycle of the exhaust gas. Three solid streams are fed to the calciner: the carbonated sorbent from the carbonator, the make-up fresh limestone and a carbonated stream coming from a reservoir (termed “R1”). The regenerated sorbent (CaO) leaving the calciner is splitted into three streams: the lime re-circulated to the carbonator, the excess lime stored in the vessel “R2” and the purge. Figure II.1-b reports the operational scheme during the nighttime. The carbonator is still in operation, as in the daytime operation. The carbonated sorbent leaving the carbonator is stored in the reservoir “R1”, whence it will be fed again to the calciner during the subsequent daytime operation. During the nighttime, the CaO needed for carbonation is provided by the vessel “R2”. The main assumptions of the model are:

- i) Operation.
  1. Operation is steady during either daytime or nighttime. The variability of incident solar power during daytime is neglected. The cyclic nature of incident solar power is considered by simply switching between daytime and nighttime operational modes.

- ii) Hydrodynamics.
  1. The carbonator and calciner are circulating fluidized beds with bottom dense bed, as depicted in Figure II.1-c.
  2. The solid flux in the riser is calculated by means of the modified Wirth (see *Montagnaro et al.*, 2011) correlation.
  3. The detailed modeling of the devices' hydrodynamics of the proposed DIFB system is not considered. The hydrodynamics of the various devices (e.g., loop seals) does not affect process operation under the investigated conditions.
- iii) Reactors and vessels.
  1. The reactors are considered isothermal, while the vessels adiabatic.
  2. The bottom beds are modeled as ideal mixed flow reactors.
  3. The reactors have the same cross section.
- iv) Kinetics and operating conditions.
  1. Flue gas treated in the carbonator bears no acidic gases but CO<sub>2</sub>.
  2. The reactivity of lime toward CO<sub>2</sub> is independent from particle size.
  3. The carbonation degree in the elutriated material is irrelevant to the CO<sub>2</sub> overall mass balance.
  4. The gaseous atmosphere in the calciner is pure CO<sub>2</sub>.
  5. Calcination reaction is fast and complete.

### **II.2.2 Model Equations**

The main equations of the model are population and thermal balance equations, developed in terms of mass or energy fluxes (mass or energy flow rate per reactor cross section). Mass of solid material was expressed in Ca molar basis. Details on the employed nomenclature are also given in § II.5.

Equation (II.1-day) is the population balance equation referred to the sorbent particles (in the size bin  $i$ ) in the carbonator during daytime operation:

$$(1 - f_p)b_{i,L}^{CALC} + \sum_{j=i+1}^n [a_{j,CL}^{CARB} P_{a,CL}^{d_j}(d_i)\Delta d] + s_{i+1,CL}^{CARB} = a_{i,CL}^{CARB} + s_{i,CL}^{CARB} + e_{i,CL}^{CARB} + b_{i,CL}^{CARB} \quad \forall i \quad (\text{II.1-day})$$

At the Left-Hand Side (LHS), the three terms account for, respectively:

- 1) the stream coming from the calciner ( $i$ -th size bin);
- 2) the coarser material already present in the carbonator that, due to attrition, falls into the  $i$ -th size bin;
- 3) the migration of particles, due to the continuous particles shrinkage by attrition, from the  $(i+1)$ -th to the  $i$ -th size bin.

The four terms at the Right-Hand Side (RHS) account for, respectively:

- 1–2) the material leaving the  $i$ -th size bin to generate finer particles due to attrition and shrinkage;
- 3) the particles belonging to the  $i$ -th size family leaving the carbonator as elutriated fines;
- 4) the bed drain ( $i$ -th size bin).

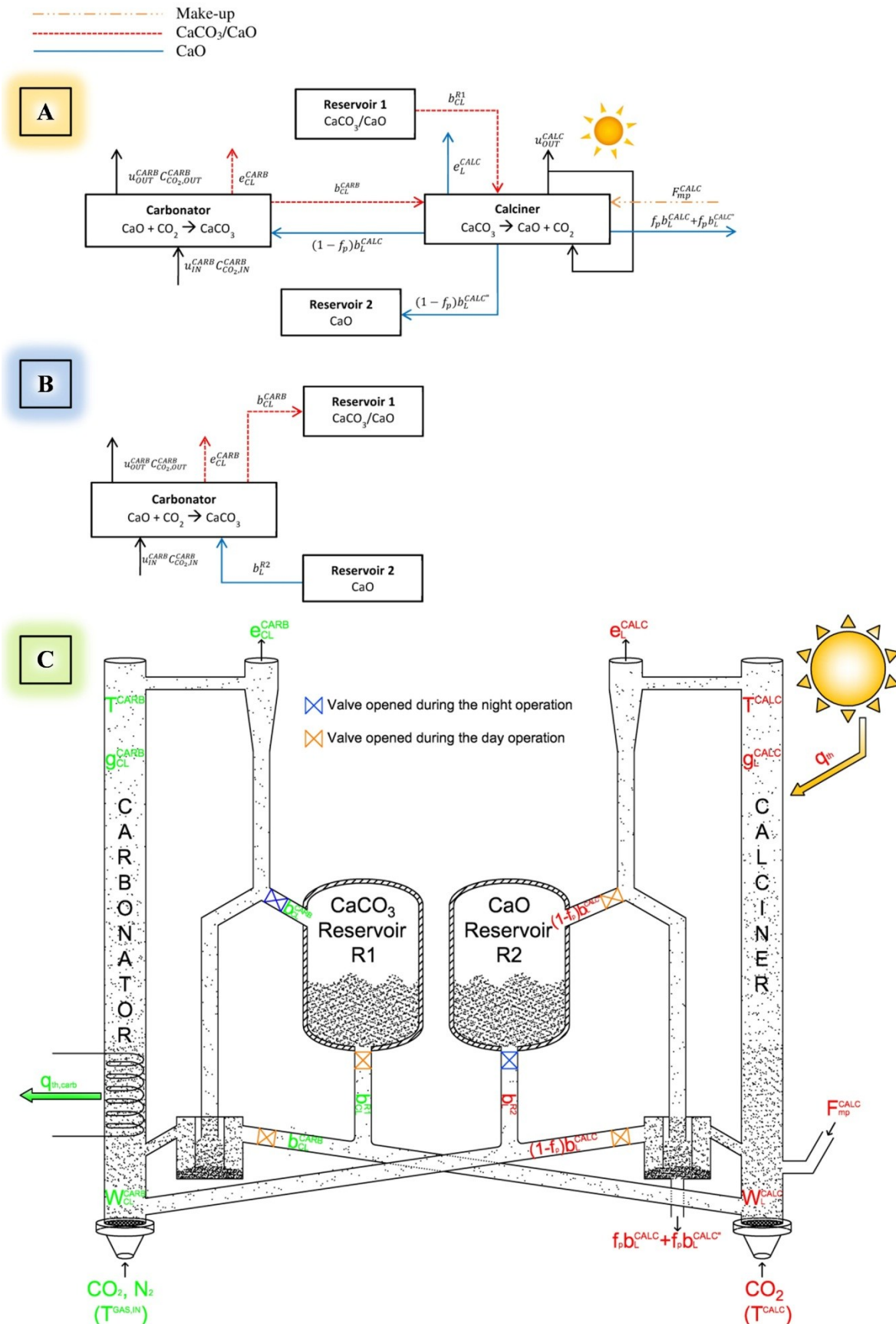


**Figure II.1:** Conceptual reactor scheme during the day (a, up) and the night (b, middle) operation, and schematic (c, down) of the proposed dual interconnected fluidized bed system with the main variables of the model.

Equation (II.2-day) is the population balance equation referred to the sorbent particles (in the  $i$ -th size bin) in the calciner during the day operation:

$$b_{i,CL}^{CARB} + b_{i,CL}^{R1} + F_{mp}^{CALC} P_0(d_i) \Delta d + \sum_{j=i+1}^n \left[ a_{j,L}^{CALC} P_{a,L}^{d_j}(d_i) \Delta d \right] + s_{i+1,L}^{CALC} = a_{i,L}^{CALC} + s_{i,L}^{CALC} + e_{i,L}^{CALC} + b_{i,L}^{CALC} + b_{i,L}^{CALC''} \quad \forall i \quad (\text{II.2-day})$$

At the LHS, besides terms having similar meaning to those in Eq. (II.1-day), the first three contributions are related to the three solid streams entering the system (cf. § II.2.1). RHS of Eq. II.2-day reports terms related to sorbent leaving the calciner or leaving the  $i$ -th size bin toward other size bins.

Equation (II.3-day) is the CO<sub>2</sub> mass balance on the carbonator:

$$u_{IN}^{CARB} C_{CO_2,IN}^{CARB} - u_{OUT}^{CARB} C_{CO_2,OUT}^{CARB} = \sum_i \left[ b_{i,CL}^{CARB} \overline{X_{Ca}^{CARB}} \right] \quad (\text{II.3-day})$$

Similar equations are written, during the nighttime operation, with reference to the carbonator and to the CO<sub>2</sub> mass balance. In particular, Eq. (II.1-night) refers to the carbonator population balance:

$$b_{i,L}^{R2} + \sum_{j=i+1}^n \left[ a_{j,CL}^{CARB} P_{a,CL}^{d_j}(d_i) \Delta d \right] + s_{i+1,CL}^{CARB} = a_{i,CL}^{CARB} + s_{i,CL}^{CARB} + e_{i,CL}^{CARB} + b_{i,CL}^{CARB} \quad \forall i \quad (\text{II.1-night})$$

Equation (II.1-thermal) is the energy balance on the calciner. It is used to express the power demand of the calciner during the day:

$$\begin{aligned} q_{th} = & \sum_i \left\{ b_{i,CL}^{CARB} \left[ \overline{C_{p,CaCO_3}^{CARB}} \overline{X_{Ca}^{CARB}} + (1 - \overline{X_{Ca}^{CARB}}) \overline{C_{p,CaO}} \right] \right\} (T^{CALC} - T^{CARB}) + \\ & + \sum_i \left[ b_{i,CL}^{CARB} \overline{X_{Ca}^{CARB}} \right] \Delta H(T^{CALC}) + \\ & + \sum_i \left\{ b_{i,CL}^{R1} \left[ \overline{C_{p,CaCO_3}^{CARB}} \overline{X_{Ca}^{CARB}} + (1 - \overline{X_{Ca}^{CARB}}) \overline{C_{p,CaO}} \right] \right\} (T^{CALC} - T^{R1}) + \\ & + \sum_i \left[ b_{i,CL}^{R1} \overline{X_{Ca,night}^{CARB}} \right] \Delta H(T^{CALC}) + \\ & + F_{mp}^{CALC} \overline{C_{p,CaCO_3}} (T^{CALC} - T_{mp}) + F_{mp}^{CALC} \Delta H(T^{CALC}) \end{aligned} \quad (\text{II.1-thermal})$$

The six terms at the RHS account for contributions due to heating-up and calcination of the three solid streams entering the calciner.

Finally, the energy balance on the carbonator during both day and night operations is expressed by Eq. (II.2-thermal). This equation is used to express the thermal flux produced by the carbonator:

$$q_{th,carb} = \begin{cases} \left( u_{IN}^{CARB} C_{CO_2,IN}^{CARB} \overline{C_{p,CO_2}} + u_{IN}^{CARB} C_{N_2,IN}^{CARB} \overline{C_{p,N_2}} \right) (T^{GAS,IN} - T^{CARB}) + \sum_i \left[ (1 - f_p) b_{i,L}^{CALC} \overline{C_{p,CaO}} \right] (T^{CALC} + \\ \quad - T^{CARB}) + \sum_i \left[ b_{i,CL}^{CARB} \overline{X_{Ca}^{CARB}} \right] [-\Delta H(T^{CARB})] & \text{day operation} \\ \left( u_{IN}^{CARB} C_{CO_2,IN}^{CARB} \overline{C_{p,CO_2}} + u_{IN}^{CARB} C_{N_2,IN}^{CARB} \overline{C_{p,N_2}} \right) (T^{GAS,IN} - T^{CARB}) + \sum_i \left[ b_{i,L}^{R2} \overline{C_{p,CaO}} \right] (T^{R2} - T^{CARB}) + \\ \quad + \sum_i \left[ b_{i,CL}^{CARB} \overline{X_{Ca}^{CARB}} \right] [-\Delta H(T^{CARB})] & \text{night operation} \end{cases} \quad (\text{II.2-thermal})$$

The three terms at the RHS express contributions related to heating-up of the gaseous stream, cooling-down of the solid stream entering the carbonator and enthalpy of the carbonation reaction.

Additional model equations are reported in Table II.1. In particular, Eqs. (T1–T15) represent the principal ones. In Eq. (II.1-day),  $f_p$  is the fractional mass of sorbent purged from the calciner. The complement  $(1 - f_p)$  is distributed between two streams, one recirculated to the carbonator and the other stored in the vessel “R2”. In particular,  $b_L^{CALC}$  identifies the flux of lime (L) particles leaving the calciner toward the carbonator as recycled material, plus its related purge fraction. Equation (T1) balances the carbonator inlet and outlet solid fluxes, where “CL” stands for the partially carbonated lime ( $\text{CaCO}_3 + \text{CaO}$ ),  $b_{CL}^{CARB}$  is the related flux leaving the carbonator (Eq. (T2), where  $W_{CL}^{CARB}$  is the solid inventory in the carbonator) and  $e_{CL}^{CARB}$  is the flux of sorbent leaving the carbonator as elutriated material. A parallel experimental campaign (Coppola *et al.*, 2012, 2013) suggested that the attrition rate is practically unaffected by the Ca conversion degree, age of the particles and  $\text{CO}_2$  concentration. Accordingly,  $a_{CL}^{CARB}$ , the attrited flux of sorbent particles in the carbonator, is expressed in Eq. (T3), where  $k_{a,CL}$  is a non-dimensional attrition constant,  $d_i$  is the particle diameter,  $u_{mf}^{CARB}$  is the minimum fluidization velocity in the carbonator and  $u_{OUT}^{CARB}$  is the gas superficial velocity in the carbonator. The latter is expressed by Eq. (T4), where  $\chi_{\text{CO}_2}$  is the gas volume variation factor associated with the course of carbonation,  $X_{\text{CO}_2}$  is the  $\text{CO}_2$  capture efficiency and  $u_{IN}^{CARB}$  is the gas superficial velocity at the carbonator inlet.  $X_{\text{CO}_2}$  is further detailed by Eq. (T5), where  $C_{\text{CO}_2,IN}^{CARB}$  is the inlet  $\text{CO}_2$  concentration to the carbonator (in the following, the corresponding outlet value is referred to as  $C_{\text{CO}_2,OUT}^{CARB}$ , equal to the value establishing in the bottom bed, according to the mixed flow assumption) and  $\overline{X_{Ca}^{CARB}}$  is the mean Ca conversion degree, as detailed after.  $P_{a,CL}^{d_j}(d_i)$  is the distribution function of the carbonated sorbent fragments having size  $d_i$ , generated by attrition from mother particles with a coarser size  $d_j$ . It is calculated from Eq. (T6), where  $\bar{d}$  is the mean diameter of the attrited fragments. Finally,  $s_{CL}^{CARB}$  is the flux of shrinking particles in the carbonator, according to Eq. (T7).

Similar terms are present in Eq. (II.2-day). The term  $b_{CL}^{R1}$  relates to the carbonated sorbent flux from the reservoir “R1” to the calciner, expressed in Eq. (T8), where the ratio under brackets refers to nighttime operation.  $F_{mp}^{CALC}$  is the make-up flux of raw limestone which, according to Eq. (T9), must balance the loss of material by purge and elutriation.  $P_0$  expresses the particle size distribution of the raw sorbent, embodying the effect of primary fragmentation following sorbent feeding.  $b_L^{CALC}$  is the lime flux leaving the calciner toward the reservoir “R2”, including its purge fraction. Terms  $a_L^{CALC}$  and  $s_L^{CALC}$  are expressed similarly to Eqs. (T3) and (T7), respectively, considering the gas superficial velocity  $u_{OUT}^{CALC}$  in the calciner. This velocity is computed by Eq. (T10), where  $R_R^{CALC}$  is the gas recycle ratio to the calciner inlet.  $P$ ,  $R$  and  $T$  are the total pressure, the ideal gas constant and the operating temperature, respectively.

In Eq. (II.1-night),  $b_{i,L}^{R2}$  is the flux of lime leaving the reservoir “R2” to be fed to the carbonator during nighttime operation (Eq. (T11)).

In Eq. (II.1-thermal),  $q_{th}$  is the thermal flux required by the daytime operation of the calciner;  $\overline{C_p}$  is the mean thermal capacity;  $T_{mp}$  is the temperature of the make-up stream;  $\Delta H$  is the enthalpy of the calcination reaction. In Eq. (II.2-thermal),  $q_{th,carb}$  is the thermal flux generated during the daytime and the nighttime operation of the carbonator.

Further constraints are given by mass balances Eqs. (T12–T15), where  $t_{day}$  and  $t_{night}$  are the daytime and nighttime durations, respectively.

Equations needed for the computation of  $\overline{X_{Ca}^{CARB}}$  are also reported in Table II.1 (Eqs. (T16–T20)). Equation (T16) is the expression of the reaction rate (an adapted form of the well established grain model which meets the condition that the rate be zero when the actual carbonation degree approaches its maximum value), where  $k_{carb}$  is the kinetic constant,  $X_{Ca}^{CARB}$  is the instantaneous calcium conversion degree,  $X_{Ca}^{CARB,MAX}$  its maximum (asymptotic) value and  $C_{CO_2,EQ}^{CARB}$  is the equilibrium value for the CO<sub>2</sub> concentration, computed according to Eq. (T17). Equation (T16) gives the  $X_{Ca}^{CARB}(t)$  profile used in Eq. (T18), where  $E(t)$  expresses the residence time distribution of the sorbent particles in the reactor according to a well mixed flow pattern. In Eq. (T18),  $t^{*,CARB}$  is the time needed for particle complete conversion, computed by Eq. (T19), while  $\tau^{CARB}$  is the mean solid residence time in the carbonator, calculated according to Eq. (T20).

In Table II.1, Eqs. (T21–T25) are those needed for the evaluation of the elutriation rates. Equation (T21) relates to the computation of the flux of elutriated material. This is related to the cyclone collection efficiency,  $\omega_c^{CARB}$ , and to the mass flux of recirculating material in the riser,  $g_{CL}^{CARB}$ . The cyclone efficiency is expressed according to Eq. (T22), where  $d_{cut}$  is the cut-off diameter and  $n_c$  an appropriate exponent.  $g_{CL}^{CARB}$  is calculated according to *Montagnaro et al.* (2011). In Eq. (T23),  $\rho_{mol}$  is the molar density,  $\varepsilon_{mf}^{CARB}$  is the bed voidage at minimum fluidization, while the non-dimensional parameter  $\beta_{CL}^{CARB}$  is expressed as in Eq. (T24) (*Montagnaro et al.*, 2011), where  $u_{\infty,CL}^{CARB}$  is the particle terminal velocity, and the Froude number is detailed in Eq. (T25). In this last equation, the solid densities  $\rho_L$  and  $\rho_{CL}$  and the gas density  $\rho_g$  are expressed as mass per volume, while  $g_c$  is the gravity constant. Similar expressions hold for the equations referred to the calciner.

### Principal equations:

$$(1 - f_p) \sum_i b_{i,L}^{CALC} = \sum_i b_{i,CL}^{CARB} + \sum_i e_{i,CL}^{CARB} \quad (T1)$$

$$b_{i,CL}^{CARB} = \frac{\sum_i b_{i,CL}^{CARB}}{\sum_i W_{i,CL}^{CARB}} W_{i,CL}^{CARB} \quad (T2)$$

$$a_{i,CL}^{CARB} = \frac{k_{a,CL}(u_{OUT}^{CARB} - u_{mf}^{CARB})W_{i,CL}^{CARB}}{d_i} \quad (T3)$$

$$u_{OUT}^{CARB} = (1 + \chi_{CO_2} X_{CO_2}) u_{IN}^{CARB} \quad (T4)$$

$$X_{CO_2} = \frac{\sum_i [b_{i,CL}^{CARB} \overline{X_{Ca}^{CARB}}]}{u_{IN}^{CARB} C_{CO_2,IN}^{CARB}} \quad (T5)$$

$$P_{a,CL}^{d_j}(d_i) = \frac{\frac{1}{d} \exp\left(-\frac{d_i}{d}\right)}{1 - \exp\left(-\frac{d_j}{d}\right)} \quad \forall i < j \quad (T6)$$

$$s_{i,CL}^{CARB} = \frac{k_{a,CL}(u_{OUT}^{CARB} - u_{mf}^{CARB})W_{i,CL}^{CARB}}{3 \Delta d} \quad (T7)$$

$$b_{i,CL}^{R1} = \sum_i b_{i,CL}^{R1} \left( \frac{W_{i,CL}^{CARB}}{\sum_i W_{i,CL}^{CARB}} \right) \Big|_{night} \quad (T8)$$

$$F_{mp}^{CALC} = f_p \sum_i b_{i,L}^{CALC} + f_p \sum_i b_{i,L}^{CALC''} + \sum_i e_{i,CL}^{CARB} + \sum_i e_{i,L}^{CALC} + \sum_i e_{i,CL,night}^{CARB} \frac{t_{night}}{t_{day}} \quad (T9)$$

$$u_{OUT}^{CALC} = (R_R^{CALC} + 1) \frac{F_{mp}^{CALC} + \sum_i [b_{i,CL}^{CARB} \overline{X_{Ca}^{CARB}}]}{P^{CALC}/(RT^{CALC})} \quad (T10)$$

$$b_{i,L}^{R2} = \sum_i b_{i,L}^{R2} \left( \frac{W_{i,L}^{CALC}}{\sum_i W_{i,L}^{CALC}} \right) \Big|_{day} \quad (T11)$$

$$(1 - f_p) \sum_i b_{i,L}^{CALC} = (1 - f_p) \sum_i b_{i,L}^{CALC} \frac{t_{night}}{t_{day}} \quad (T12)$$

$$(1 - f_p) \sum_i b_{i,L}^{CALC} = \sum_i b_{i,L}^{R2} \quad (T13)$$

$$\sum_i b_{i,L}^{R2} = \sum_i b_{i,CL,night}^{CARB} + \sum_i e_{i,CL,night}^{CARB} \quad (T14)$$

$$\sum_i b_{i,CL,night}^{CARB} = \sum_i b_{i,CL}^{R1} \frac{t_{day}}{t_{night}} \quad (T15)$$

### Kinetic equations:

$$\frac{dX_{Ca}^{CARB}}{dt} = k_{carb} \left( 1 - \frac{X_{Ca}^{CARB}}{X_{Ca}^{CARB,MAX}} \right)^{\frac{2}{3}} (C_{CO_2,OUT}^{CARB} - C_{CO_2,EQ}^{CARB}) \quad (T16)$$

$$C_{CO_2,EQ}^{CARB} = \frac{1.462 \cdot 10^{11}}{T^{CARB}} \exp \left( -\frac{19130}{T^{CARB}} \right) \quad (T17)$$

$$\overline{X_{Ca}^{CARB}} = \int_0^{t^*,CARB} X_{Ca}^{CARB}(t) E(t) dt + \int_{t^*,CARB}^{+\infty} X_{Ca}^{CARB,MAX} E(t) dt = \quad (T18)$$

$$= 6X_{Ca}^{CARB,MAX} \left\{ \frac{1}{2} \left( \frac{\tau^{CARB}}{t^*,CARB} \right) - \left( \frac{\tau^{CARB}}{t^*,CARB} \right)^2 + \left( \frac{\tau^{CARB}}{t^*,CARB} \right)^3 \left[ 1 - \exp \left( -\frac{t^*,CARB}{\tau^{CARB}} \right) \right] \right\}$$

$$t^*,CARB = \frac{3X_{Ca}^{CARB,MAX}}{k_{carb} (C_{CO_2,OUT}^{CARB} - C_{CO_2,EQ}^{CARB})} \quad (T19)$$

$$\tau^{CARB} = \frac{\sum_i W_{i,CL}^{CARB}}{(1-f_p) \sum_i b_{i,L}^{CALC}} \quad (T20)$$

### Equations for the evaluation of the elutriated streams:

$$e_{i,CL}^{CARB} = g_{i,CL}^{CARB} [1 - \omega_c^{CARB}(d_i)] \quad (T21)$$

$$\omega_c^{CARB}(d_i) = \frac{1}{1 + \left( \frac{d_{cut}^{CARB}}{d_i} \right)^{n_c}} \quad (T22)$$

$$g_{i,CL}^{CARB} = \quad (T23)$$

$$= \beta_{i,CL}^{CARB}(d_i) [\rho_{mol,CaO} (1 - \overline{X_{Ca}^{CARB}}) + \rho_{mol,CaCO_3} \overline{X_{Ca}^{CARB}}] (1 - \epsilon_{mf}^{CARB}) u_{OUT}^{CARB} \frac{W_{i,CL}^{CARB}}{\sum_i W_{i,CL}^{CARB}}$$

$$\beta_{i,CL}^{CARB} = \quad (T24)$$

$$\begin{cases} \left( 1 - \frac{u_{\infty,CL}^{CARB}(d_i)}{u_{OUT}^{CARB}} \right)^2 \cdot 0.00533 \frac{Fr^2(d_i)^{CARB}}{4(1 - \epsilon_{mf}^{CARB})} & \text{for } u_{\infty,CL}^{CARB} < u_{OUT}^{CARB} \\ 0 & \text{for } u_{\infty,CL}^{CARB} \geq u_{OUT}^{CARB} \end{cases}$$

$$Fr(d_i)^{CARB} = \frac{u_{OUT}^{CARB}}{\sqrt{\left\{ \frac{[\rho_L(1 - X_{Ca}^{CARB}) + \rho_{CL} X_{Ca}^{CARB}] - \rho_g}{\rho_g} \right\} d_i g_c}} \quad (T25)$$

**Table II.1:** Additional model equations.

### II.2.3 Evaluation of Parameters

Table II.2 lists the values of the main parameters used in the model, chosen as close as possible to realistic conditions (Charitos *et al.*, 2011; Dieter *et al.*, 2014; Martínez *et al.*, 2013; Romano, 2012; Ströhle *et al.*, 2014). The carbonator is operated at 923 K (the model parameters of the carbonator have the same values during the day and the night operation), as well as the reservoir

“R1”. The calciner temperature is 1213 K. The whole system is at atmospheric pressure. Assuming a flue gas to be treated in the carbonator having a 15%<sub>v</sub> CO<sub>2</sub> fraction, its inlet CO<sub>2</sub> concentration turns out to be 2.0 mol m<sup>-3</sup>.

Parameter	Units	Value
$T^{CARB} = T^{R1}$	[K]	923
$T^{CALC}$	[K]	1213
$P$	[Pa]	$1.01 \times 10^5$
$C_{CO_2,IN}^{CARB}$	[mol m <sup>-3</sup> ]	2
$u_{IN}^{CARB} = u_{OUT}^{CALC}$	[m s <sup>-1</sup> ]	1, 2, 3
$(1 - f_p) \sum_i b_{i,L}^{CALC}$	[mol <sub>Ca</sub> m <sup>-2</sup> s <sup>-1</sup> ]	4–16, 8–32, 12–48
$\sum_i W_{i,CL}^{CARB} = \sum_i W_{i,L}^{CALC}$	[mol <sub>Ca</sub> m <sup>-2</sup> ]	2000, 4000, 6000
$\tau^{CARB}$	[s]	500–125
$f_p$	[-]	0.05
$T_{mp,IN}$	[K]	298
$k_{carb}$	[m <sup>3</sup> mol <sup>-1</sup> s <sup>-1</sup> ]	0.02
$X_{Ca}^{CARB,MAX}$	[-]	0.35
$k_{a,CL}$	[-]	$3 \times 10^{-9}$
$k_{a,L}$	[-]	$5 \times 10^{-9}$
$\bar{d}$	[m]	$35 \times 10^{-6}$
$d_{cut}^{CARB}$	[m]	$10 \times 10^{-6}$
$n_c$	[-]	4
$t_{day} = t_{night}$	[h]	12
$\chi_{CO_2}$	[-]	-0.15
$\varepsilon_{mf}^{CARB}$	[-]	0.42

**Table II.2:** Main input parameters of the model.

Three different cases have been studied, according to three different values for the inlet gas velocity in the carbonator: 1, 2, 3 m s<sup>-1</sup>. This was done since some variability of this important inlet parameter is reported in the literature (*Rodríguez et al.*, 2011a, 2011b). With the aim of working at carbonator inlet Ca/C molar ratios:

$$\frac{Ca}{C} = \frac{(1-f_p) \sum_i b_{i,L}^{CALC}}{u_{IN}^{CARB} C_{CO_2,IN}^{CARB}} \quad (II.4)$$

in the 2–8 range (*Shimizu et al.*, 1999) in any of the three cases, the flux of sorbent exiting the calciner and fed to the carbonator is varied in the range 4–16, 8–32 and 12–48 mol m<sup>-2</sup> s<sup>-1</sup> when the inlet gas velocity is 1, 2 and 3 m s<sup>-1</sup>, respectively. Values of the mean residence time of the solid in the carbonator ranged from 125 to 500 s (*Rodríguez et al.*, 2011b). For any given inlet gas velocity and sorbent inventory, the only parameter affecting the mean solid residence time in the carbonator is the sorbent feeding rate to the carbonator. For example, in the case of an inlet gas velocity of 1 m s<sup>-1</sup>, and keeping the inventory fixed at 2000 mol<sub>Ca</sub> m<sup>-2</sup>, when the sorbent flux ranges from 4 to 16 mol m<sup>-2</sup> s<sup>-1</sup> the solid residence time correspondingly ranges from 500 to 125 s, and the carbonator

inlet  $Ca/C$  molar ratio from 2 to 8. The purge stream from the calciner is fixed at 5% of the outlet streams to the “R2” vessel and to the carbonator ( $f_p=0.05$ ) (Romeo *et al.*, 2008, 2009). In the kinetic Eq. (T16), the reaction constant is equal to  $0.02 \text{ m}^3 \text{ mol}^{-1} \text{ s}^{-1}$  (Charitos *et al.*, 2011; Montagnaro *et al.*, 2011; Scala *et al.*, 1997) and the maximum value for the calcium conversion degree is 35%, as inferred from the literature (Abanades, 2002) taking as the maximum conversion degree an average between that of a fresh sorbent and that of a sorbent subjected to multiple calcination-carbonation cycles. The attrition constants are  $3 \times 10^{-9}$  and  $5 \times 10^{-9}$  for the carbonated and calcined limestone, respectively, taking into account that the  $\text{CaCO}_3$ -rich shell makes the partly carbonated material more resistant to surface wear. The particle size distribution ( $P_0(d_i)$ ) of the inlet fresh sorbent is expressed as a log-normal function extending over the 0–1000  $\mu\text{m}$  particle size range, with a mean Sauter diameter of 105  $\mu\text{m}$ , a distribution peak equal to 65  $\mu\text{m}$  and a median value of 170  $\mu\text{m}$ . As far as the distribution function of the attrited fragments is concerned (Eq. (T6)), a mean diameter of 35  $\mu\text{m}$  is assumed in the computations. Attrition of particles finer than 50  $\mu\text{m}$  is neglected. The cyclone cut diameter is 10  $\mu\text{m}$ . Computations have been referred to 12 h daytime/12 h nighttime daily cycles.

#### **II.2.4 Model Implementation**

Model equations consist of a system of nonlinear equations (200 equispaced size bins are considered in the 0–1000  $\mu\text{m}$  range) implemented and solved in the MATLAB environment using the *fsolve* function which embodies the Levenberg–Marquardt algorithm. The method guarantees the convergence of the solution with a tolerance and precision of  $10^{-6}$ .

### **II.3 Results and Discussion**

#### **II.3.1 Results of Base Case Model Computations**

Model results have been first obtained for a reference base case. To this end, a combustion plant of 100  $\text{MW}_{\text{th}}$  thermal power has been considered, fuelled with a bituminous coal with the following typical main properties and composition (Solimene *et al.*, 2012): ultimate analysis, dry basis – 66.5% C, 4.4% H, 1.2% N, 0.6% S, 13.3% O –; proximate analysis – 7.4% moisture, 21.8% volatiles, 57.9% fixed carbon, 12.9% ash –; lower heating value of  $25.76 \text{ MJ kg}^{-1}$ . The  $\text{CO}_2$  stream generated from the combustor (to be concentrated in the CaL cycle) amounts to  $0.20 \text{ kmol s}^{-1}$ . The inlet temperature for the combustion flue gases to be treated in the carbonator was taken equal to the carbonator temperature, namely  $T^{\text{GAS,IN}} = T^{\text{CARB}} = 650 \text{ }^\circ\text{C}$ .

The following base case operating parameters of the CaL system were selected:  $\tau=250 \text{ s}$  (for both the reactors),  $u_{\text{IN}}^{\text{CARB}}=2 \text{ m s}^{-1}$ ,  $\sum_i W_{i,\text{CL}}^{\text{CARB}} = \sum_i W_{i,\text{L}}^{\text{CALC}}=4000 \text{ mol m}^{-2}$ . This choice resulted into a value of the cross-sectional area of both the calciner and the carbonator equal to  $A=50.3 \text{ m}^2$ . The main results of this base case model computation are summarized in Table II.3 and depicted in Figure II.2. The mean carbonation degree was 0.22, while the  $\text{CO}_2$  capture efficiency approached a fairly high value of 89%. The sorbent elutriation rate from the carbonator was  $5.72 \text{ mol}_{\text{Ca}} \text{ s}^{-1}$ . According to Eq. (T9) (therefore, considering the elutriation from both reactors and the fixed sorbent purge rate), the sorbent make-up flow rate to the calciner was  $108.5 \text{ mol}_{\text{Ca}} \text{ s}^{-1}$ . A key aspect of the design regards the integration between the daytime and nighttime operation of the plant

(Figure II.1). The storage of excess lime produced during daytime operation, and of carbonated lime during nighttime operation, requires two storage vessels (“R1” and “R2”) of nearly 2200 m<sup>3</sup> volume each. The thermal power that must be supplied to the calciner during the daytime cycle is 135 MW. Using a reference value of the direct normal irradiance (*DNI*) of 850 W m<sup>-2</sup> and an overall efficiency factor of 0.6 (including reflection and re-emission from the receiver), the thermal input to the calciner would be supplied by a heliostats field of surface *S*=0.26 sqkm. The thermal power available at the carbonator is 50 MW throughout daytime and nighttime cycles. It is worth underlying that the combined power at the combustion plant and at the CaL-CSP combined process makes the overall thermal throughput of the integrated system equal to 150 MW<sub>th</sub>.

Parameter	Physical meaning	Units	Value
$\overline{X}_{Ca}^{CARB}$	mean Ca carbonation degree	[-]	0.22
$X_{CO_2}$	CO <sub>2</sub> capture efficiency	[-]	0.89
$A \sum_i e_{i,CL}^{CARB}$	elutriation flow rate from the carbonator	[mol <sub>Ca</sub> s <sup>-1</sup> ]	5.72
$F_{mp}^{CALC} A$	make-up flow rate to the calciner	[mol <sub>Ca</sub> s <sup>-1</sup> ]	108.5
	volume of vessels “R1” and “R2”	[m <sup>3</sup> ]	~2200
$q_{th}A$	thermal power required by the calciner (during daytime)	[MW]	135
$q_{th,carb}A$	thermal power produced by the carbonator (during both daytime and nighttime)	[MW]	50
<i>S</i>	surface of the heliostats field	[sqkm]	0.26

**Table II.3:** Results of model computations for the base case.

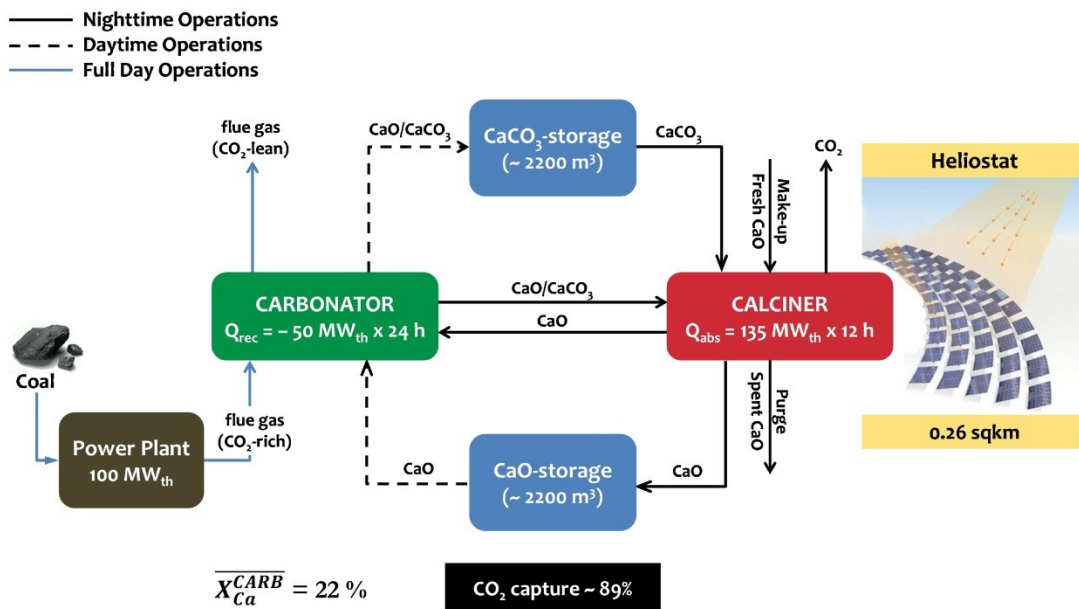


**Figure II.2:** Scheme of the solar CaL with the main results of the base-case.

### II.3.2 Effect of the Operating Parameters

Key operational parameters of the system are represented by the mean solid residence time  $\tau^{CARB}$  in the carbonator, which dictates the solids recirculation rate between the calciner and the

carbonator, and the gas superficial velocity  $u_{IN}^{CARB}$  in the carbonator. The influence of these variables on the performance of the integrated CaL-CSP scheme will be investigated hereinafter.

Figure II.3 reports the mean calcium conversion degree in the stream leaving the carbonator as a function of  $\tau^{CARB}$  taking  $u_{IN}^{CARB}$  as a parameter. No effect in the change of the inlet gas velocity is observed as, according to the model hypotheses,  $\overline{X_{Ca}^{CARB}}$  is a function of  $\tau^{CARB}$  only. The analysis of the plot indicates that longer solid residence times (i.e., smaller sorbent recirculating fluxes) result into larger mean carbonation degrees, rising from 12% when  $\tau^{CARB}=125$  s ( $Ca/C=8$ ) to 33% when  $\tau^{CARB}=500$  s ( $Ca/C=2$ ). The mean carbonation degree at  $\tau^{CARB}=500$  s approaches its theoretical maximum (35%). Moreover, Figure II.3 reports the CO<sub>2</sub> capture efficiency as a function of  $\tau^{CARB}$ . Again, the influence of  $u_{IN}^{CARB}$  is negligible. The capture efficiency decreases from 90.6% to 66.5% as  $\tau^{CARB}$  increases. This effect is related to the combined influence of the increased Ca conversion and the reduced recirculation rate of the sorbent as  $\tau^{CARB}$  increases. The trend observed in Figure II.3 reflects, as expected, the increased “productivity” (i.e., the CO<sub>2</sub> capture efficiency  $X_{CO_2}$ ) of the carbonator as it is operated toward differential conditions with respect to the recirculated sorbent. From a practical standpoint, however, it is observed that  $X_{CO_2} \sim 90\%$  when  $\tau^{CARB} \sim 200$  s, indicating that the incremental benefit of operating at even shorter solid residence times, i.e. larger recirculation rates, is very limited.

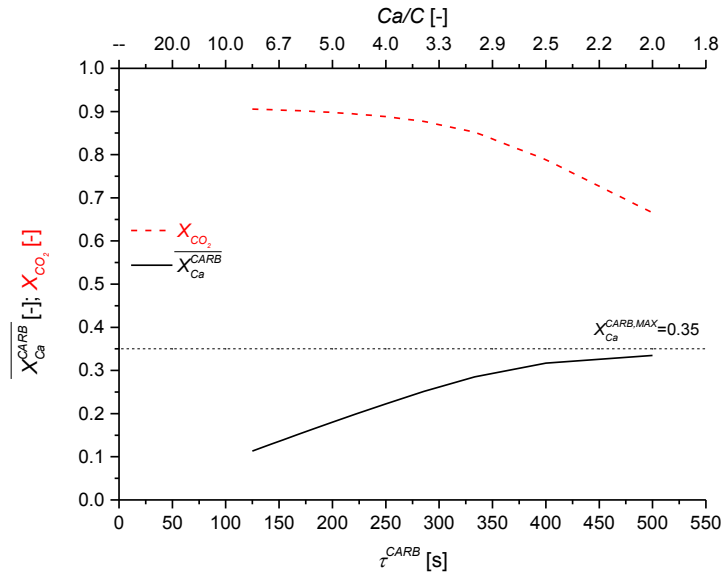


**Figure II.3:** Mean calcium carbonation degree (Eq. (T18)) and CO<sub>2</sub> capture efficiency (Eq. (T5)) as a function of the sorbent mean residence time (Eq. (T20)) and of the inlet CaO-to-CO<sub>2</sub> molar ratio (Eq. (II.4)). The plot is the same for all the three inlet gas velocities ( $u_{IN}^{CARB}=1, 2, 3$  m s<sup>-1</sup>).

The elutriation rate of calcium has been expressed as  $E^*$ , defined as the moles of Ca elutriated from the carbonator per mole of CO<sub>2</sub> fed to the system:

$$E^* = \frac{\sum_i e_{i,CL}^{CARB}}{u_{IN}^{CARB} C_{CO_2,IN}^{CARB}} \quad (\text{II.5})$$

This specific elutriation rate has been evaluated as a function of  $\tau^{CARB}$  for the three cases investigated. Model results show that the effect of the solid residence time is very limited. On the

other hand, a moderate increase of  $E^*$  is observed when the inlet CO<sub>2</sub> flux is increased.  $E^*$  resulted 0.014, 0.029 and 0.046 mol<sub>Ca</sub> mol<sub>CO<sub>2</sub></sub><sup>-1</sup> when  $u_{IN}^{CARB}$  was 1, 2 and 3 m s<sup>-1</sup>, respectively. This finding can be related to the effect that operating at increasing gas superficial velocities exerts on solids attrition and fines carryover, and that larger velocities are bound to larger sorbent inventories, as pointed out in §II.2.3, which imply larger generation of attrition fines (see Eq. (T3)). Model computations enable the assessment of the make-up of fresh sorbent needed to compensate for the purge and elutriated streams. The make-up depends on both the solid residence time and gas velocities. The specific make-up, expressed as mole of fresh Ca per mole of CO<sub>2</sub> fed to the system, ranges between 0.90 and 0.26, mol<sub>Ca</sub> mol<sub>CO<sub>2</sub></sub><sup>-1</sup> when  $\tau^{CARB}$  ranges between 125 and 500 s and  $u_{IN}^{CARB}=1$  m s<sup>-1</sup>. The specific make-up is comprised between 0.97 and 0.32, 1.05 and 0.39 mol<sub>Ca</sub> mol<sub>CO<sub>2</sub></sub><sup>-1</sup> when  $u_{IN}^{CARB}$  is set at 2 and 3 m s<sup>-1</sup>, respectively, in the same range of  $\tau^{CARB}$ . The specific make-up decreases along with the mean solid residence time, due to the smaller recirculating sorbent fluxes. The moderate increase observed when the inlet CO<sub>2</sub> flux increases is related to the effect of larger elutriation rates, as discussed above. Analyzing data over the whole system (carbonator and calciner) and daily cycle (daytime and nighttime) suggests that make-up is largely (87–67%) due to replacement of purge spent/sintered material, while a smaller (13–33%), though not negligible contribution, is related to sorbent loss by elutriation. Table II.4 lists the values of the mean Sauter diameter of the sorbent inventory in the carbonator and of the elutriated material. It is recalled here that the Sauter diameter for the raw limestone was set at 105  $\mu$ m. The Sauter mean diameter of the inventory material is always larger than the value of the parent make-up. In fact, attrition generates finer sorbent particles ( $d_{Sauter}=13–16$   $\mu$ m) mostly lost by elutriation, leaving behind a sorbent in the bottom bed with a particle size distribution shifted toward coarser sizes. The increase in the mean diameter of the bed solids is emphasized as the gas superficial velocity is increased, which enhances attrition and fines entrainment.

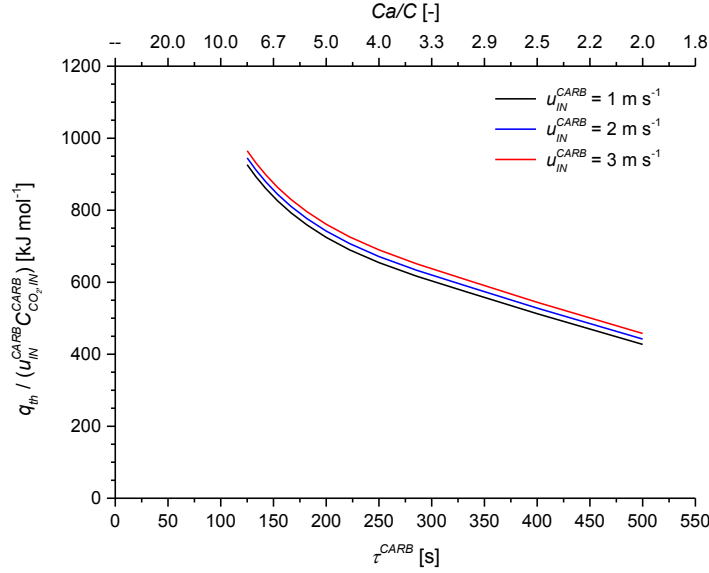
Operation of the carbonator during the night can be analysed much like the daytime cycle. Energy integration over the whole daily – daytime+nighttime – cycle requires two reservoirs (“R1” and “R2”) to host an inventory of 173–691 kmol<sub>Ca</sub> m<sup>-2</sup> ( $u_{IN}^{CARB}=1$  m s<sup>-1</sup>), 346–1380 kmol<sub>Ca</sub> m<sup>-2</sup> ( $u_{IN}^{CARB}=2$  m s<sup>-1</sup>) and 518–2074 kmol<sub>Ca</sub> m<sup>-2</sup> ( $u_{IN}^{CARB}=3$  m s<sup>-1</sup>) when  $\tau^{CARB}$  ranges between 125 and 500 s.

$u_{IN}^{CARB}$ [m s <sup>-1</sup> ]	$\bar{d}(Sauter)$ [ $\mu$ m]	
	Inventory	Elutriated
1	113–116	13–14
2	122–123	15
3	128–132	16

**Table II.4:** Mean Sauter diameter for the carbonator inventory material and elutriated flux, as a function of the inlet gas velocity.

Figure II.4 addresses the calciner thermal duty and reports the specific thermal requirement per mole of CO<sub>2</sub> fed to the system. The plot suggests that the specific energy needed per unit CO<sub>2</sub> in the feeding decreases as one considers longer sorbent mean residence times. At fixed inventory (and  $u_{IN}^{CARB}$ ), at least three different effects concur in the energy requirement. By increasing  $\tau^{CARB}$ , the mean carbonation degree of the recirculating stream is larger, and the specific energy needed for the calcination process increases correspondingly. At the same time, longer  $\tau^{CARB}$  also means smaller recirculating and make-up fluxes, and this moderates the specific energy requirement. Since the

profile of the calciner specific thermal requirement vs.  $\tau^{CARB}$  is strictly decreasing, these last effects are predominant. On the other hand, an increase in  $u_{IN}^{CARB}$  results in slightly larger specific energy requirements. In this case, the increase of both the recirculating and the sorbent make-up enhances the specific thermal power requirement of the calciner. The energy duty of the calciner ranges between 926–427 kJ mol<sub>CO<sub>2</sub></sub><sup>-1</sup> ( $u_{IN}^{CARB}=1$  m s<sup>-1</sup>), 945–442 kJ mol<sub>CO<sub>2</sub></sub><sup>-1</sup> ( $u_{IN}^{CARB}=2$  m s<sup>-1</sup>) and 965–458 kJ mol<sub>CO<sub>2</sub></sub><sup>-1</sup> ( $u_{IN}^{CARB}=3$  m s<sup>-1</sup>) when  $\tau^{CARB}$  increases from 125 to 500 s.



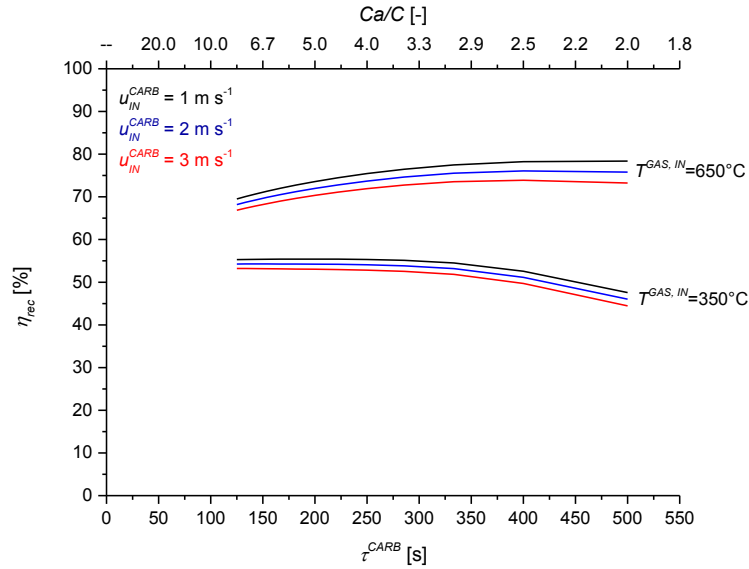
**Figure II.4:** Specific calciner thermal requirement (see Eq. (II.1-thermal)), per mole of CO<sub>2</sub> fed to the system, as a function of the sorbent mean residence time (Eq. (T20)) and of the inlet CaO-to-CO<sub>2</sub> molar ratio (Eq. (4)). The curves are parametric with respect to the carbonator inlet gas velocity.

Figure II.5 refers to the thermal duty of the carbonator. Equation (II.2-thermal) was solved taking two alternative values of the carbonator inlet flue gas temperature, namely 350 °C and 650 °C. An inlet temperature of 350 °C may be realistic when CaL is applied to an existing thermal plant. In this case it is likely that flue gases fed to the carbonator derive from a gas clean-up system. The inlet temperature of 650 °C can be representative of a CaL process integrated in a new combustion plant where thermal power at the carbonator can be integrated within the thermodynamic cycle of the power plant. In both cases, the solution of Eq. (II.2-thermal) yields a positive value of  $q_{th,carb}$ , indicating that it is always necessary to extract heat from the carbonator to keep its temperature at the pre-set value ( $T^{CARB}$ ). Bearing this in mind, Figure II.5 reports  $\eta_{rec}$ , the ratio between the energy which can be recovered over the 24 h-cycle, and the calciner thermal requirement.  $\eta_{rec}$ , expressed according to Eq. (II.6):

$$\eta_{rec} = \frac{q_{th,carb}|_{day} t_{day} + q_{th,carb}|_{night} t_{night}}{q_{th} t_{day}} \quad (\text{II.6})$$

is plotted in Figure II.5 as a function of  $\tau^{CARB}$  for either inlet flue gas temperature and varying the fluidization velocity. The effect of  $\tau^{CARB}$  on  $\eta_{rec}$  is non-trivial. Increasing  $\tau^{CARB}$  results into larger carbonation degrees, hence increases the specific thermal flux required by the calciner. Moreover, it reduces the recirculation solid flux, and the associated net enthalpy flux from the carbonator to the calciner. The overall dependency of  $\eta_{rec}$  vs.  $\tau^{CARB}$  is fairly moderate. The effect of increasing the

carbonator inlet flue gas temperature on the increase of  $\eta_{rec}$  is, as expected, fairly strong. Furthermore, larger inlet gas velocities yield smaller values of  $\eta_{rec}$  (see, in particular, Figure II.4 where the undesired effect of  $u_{IN}^{CARB}$  on the specific thermal flux required by the calciner is clarified). Altogether it can be stated that, according to model computations, nearly 50–55% of the power required by the calciner can be recovered when the inlet flue gas temperature is 350 °C, and 70–80% when the inlet flue gas temperature is 650 °C.



**Figure II.5:** Ratio between the energy produced in the carbonator and the calciner thermal requirement (Eq. (6)) as a function of the sorbent mean residence time (Eq. (T20)) and of the inlet CaO-to-CO<sub>2</sub> molar ratio (Eq. (4)). The curves are parametric with respect to the carbonator inlet gas velocity and temperature.

## II.4 Final Remarks

Integration of a calcium looping process for CO<sub>2</sub> capture from a combustion plant with concentrated solar power for supplementing the thermal power required for sorbent calcination has been investigated in the present Chapter. A reference case of a 100 MW<sub>th</sub> combustion plant generating 0.20 kmol s<sup>-1</sup> of CO<sub>2</sub> has been considered. Integration of the thermal power generated from the concentrated solar power system during the daytime into a 24 h-cycle steadily operated Ca looping process is accomplished by storing excess calcined sorbent produced during the daytime so that it can be eventually utilized in the calcium looping system during the nighttime. This implies the use of two storage vessels of nearly 2000 m<sup>3</sup>.

Computations indicate that capture efficiency of carbon dioxide approaches 90% when the residence time of the recirculated sorbent is set at nearly 200 s. Sorbent elutriation, emphasized by attrition, accounts for a non-negligible fraction (up to about 30%) of the sorbent make-up. Attrition also emphasizes the difference between the mean diameter of the bed material and that of the parent limestone.

Depending on the temperature of the flue gas fed to the carbonator, as much as 80% of the thermal input from the concentrated solar power system to the calciner can be recovered as valuable thermal power at the carbonator. This rises the overall thermal throughput that can be exploited by the combustion plant equipped with an integrated calcium looping-concentrated solar power system from 100 MW<sub>th</sub> to nearly 150 MW<sub>th</sub> in the selected reference case.

## II.5 Model Nomenclature

$A$	$[\text{m}^2]$	reactors cross-sectional area
$a$	$[\text{mol}_{\text{Ca}} \text{m}^{-2} \text{s}^{-1}]$	attrited flux
$b$	$[\text{mol}_{\text{Ca}} \text{m}^{-2} \text{s}^{-1}]$	bed drain flux
$C$	$[\text{mol} \text{m}^{-3}]$	concentration
$Ca/C$	$[-]$	carbonator inlet Ca (as sorbent)/C (as $\text{CO}_2$ ) molar ratio
$\bar{C}_p$	$[\text{J mol}^{-1} \text{K}^{-1}]$	mean thermal capacity
$d$	$[\text{m}]$	particle diameter
$\bar{d}$	$[\text{m}]$	mean diameter of attrited fragments
$d_{cut}$	$[\text{m}]$	cyclone cut diameter
$DNI$	$[\text{J m}^{-2} \text{s}^{-1}]$	direct normal irradiance
$E$	$[\text{s}^{-1}]$	residence time distribution function
$E^*$	$[\text{mol}_{\text{Ca}} \text{mol}_{\text{CO}_2}^{-1}]$	specific elutriation in the carbonator
$e$	$[\text{mol}_{\text{Ca}} \text{m}^{-2} \text{s}^{-1}]$	elutriated flux
$F_{mp}$	$[\text{mol}_{\text{Ca}} \text{m}^{-2} \text{s}^{-1}]$	make-up flux
$f_p$	$[-]$	fraction of material purged from the calciner
$Fr$	$[-]$	Froude number
$g$	$[\text{mol}_{\text{Ca}} \text{m}^{-2} \text{s}^{-1}]$	internal flux of recirculating material
$g_c$	$[\text{m s}^{-2}]$	gravity constant
$k_a$	$[-]$	attrition constant
$k_{carb}$	$[\text{m}^3 \text{mol}^{-1} \text{s}^{-1}]$	kinetic constant for the carbonation reaction
$n_c$	$[-]$	cyclone collection efficiency exponent
$P$	$[\text{Pa}]$	pressure
$P_0$	$[\text{m}^{-1}]$	size distribution function for the raw sorbent after primary fragmentation
$P_a$	$[\text{m}^{-1}]$	size distribution function for sorbent fragments upon attrition
$q_{th}$	$[\text{J m}^{-2} \text{s}^{-1}]$	thermal flux required by the calciner
$q_{th,carb}$	$[\text{J m}^{-2} \text{s}^{-1}]$	thermal flux produced by the carbonator
$R$	$[\text{J mol}^{-1} \text{K}^{-1}]$	ideal gas constant
$R_R$	$[-]$	gas recycle ratio
$S$	$[\text{m}^2]$	surface of the heliostats field
$s$	$[\text{mol}_{\text{Ca}} \text{m}^{-2} \text{s}^{-1}]$	flux of shrinking particles
$T$	$[\text{K}]$	temperature
$t$	$[\text{s}]$	time
$t^*$	$[\text{s}]$	time for particle complete carbonation
$t_{day}$	$[\text{s}]$	daylight duration
$t_{night}$	$[\text{s}]$	nighttime duration
$u$	$[\text{m s}^{-1}]$	gas velocity
$u_{mf}$	$[\text{m s}^{-1}]$	minimum fluidization velocity
$u_{\infty}$	$[\text{m s}^{-1}]$	particle terminal velocity
$W$	$[\text{mol}_{\text{Ca}} \text{m}^{-2}]$	bed inventory
$X_{Ca}$	$[-]$	instantaneous Ca carbonation degree
$\bar{X}_{Ca}$	$[-]$	mean Ca carbonation degree
$X_{\text{CO}_2}$	$[-]$	$\text{CO}_2$ capture efficiency

### Greek symbols.

$\beta$	$[-]$	carryover parameter
$\Delta H$	$[\text{J mol}^{-1}]$	enthalpy change of the calcination reaction
$\varepsilon_{mf}$	$[-]$	bed voidage at minimum fluidization

$\eta_{rec}$	[-]	ratio between the energy produced in the carbonator and the calciner thermal requirement
$\rho$	[kg m <sup>-3</sup> ]	solid density
$\rho_g$	[kg m <sup>-3</sup> ]	gas density
$\rho_{mol}$	[mol m <sup>-3</sup> ]	molar density
$\tau$	[s]	mean solid residence time
$\chi_{CO_2}$	[-]	gas volume variation factor
$\omega_c$	[-]	cyclone collection efficiency

***Superscripts and subscripts.***

<i>CALC</i>	relative to the calciner (see Figure II.1)
<i>CALC"</i>	relative to the fluxes from the calciner to the reservoir "R2" (see Figure II.1)
<i>CARB</i>	relative to the carbonator (see Figure II.1)
<i>CL</i>	carbonated lime (CaCO <sub>3</sub> /CaO mixture)
<i>EQ</i>	equilibrium
<i>GAS</i>	relative to the gaseous species
<i>i</i>	granulometric class
<i>IN</i>	inlet
<i>L</i>	lime (CaO)
<i>MAX</i>	maximum value
<i>mp</i>	make-up
<i>n</i>	coarsest granulometric class
<i>OUT</i>	outlet
<i>R1</i>	relative to the reservoir "R1" (see Figure II.1)
<i>R2</i>	relative to the reservoir "R2" (see Figure II.1)

# Chapter III. Heat Transfer in Directly Irradiated Fluidized Beds

## III.1 Introduction

In the present Chapter, a deeper characterization of the direct interaction between a concentrated simulated solar radiation and a fluidized bed is performed. Radiative heat transfer and lateral dispersion of the incoming radiative flux are here characterized by time-resolved infrared mapping of the surface of a directly-irradiated gas–solid dense fluidized bed. Possible improvements of the interaction between radiative flux and fluidized particles induced by tailoring the bed hydrodynamics is assessed. To this end, the effect of localized injection of chains of bubbles from a nozzle located in the proximity of the radiation focal point is investigated. The experimental facility is intentionally designed to have a cross-sectional area much larger than the spot irradiated by the solar simulator. This design choice allows the assessment of the interaction between the irradiated core and the surrounding bulk of the bed with minimal wall effects.

## III.2 Experimental Apparatus, Diagnostics and Materials

The experimental apparatus is represented in Figure III.1. Its main components are:

- i) A fluidized bed reactor with a gas preheater and a mass flow control system;
- ii) A temperature and pressure measurement system of the bottom bed;
- iii) A simulated solar radiation source, consisting of a short-arc Xe-lamp and of an elliptical reflector;
- iv) An infrared camera to map the bed surface temperature;
- v) A Bubble Generation System (BGS) connected to a submerged nozzle located along the central axis of the fluidized bed.

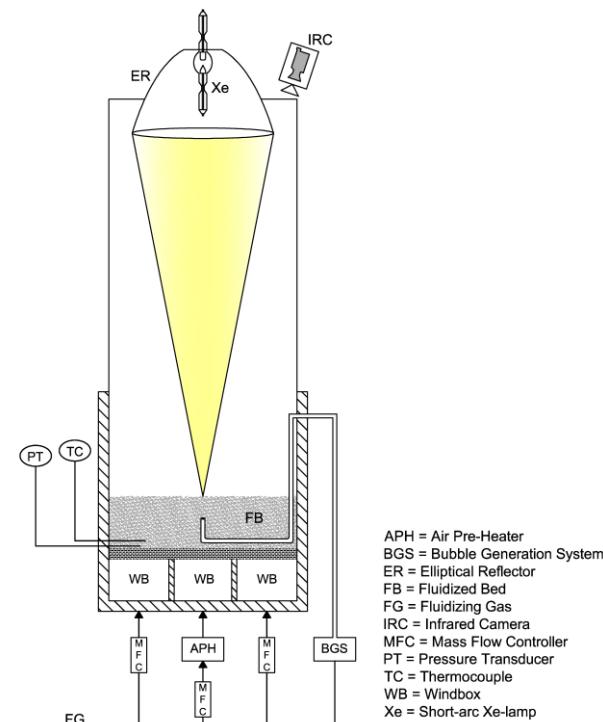


Figure III.1: Outline of the experimental apparatus.

### III.2.1 Fluidized Bed Reactor

The fluidized bed column is made of stainless steel (AISI 304) and has an internal square cross section of 0.78 m×0.78 m, 0.6 m tall. The gas distribution plate consists of a set of stainless steel wire mesh supported by a metallic grid. The windbox, 0.2 m tall, is compartmented in three sections independently fed by three mass flow meters (Mass Stream D-6380), each of 200 Nm<sup>3</sup> h<sup>-1</sup> maximum rate. The gaseous stream fed to the central section of the windbox can be preheated through a 5 kW<sub>el</sub> electric preheater. Three temperature and pressure taps are located at the bottom of the fluidized bed close to the distributor. Calibrated J-type thermocouples and piezoresistive pressure transducers (Keller PR-33X; full scale: 0.1 bar; accuracy: 0.15%FS) were used to monitor the bed temperature and the fluidization conditions, respectively. A PC coupled with an A/D converter (NI-9213 and NI-9201 analogue input modules plugged into a NI-9174 Compact DAQ 4-Slot USB Chassis) was used to log pressure and temperature signals. Temperatures at the bottom of the bed, mass flow rates and pressures were continuously sampled at 1 Hz and post-processed with a procedure developed in LabVIEW environment.

### III.2.2 Solar Simulator: Short-Arc Xenon Lamp and Optical Reflectors

A short-arc Xe lamp was chosen as source of solar simulated radiation due to the similarity of its emission spectrum to that referred to terrestrial sunlight (Figure III.2). Short-arc Xe-lamps feature two electrodes made of doped tungsten and enclosed in a quartz bulb glass filled with pure Xe at a pressure of 8–10 bar. The quartz material is required to withstand the high temperature and pressure achieved during the exercise of the lamp. High purity or doped quartz are used as bulb envelope: the former is used when UV radiations are needed, while the latter when UV radiations need to be shielded. When doped quartz is used, the spectral emission of the lamp starts from about 240 nm, and lamps are commonly referred as Ozone Free (OFR). The cathode of a Xe-lamp is relatively small and with a sharp tip to enhance the electrons emission. On the contrary, the anode is considerably bigger as it has to dissipate a huge quantity of heat: the high speed electrons emitted by the cathode continuously penetrate the anode and a large amount of energy is converted into heat. A picture of a short-arc Xe-lamp is shown in Figure III.3.

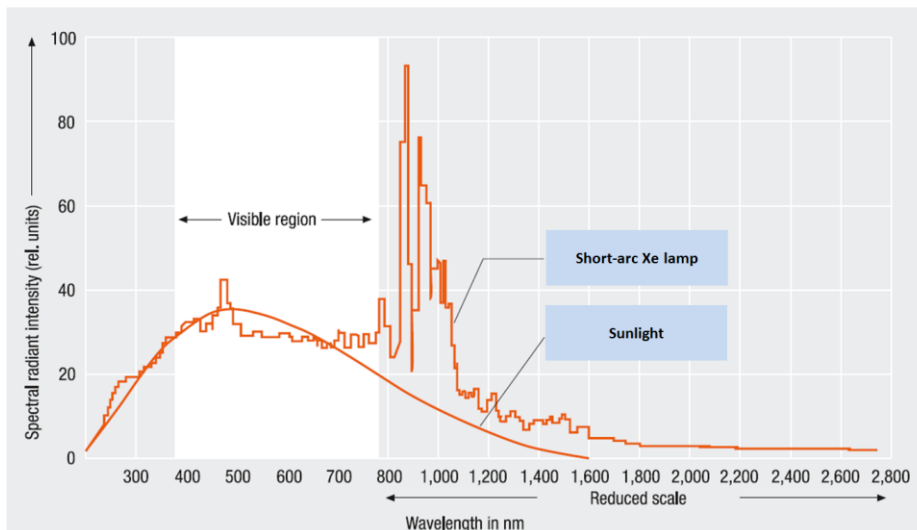


**Figure III.2:** Spectral distribution of radiant intensity of a typical short arc Xe-lamp and that of the sun (represented as a 6200 K black body radiator).

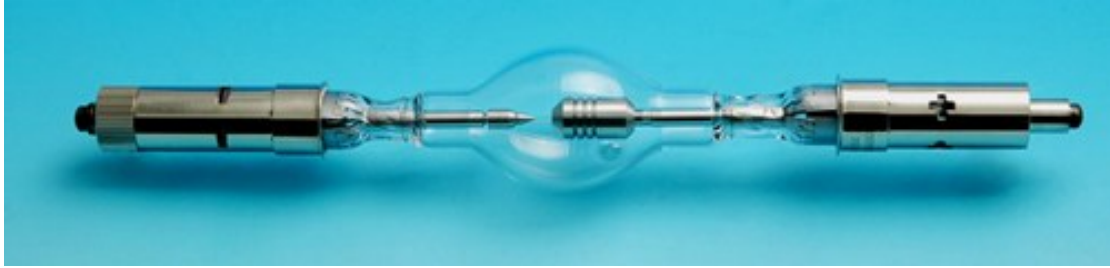


**Figure III.3:** Picture of a short-arc Xe-lamp. Left-electrode, cathode; right-electrode, anode.

When a high potential difference is applied between the electrodes, the xenon gas is ionized and an electric arc is formed. As the distance between the two electrodes is not high, the arc region is very small and for many applications these lamps come very close to the ideal of a point source: this is a key feature as it enables the accurate location of the lamp in the focal point of an optical reflector. The lamp used for the experiments is an OFR model with a power of  $4 \text{ kW}_{\text{el}}$ . To address the light produced by the Xe-lamp towards a proper direction, an optical reflector must be used. The geometry of the reflector is crucial, as it determines the main features of the produced beam. Two reflectors were tested: a parabolic shaped one, which was supplied by the manufacturer together with the Xe-lamp, and an elliptical reflector specifically chosen to achieve a high concentration ratio of the luminous radiation. A parabolic reflector collects the radiations from a source located at its focal point and reflect them as a collimated beam, parallel to the axis of the parabola, and with a dimension of the same order of magnitude of the parabolic reflector aperture. The produced beam is then focused at infinite. Differently, an elliptical reflector collects the radiations from a source located at its focal point and redirect them into a second fixed focal point: single ray-light arising from the first focal point passes through the second focal point after a single reflection. The produced beam is then focused into the second focal point of the reflector. As every real light source has some finite extent, points of the source that are not exactly at the focus of the reflector will be magnified and defocused at the image. Figure III.4 reports a sketch of the two reflectors. The elliptical reflector used for the experimental test is made by Optiforms and it is characterized by a distance between the two conjugated foci of 1.585 m. The optical coating is made of aluminium overcoated with silicon dioxide (generally known as protected aluminium). It exhibits over 90% reflectance across the visible spectrum and has better handling characteristics with respect to pure aluminium.

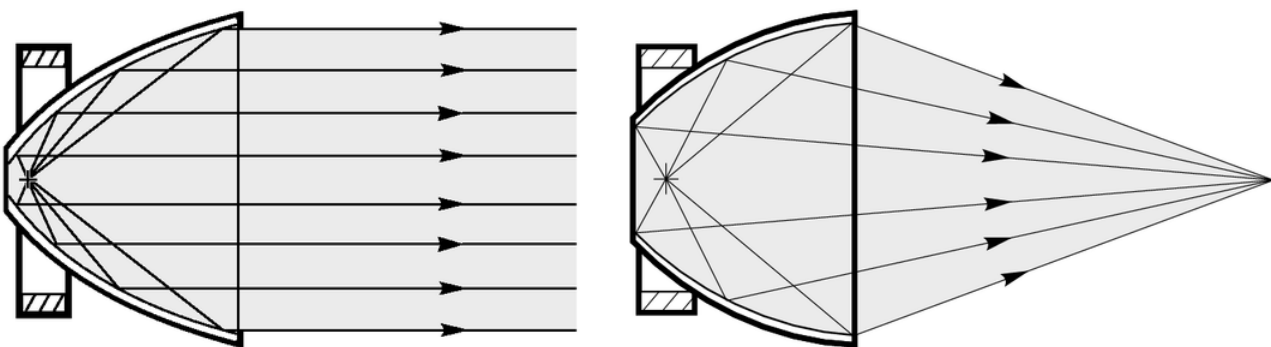


**Figure III.4:** Sketch of a parabolic shaped reflector (left) and of an elliptical reflector (right).

### **III.2.3 Bubble Generation System**

The discrete BGS is composed of a cylinder hosting a movable piston connected to a submerged nozzle (8 mm ID), through which single bubbles are injected into the bed. A fine metallic net (finer than 50  $\mu\text{m}$ ) is located at the nozzle tip to prevent backflow of bed solids. The piston stroke and the pressure of the gas contained in the piston chamber can be adjusted in order to set the volume of gas released after a single piston movement. The actuation of the system is realized by alternating the opening and closing of a 12 V electrical circuit driven by a relay controlled by a NI-9263 analogue output module. A LabVIEW script is used to set the circuit opening/closing time, so to produce a chain of bubbles at the desired frequency in the 0–1 Hz range. Higher frequencies could not be used as they would not guarantee complete filling of the piston chamber.

### **III.2.4 Thermal Infrared Camera**

The thermal infrared camera used for the measurement of the bed surface temperature is an Optris PI-400. It is schematically shown in Figure III.5. It features a 25  $\mu\text{m} \times 25 \mu\text{m}$  detector and has a digital resolution of 382 $\times$ 288 pixels, with a maximum acquisition frame rate of 80 Hz. The temperature is calculated by the camera on the basis of the emitted infrared radiation in the 7.5–13  $\mu\text{m}$  spectral range. It is important to underline that the spectral range detected by the infrared camera does not overlap with the emission spectrum of the short-arc Xe-lamp (0.2–2  $\mu\text{m}$ ), so the error related to the part of the incident radiation which is reflected by the fluidized particles can be considered negligible. The camera is coupled with a tele-lens to measure the temperature in an observation window of 0.35 m $\times$ 0.26 m, at a distance of 1.5 m and with a pixel resolution of 0.9 mm, just at the centre of the fluidized bed surface. The camera tilting angle with respect to the reactor vertical axis is small ( $\sim 15^\circ$ ), thus the image distortion is barely detectable. Four calibration ranges can be used during the image acquisition: –20–100, 0–250, 150–900 and 200–1500  $^\circ\text{C}$ , once a proper value of the emissivity is set for the investigated material. The choice of the range is of primary importance, as no changes can be done after the images have been acquired: any information that falls out of the chosen range is lost and only the minimum/maximum value of the calibration range will be displayed in this case.

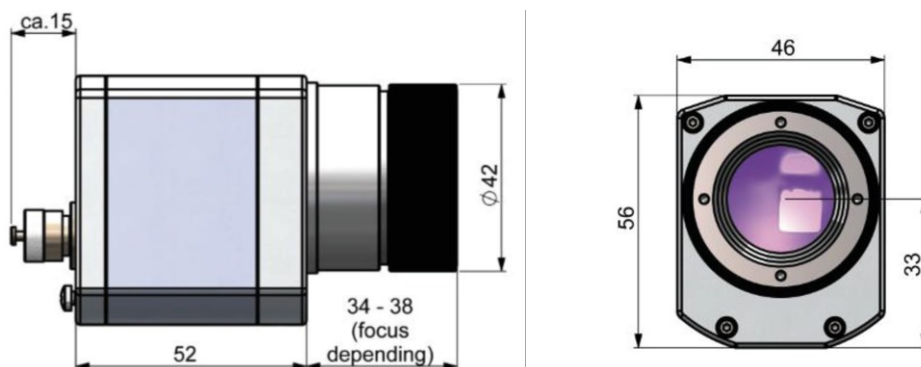


**Figure III.5:** Sketch of the thermal infrared camera. Dimensions are expressed in mm.

### **III.2.5 Capacitance Probes**

Capacitance probes measure the change in the capacitance of a condenser and were used to characterize the features of the bubbles generated by the BGS. The probes used (custom-made

ASP-2-ILA/SP needle capacitance probe coupled with an MTI Instruments AccuMeasure 9000 amplifier) are characterized by a needle shape so as to disturb the fluidization behaviour as little as possible (Figure III.6). When a capacitance probe is immersed into a fixed bed, a stable d.c. voltage signal, proportional to the bed material permittivity, is generated. When the bed becomes fluidized, the temporal variation of the porosity near the control volume of the probe causes a continuous change in the capacitance, which in turn results into a proportional variation of the d.c. voltage signal. The passage of a bubble through the control volume of a probe is easily recognized due to the generation of a Gaussian-like peak into the time-voltage space. By the analysis of the probe signal, it is possible to obtain several information, like the mean pierced length of a bubble and its mean rise velocity.



**Figure III.6:** Picture of a capacitance probe. The poles are the protruding needle and the enclosing metal tube.

### **III.2.6 Gas Meter**

The gas meter (Figure III.7) was used to measure the air flow produced by the discrete BGS. When a continuous gas stream is sent through the gas meter for a fixed time, the front needles indicate the total volume of gas that has passed through the instrument. If the flow rate of a continuous stream needs to be determined, the acquisition is performed for a fixed time and then the total volume is divided by the elapsed time. In order to estimate the features of the discrete BGS, the acquisition was performed for a total number of about 100 bubbles.



**Figure III.7:** Picture of the gas meter.

### **III.2.7 Radiative Heat Flux Sensor**

The radiative heat flux sensor (Figure III.8) was used for the characterization of the solar simulator. This instrument measures the radiative heat flux impinging on its surface. The transducer

is a differential thermocouple that measures the temperature difference between the centre and the circumference of a thin circular foil disk, which is bonded to a circular opening in a cylindrical heat sink. The foil and body are made of complementary thermocouple alloys and produce an output voltage which is directly proportional to the impinging heat flux. The proportionality constant is given by the manufacturer, which provides a certificate of calibration. The sensor is also water-cooled: a continuous water flow is indeed used to protect the sensor against over-heating and to provide a good heat sink (required to achieve an accurate measurement). A sapphire window (spectral range 0.3–5  $\mu\text{m}$ ) is located in front of the sensing element to screen out the convective heat flux, so that only the radiative flux is measured. The window is placed directly on the water-cooled copper surface to minimize its heating, but is not in contact with the sensing element itself. The calibration constant of the heat flux is equal to  $8.751 \text{ W cm}^{-2} \text{ mV}^{-1}$ . The output from the sensor is linear and the calibration is valid up to 15 mV. Between 15 and 20 mV the output is no more linear, while output values over 20 mV can permanently damage the sensor.

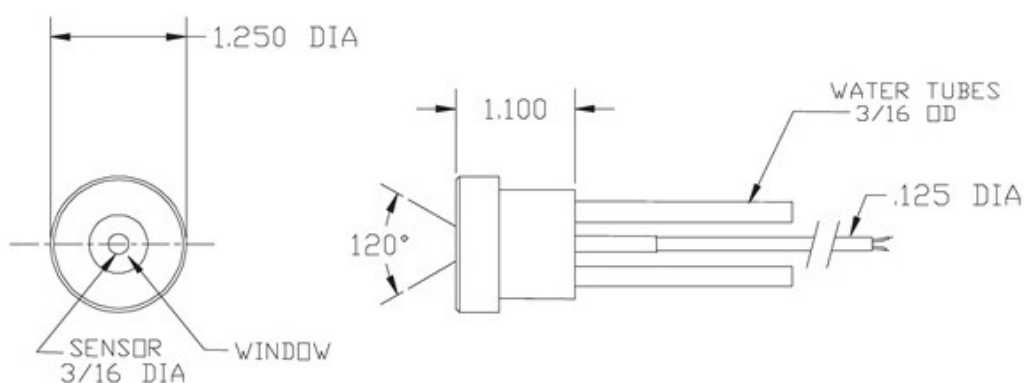


**Figure III.8:** Sketch of the radiative heat flux sensor. Dimensions are in inches.

### III.2.8 Materials

The fluidizing gas was technical air. The bed material consisted of SiC, a potential good absorber of the radiation due to its large emissivity and dark colour. The properties of the SiC powder are reported in Table III.1. The minimum fluidization velocity of this material displays limited change with temperature. The bed height under fixed bed conditions was set equal to 0.2 m.

Density [ $\text{kg m}^{-3}$ ]	Size range [ $\mu\text{m}$ ]	Size standard deviation [ $\mu\text{m}$ ]	Sauter mean diameter [ $\mu\text{m}$ ]	Geldart classification group	$U_{mf}$ [ $\text{m s}^{-1}$ ]
3210	50–350	55	127	B	0.018 (@ 20 °C) 0.016 (@ 600 °C)

**Table III.1:** Physical properties and fluidization features of the SiC powder.

## III.3 Characterization

### III.3.1 SiC Emissivity

SiC effective emissivity was determined by measuring its temperature with both the thermal infrared camera and a K-type thermocouple at different bed temperatures under bubbling fluidized bed conditions. The estimated value, nearly 0.9, is consistent with values reported in the literature (Chen, 2003; Green and Perry, 2008).

### **III.3.2 Xe-Lamp Thermal Power**

#### **III.3.2.1 Parabolic Reflector**

In order to characterize the heat flux distribution of the 4 kW<sub>el</sub> Xe-lamp coupled with the parabolic reflector, the lamp was focused on a target board whose surface temperature distribution was measured by the thermal infrared camera: the measured temperatures were then related to the impinging flux through an energy balance. The lamp and the board were arranged so that the luminous beam were orthogonal to the board. An insulating board was used as target material so that the lamp draws an imprint on the surface. Only a mean flux could be estimated due to the homogenization of the surface temperatures. The target board was also coated with a high-temperature-resistant matt black paint to increment its spectral absorbance. The radiometric images acquired by the thermal camera consists in false colour images which can be exported as 382×288 matrixes of temperature values. The space distance between two adjacent temperature values was estimated through the use of a target grid positioned on the insulating board. Images of the board surface were taken once a steady state was reached. More in detail, images in both the 0–250 °C and 150–900 °C ranges were acquired and merged through an “if” function to obtain a single image covering the full 0–900 °C range. Moreover, the temperature of the opposite face of the insulating board was measured in three different points with the use of a K-type thermocouple. The energy balance equation written on the insulating board includes radiative, conductive and convective contributes. The equation reads:

$$\Phi\alpha = \varepsilon\sigma T_S^4 + \frac{\overline{K_T}(T_S - T_I)}{s} + h^{CN}(T_S - T_{Air}) \quad (\text{III.1})$$

where:

$\Phi$  is the impinging radiative flux;

$\alpha$  and  $\varepsilon$  are the absorption and emission coefficient of the board, respectively;

$\sigma$  is the Stefan–Boltzmann constant;

$T_S$  and  $T_I$  are the temperature of the surface and of the opposite face of the board, respectively;

$\overline{K_T}$  is the mean thermal conductivity of the board between  $T_S$  and  $T_I$ ;

$s$  is the thickness of the board;

$h^{CN}$  is the convective heat transfer coefficient;

$T_{Air}$  is the temperature of the air and of the surrounding ambient.

The equation was solved for each of the interested cells of the 382×288 matrix in order to obtain the spatial flux distribution.  $\alpha$  and  $\varepsilon$  were both set equal to 0.9 (grey-body behaviour assumption). Concerning the conductive term, an approximation was made as the temperature of the opposite board face was measured only at three different coordinates. More in detail, the ratio between the conductive and the radiative contribute was estimated for the three available data: as this ratio resulted to be almost constant, the conductive contribute was taken into account by adding to each matrix cell a fixed percentage of the radiative flux. The conductive contribute resulted to account

for a mean value of 4.6% of the radiative contribute. Concerning the convective contribute,  $T_{Air}$  was set equal to 25 °C, while the heat transfer coefficient was estimated using Eq. (III.2)<sup>2</sup>:

$$Nu = 0.68 + \frac{0.67Ra^{1/4}}{\left[1 + \left(\frac{0.492}{Pr}\right)^{9/16}\right]^{4/9}}; \quad Ra \leq 10^9 \quad (III.2)$$

The Rayleigh number for an inclined plate is defined by replacing, in the classic equation, the gravitational acceleration with only its component along the direction parallel to the inclined plate. Considering a mean temperature for the insulating board of 200 °C, and the side of the board (50 cm) as characteristic length, the convective heat transfer coefficient results to be equal to  $h^{CN}=5.8 \text{ W m}^{-2} \text{ K}^{-1}$  ( $Pr=0.7$ ;  $Ra=8 \cdot 10^8$ ;  $Nu=87$ ).

Results of the energy balance are depicted in a 3D surface plot (Figure III.9) and a contour chart (Figure III.10). The heat flux of the Xe-lamp coupled with the parabolic reflector is quite diluted, with a peak value of only  $50 \text{ kW m}^{-2}$ . The imprint leaved on the board is relatively wide, and it can be approximated by a circumference of 30 cm diameter. Even considering a more restricted area with a diameter of 5 cm (Figure III.10), a mean flux of only  $28 \text{ kW m}^{-2}$  is obtained, with a total power of 55 W. The mean heat flux and the total power are both too low, thus it is concluded that the supplied parabolic reflector is not suitable to design a simulator of a solar concentrated radiation.

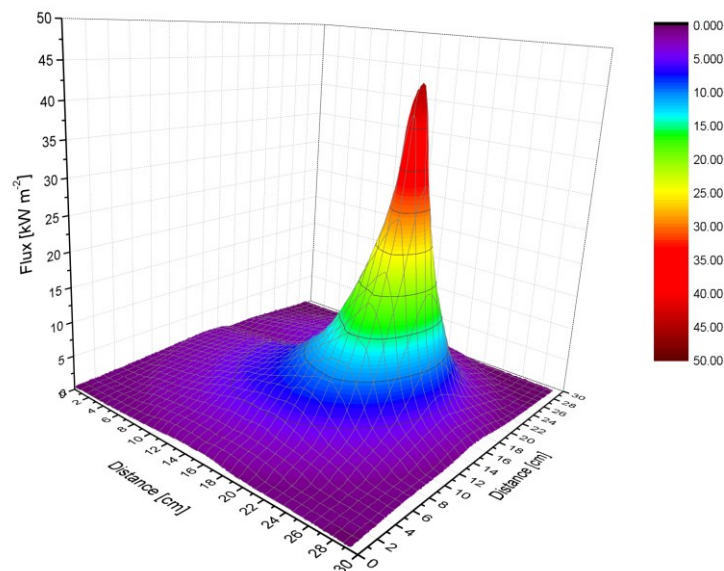


**Figure III.9:** Surface plot of the spatial distribution of radiative heat flux obtained through the parabolic reflector.

<sup>2</sup> [www.thermalfluidscentral.org/encyclopedia/index.php](http://www.thermalfluidscentral.org/encyclopedia/index.php)

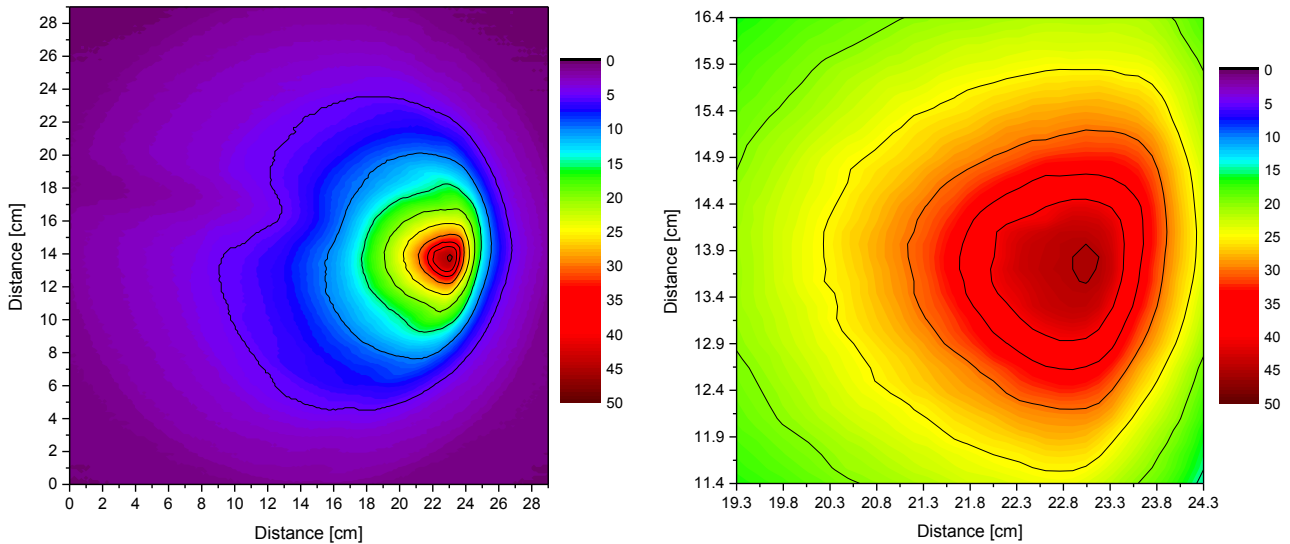


**Figure III.10:** Contour chart of the spatial distribution of radiative heat flux obtained through the parabolic reflector. Left: overall imprint; right: zoom of a limited section of 5 cm diameter.

### III.3.2.2 Elliptical Reflector

The characterization of the heat flux distribution of the Xe-lamp coupled with the elliptical reflector was performed using the radiative heat flux sensor and the thermal infrared camera. More specifically, the heat flux sensor was used to measure the concentrated radiative flux while the infrared camera was used to record the spatial distribution of the incident radiative flux. To this end, the simulated solar beam was focused onto the bed surface of SiC particles under no-flow conditions and thermal maps of the bed surface were acquired under steady state conditions assuming emissivity equal to 1. At the same time and under the same operating conditions, the radiative flux was measured by the heat flux sensor at different locations at the bed surface. Infrared maps and data from the heat flux sensor were used to correlate the surface bed temperature and the radiative incident flux. The flux measured by the radiative sensor linearly correlated with the fourth power of the absolute surface bed temperature (which is proportional to the incident flux according to Stefan–Boltzmann equation), as it is possible to observe in Figure III.11.

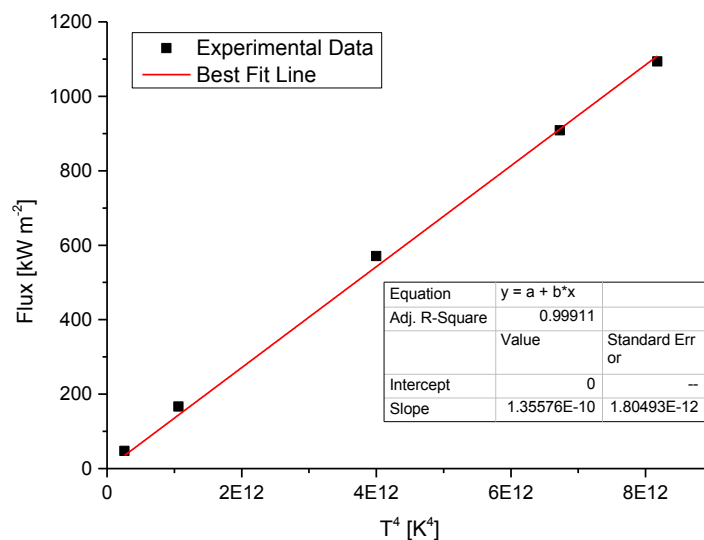


**Figure III.11:** Experimental correlation between the absolute surface bed temperature obtained assuming an emissivity value of 1 and the heat flux value measured by the sensor.

The correlation factor was used to convert the temperature map into a map of the heat flux spatial distribution (Figures III.12–13). A peak flux of  $1100 \text{ kW m}^{-2}$  was obtained in the focal point. The total power irradiated to the bed surface was  $1270 \text{ W}$ , estimated by integrating the radiative flux over the whole bed area. The total power decreased to  $1000 \text{ W}$  and  $700 \text{ W}$  when square areas centred on the focal point of lateral size  $0.10 \text{ m}$  and  $0.05 \text{ m}$  were considered, respectively. Both the heat flux values and the total power are considerably larger than the ones achieved with the parabolic reflector. The  $4 \text{ kW}$  short-arc Xe-lamp coupled with the elliptical reflector can then be successfully used to simulate a solar concentrated radiation.

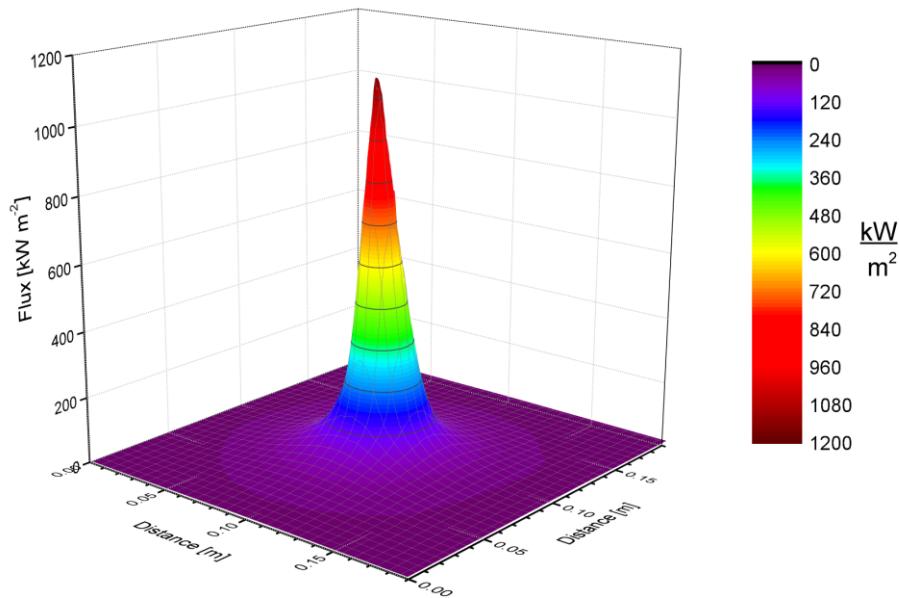


**Figure III.12:** Surface plot of the spatial distribution of radiative heat flux incident on the bed surface obtained through the elliptical reflector.

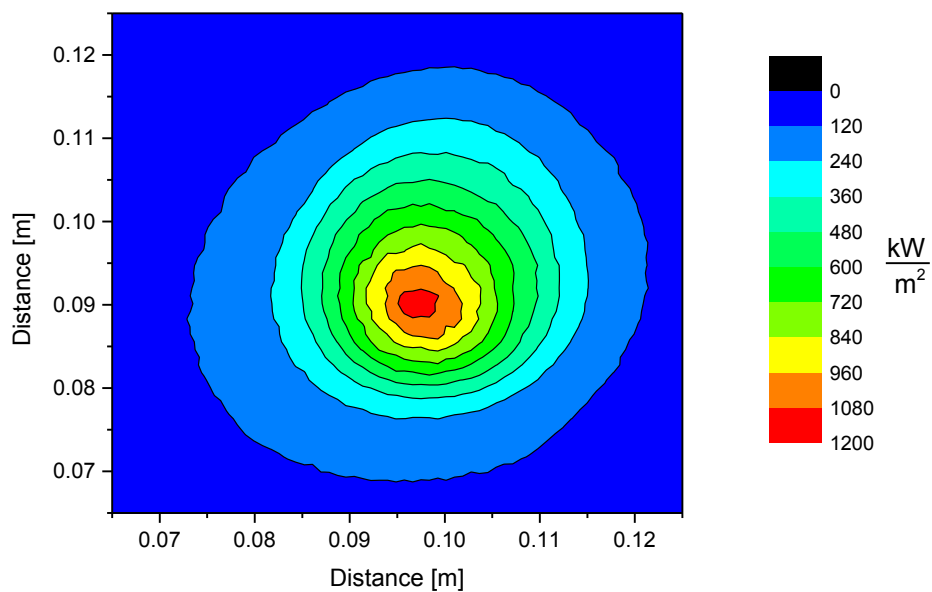


**Figure III.13:** Contour chart of the spatial distribution of radiative heat flux incident on the bed surface obtained through the elliptical reflector.

### **III.3.3 Bubble Generation System Features**

The BGS was optimized to generate bubbles with a diameter ( $D_b$ ) of 0.065 m. Its characterization in terms of diameter and rise velocity of the generated bubbles was performed using both the capacitance probes and the gas meter. The analysis with the capacitance probes was carried out following the experimental procedure proposed by *Werther and Molerus* (1973). A system of two aligned probes, with a fixed distance between them, was immersed in the fluidized bed with the tip of the probes centred above the nozzle. The probes were positioned far above the nozzle so to make the bubbles completely grow before the measure take place. Data acquired during a 60 s test performed with a bubble generation frequency of 0.2 Hz and a data acquisition frequency of 1000 Hz are reported in Figure III.14: each peak corresponds to the passage of a single bubble. Analysing the zoomed part of the chart in Figure III.14 it is possible to observe the existence of a time delay between the two signals: this delay is a direct information of the time that a bubble requires to travel for a distance equal to the space between the needles of the two probes. The velocity of the rising bubbles can then be evaluated by computing the time delay between the two signals and by considering the probes distance. In order to evaluate a mean time delay, averaged on the signal duration, it is first necessary to clean the data by removing the part of the signal generated by the variations of porosity of the dense phase. The discrimination between the dense phase signal and the bubble signal was performed by choosing a reference voltage ( $V_R$ ) that can discern the nature of the signal. To establish the reference value, an amplitude distribution curve was generated from the experimental data and  $V_R$  was set in the region in which the curve is nearly constant at relatively low voltage values. The distribution curve is plotted in Figure III.15: from its analysis, a reference voltage of 3.5 V was set. Figure III.16 reports a smaller section of the voltage-time plot before and after the cleaning data operation. Once the data have been filtered, a MATLAB script which makes use of the “*finddelay*” function was used to estimate the temporal delay between the two probes signal. The distance between the two probes was measured with the use of a Vernier calliper. A temporal delay of 19.7 ms was obtained; considering the measured probes distance of 11.2 mm, it resulted into a bubble rising velocity of  $0.57 \text{ m s}^{-1}$ . Finally, the bubble mean diameter ( $D_{bubble}$ ) was evaluated according to Eq. III.3 (*Kunii and Levenspiel*, 1991):

$$D_{bubble} = \frac{\left(\frac{u_{bubble}}{0.711}\right)^2}{g} \quad (\text{III.3})$$

where  $u_{bubble}$  is the bubble mean rising velocity and  $g$  is the gravitational constant. Solution of Eq. (III.3) returns a bubble diameter of nearly 6.5 cm. The bubble mean diameter was further evaluated through the gas meter. The flow of 100 bubbles resulted into a measured volume of  $13.7 \text{ dm}^3$ , from which a bubble spherical diameter of 6.4 cm is obtained, to confirm the above estimation. Considering a bubble release frequency of 1 Hz, the increase of fluidization velocity due to bubble injection is negligible if the total cross section of the fluidized bed is taken into account ( $2.2 \cdot 10^{-4} \text{ m s}^{-1}$ ), whereas it amounts to  $0.034 \text{ m s}^{-1}$  if the gas superficial velocity is referred to a cross sectional area equal to  $D_b \times D_b$ .

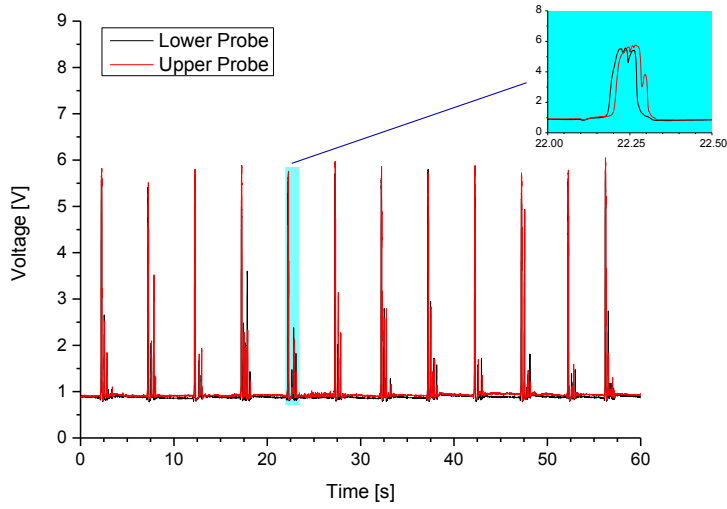


**Figure III.14:** Voltage-time plot of the two capacitive probes.

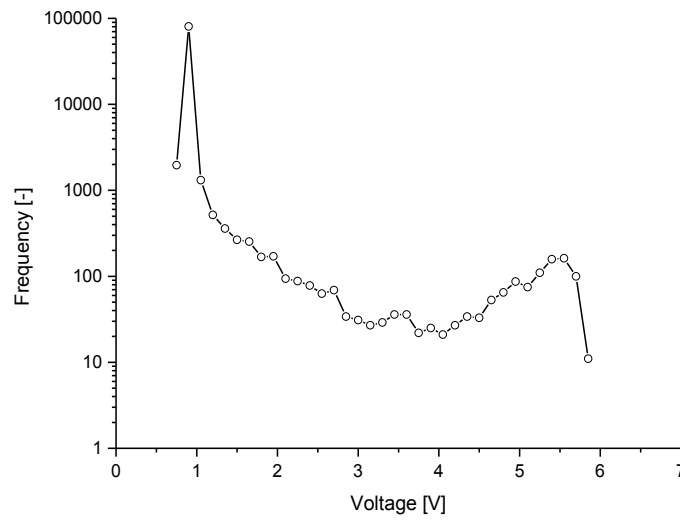


**Figure III.15:** Amplitude distribution curve of the probes signal.

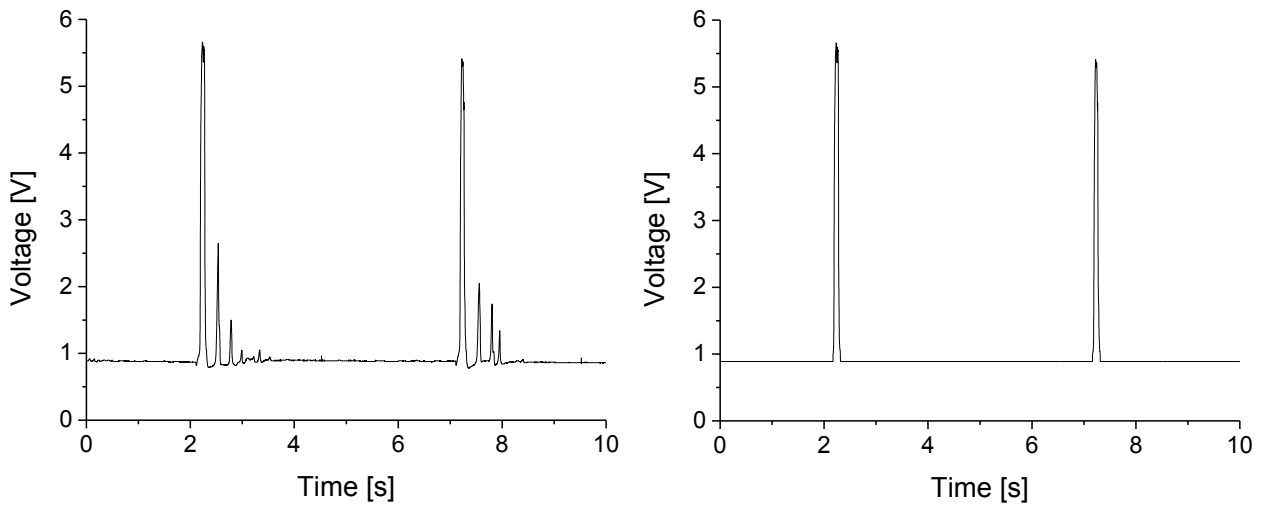


**Figure III.16:** Voltage-time plot before and after the noise reduction operation.

### III.4 Experimental Procedure and Operating Conditions

At the beginning of the test the lamp beam was carefully focused at the centre of the fluidized bed surface. Eventually, the Xe lamp was powered off, the bed was fluidized shortly at a fluidizing gas velocity ( $U$ ) of about  $0.07 \text{ m s}^{-1}$  and heated up to a temperature of  $25\text{--}30 \text{ }^\circ\text{C}$  using the air preheater, in order to reach an almost constant base-line for each experiment. Once the pre-set temperature was established, iterated acquisition of time-resolved thermal maps of the bed surface was started at a sampling frequency of 27 Hz, then the Xe lamp was turned on. Each test lasted about 15 minutes. Experiments were carried out at different gas superficial velocities (0 to  $0.1 \text{ m s}^{-1}$ ) ranging from fixed bed to freely bubbling fluidized bed conditions.

In most experiments the temperature of the bed surface exhibited wide time- and space-fluctuations, which could not be captured with a single calibration range of the infrared camera. Hence, experiments at given fluidization and irradiation conditions were iterated with different calibration ranges of the infrared camera, and multiple acquisitions of the bed surface temperature were performed. Of course, the time-series corresponding to experiments with different calibration ranges were not synchronized to each other, but could be cumulatively analysed on a time-averaged basis.

Some experiments were performed with injection of additional bubbles in the close proximity of the radiation focal point, using the previously described BGS. The submerged nozzle was located inside the fluidized bed and aligned with the focal point of the simulated solar beam. The influence of the spatial gap between the nozzle and the bed surface –values of 0.09 m and 0.03 m were considered– was investigated at different gas superficial velocities, while keeping the bubble generation frequency at 1 Hz. The 0.09 m gap was large enough to give the bubbles space to completely grow before bursting. The 0.03 m gap gave rise to a different hydrodynamical pattern, with bubbles formation and eruption taking place at the same time. Table III.2 summarizes the experimental conditions tested. When the BGS was used,  $U$  ranged from  $0.004 \text{ m s}^{-1}$  to  $0.063 \text{ m s}^{-1}$ .

The thermal maps obtained with the infrared camera were post-processed to get the time-resolved temperature profiles at selected measurement points. In particular, the attention was focused on the focal point of the beam, where a maximum radiative flux of  $1100 \text{ kW m}^{-2}$  is achieved. Time-series of temperature recorded at this point were worked out to obtain temperature probability density functions ( $P(T)$ ), time-averaged temperature and temperature standard deviation. For the experimental tests in which more than one calibration range was used, data sets corresponding to different calibration ranges were merged and jointly analysed after optimal selection of the temperature cut-off of each set. Time-averaged temperatures ( $T_{mean}$ ) and standard deviations ( $\sigma_T$ ) were then estimated according to Eqs. (III.4)–(III.5):

$$T_{mean} = \int_0^{T_{MAX}} T \cdot P(T) dT \quad (\text{III.4})$$

$$\sigma_T = \sqrt{\int_0^{T_{MAX}} (T - T_{mean})^2 \cdot P(T) dT} \quad (\text{III.5})$$

The statistics was always referred to time-series obtained when a steady state (on a time-averaged basis) was established (less than 5% change of time-averaged properties).

Without BGS	With BGS	
	nozzle–surface gap: 0.09 m	nozzle–surface gap: 0.03 m
$U$ [m s <sup>-1</sup> ]	$U$ [m s <sup>-1</sup> ]	$U$ [m s <sup>-1</sup> ]
0	0.004	0.008
0.013	0.015	0.015
0.019	0.022	0.022
0.031	–	–
0.037	0.044	0.043
0.050	–	–
0.062	0.063	0.063
0.073	–	–
0.087	–	–
0.099	–	–

**Table III.2:** Operating conditions of the tests. The gas superficial velocity ( $U$ ) reported in the Table refers to air feeding to the windbox. Additional air fed to the nozzle, when present, represents a negligible fraction of the overall gas flow rate.

## III.5 Results and Discussion

### III.5.1 Analysis of Thermal Maps of the Bed Surface Upon Irradiation

Figures III.17–21 report selected sequences of thermal maps of the bed surface captured by the infrared camera at a sampling rate of 27 Hz during experiments carried out at different fluidizing gas velocities without injection of additional bubbles. The frames at 0 s in Figures III.17 and III.18 correspond to the time just before the lamp was turned on. Figure III.17 refers to fixed bed conditions, as no fluidizing gas was fed to the bed. Data in Figures III.17–18 were acquired within the 200–1500 °C calibration range. Accordingly, the dark blue colour corresponds to temperatures of 200 °C and less, whereas the white colour corresponds to temperatures of 1500 °C and higher. Figure III.17 reports the dynamic establishment of the fingerprint of the simulated solar radiation on the bed surface. 20 s after lamp ignition, temperatures exceeding 1500 °C were recorded in the focal zone. After about 160 s, surface temperature was steady in the focal zone, while increasingly extended areas of the bed turned hotter away from the focal point, under the combined effect of transient heat transfer in the bulk of the bed and energy re-irradiation from the surface of the bed to the environment. Figure III.18 reports thermal maps obtained when the bed was kept at incipient fluidization ( $U=0.018$  m s<sup>-1</sup>, see Table III.2). As for fixed bed conditions, it is possible to observe the formation of a central hot zone whose temperature increases along with time. Remarkably, several micro-bubbles (1–5 mm diameter) became apparent in this case within the imprint of the lamp, that were not observed when the radiative source was turned off. This phenomenon is explained by considering the excess gas superficial velocity that establishes in the hot focal zone and flows as small bubbles when the bed, hence the fluidizing gas, is heated up.

Figures III.19–20 report two sequences of thermal maps of the upper surface of the fluidized bed acquired with calibration range 0–250 °C under moderate freely bubbling conditions ( $U=0.073$  m s<sup>-1</sup>). The sequences refer to a time-window shorter than those previously reported, to better follow the detailed dynamics of the bed associated with individual bubble eruptions. The analysis of the sequences demonstrates that bubble bursting reduces local overheating of the bed surface at the focal point along two different mechanisms: 1) bubbles promote coverage of the hot

central region by “avalanching” of colder particles located away from the focal point (Figure III.19); 2) bubble bursting promotes ejection and displacement of hot particles from the focal point toward neighbouring regions of the bed (Figure III.20). Altogether, bubble eruption provides intermittent renewal of the fluidized bed surface at the focal point. Rapid heating up of the bed material is observed at the focal point between successive bubble eruptions, whose extent depends on the time elapsed between consecutive bubble eruptions in the proximity of the focal point.

Figure III.21 demonstrates the effect of localized bubble formation at the focal point due to supplemental gas fed via the BGS. The figure reports sequences of thermal maps of the bed surface recorded in tests carried out with bubble injection, for two values of the nozzle–surface gap: 0.03 m and 0.09 m. The gas superficial velocity was  $0.013 \text{ m s}^{-1}$  and the bubble release frequency was set at 0.2 Hz, conditions that made it possible to follow the phenomenology associated with the eruption of a single bubble. The frame at 0 ms corresponds to the time just before the establishment of the “dome”, that is when the nose of the bubble starts to emerge from the bed surface. In Figure III.21-up, corresponding to a nozzle–surface gap of 0.09 m, the first snapshot (0 ms) shows a warmer annular region around the focal point remaining after the previous eruption. Eventually, the displacement of the hot fluidized particles from the nose of the erupting bubbles toward an annular region whose mean diameter is about 0.12 m, roughly twice the bubble diameter, was observed. The sequence clearly demonstrates that localized bubble eruption at or close to the focal point effectively promotes lateral dispersion of incident power by solids convection. Applying the Einstein’s equation (*Einstein, 1956; Liu and Chen, 2010; Farzaneh et al., 2013*):

$$D = \frac{(\Delta x)^2}{2\Delta t} \quad (\text{III.6})$$

and estimating the displacement ( $\Delta x$ ) and the time duration of displacement ( $\Delta t$ ) of the hot particles during the eruption of 0.065 m diameter single bubbles, observed from infrared time-resolved maps, a coefficient of lateral dispersion was calculated in the order of  $D=3\text{--}4\times 10^{-3} \text{ m}^2 \text{ s}^{-1}$ . When the gap between the nozzle tip and the bed surface is reduced to 0.03 m, the phenomenology somewhat changes (Figure III.21-down). Ejection of particles due to bubble bursting takes place as an intermittent spout. Some of the hot particles located at the focal point are ejected away, but most of them are submerged by the colder particles avalanching from the region surrounding the spout or coming from the underneath bulk of the fluidized bed. Consequently, the distribution of warmer particles across the surface is more irregular when compared with results obtained with the larger gap. It is likely that this hydrodynamical pattern could be more favourable to axial dispersion of the incident radiative power.

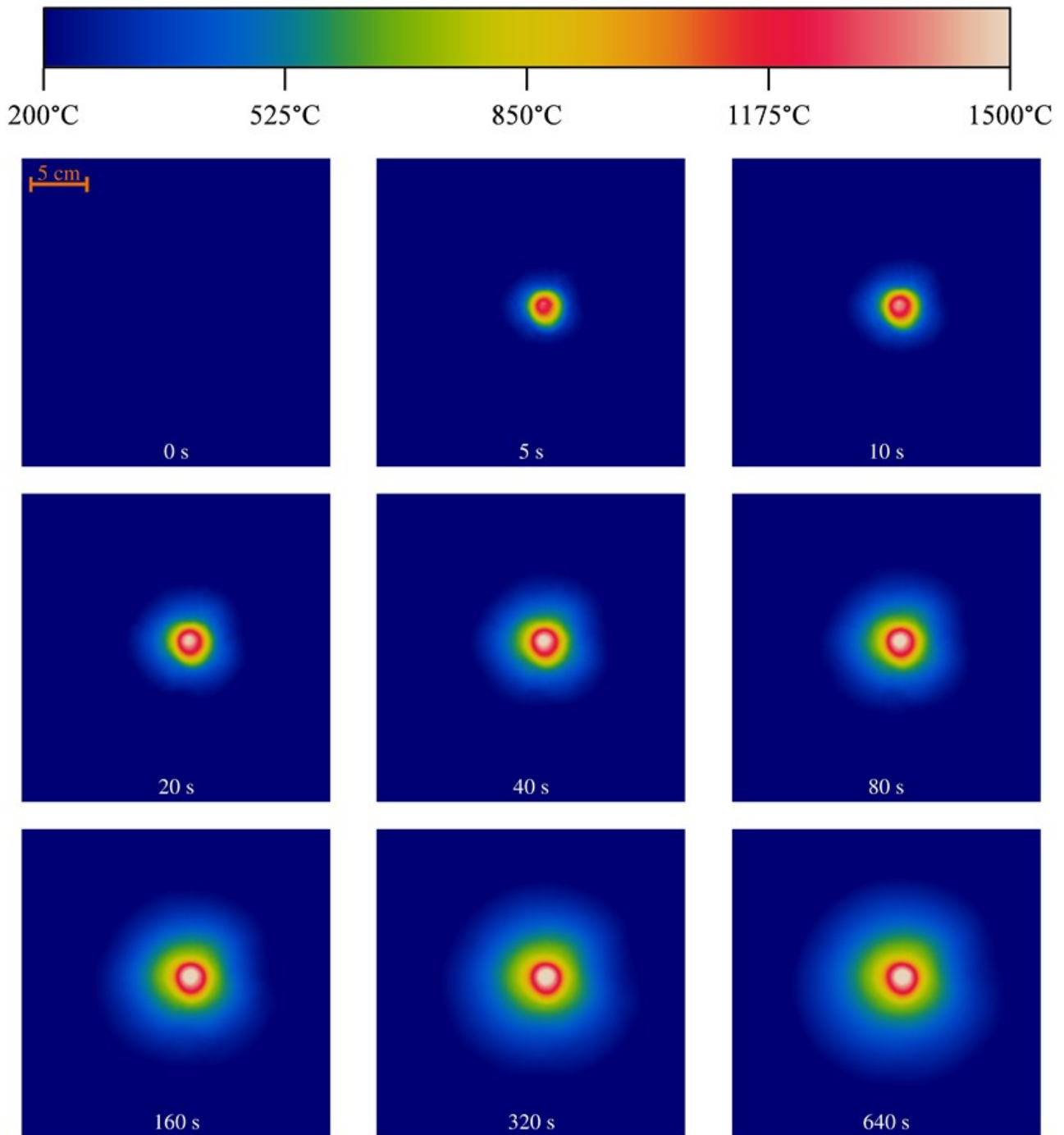


**Figure III.17:** Sequence of thermal maps of the bed surface under fixed bed conditions (no inlet gas).

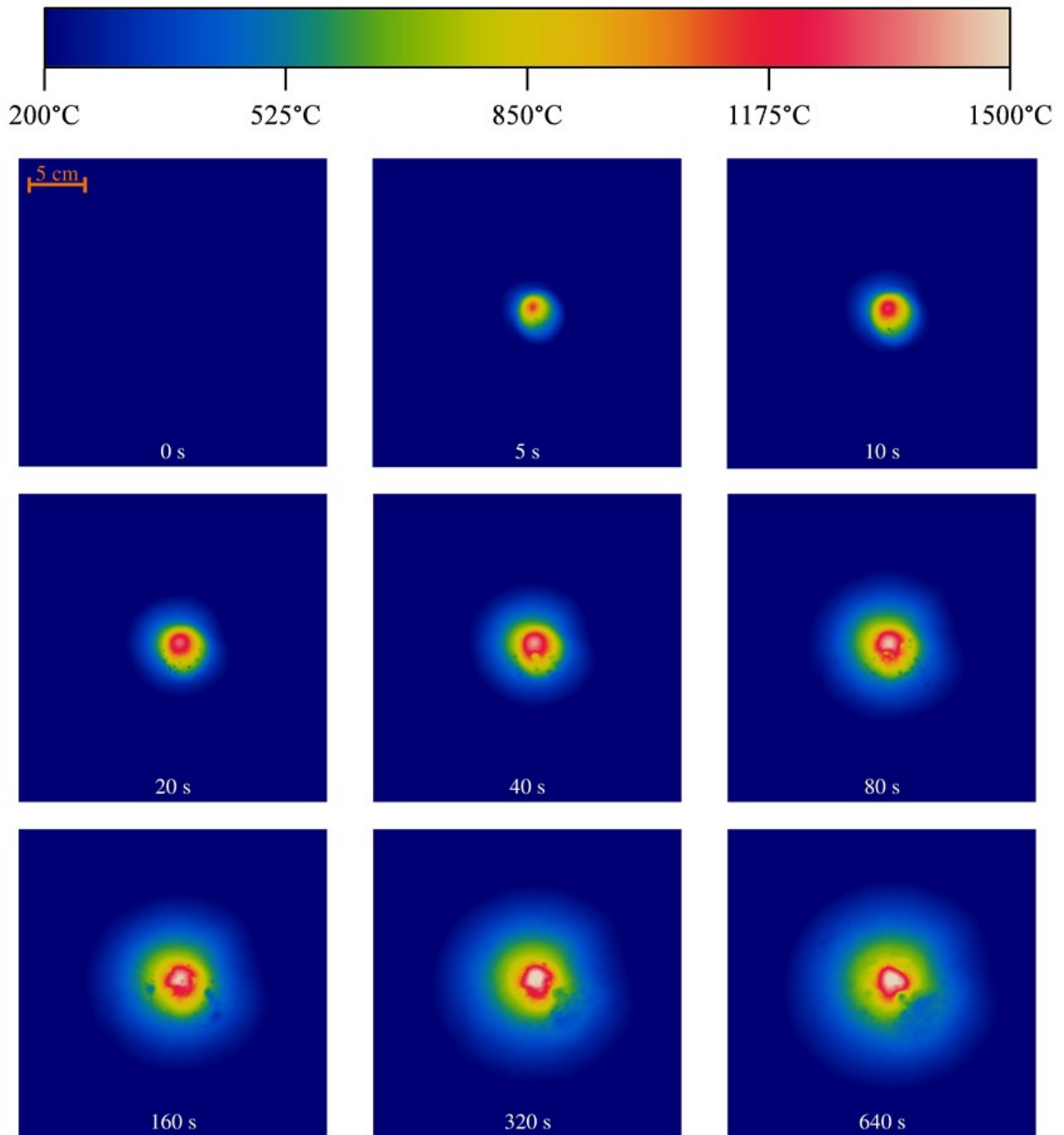


**Figure III.18:** Sequence of thermal maps of the bed surface under incipient fluidization conditions ( $U=0.018 \text{ m s}^{-1}$ ).

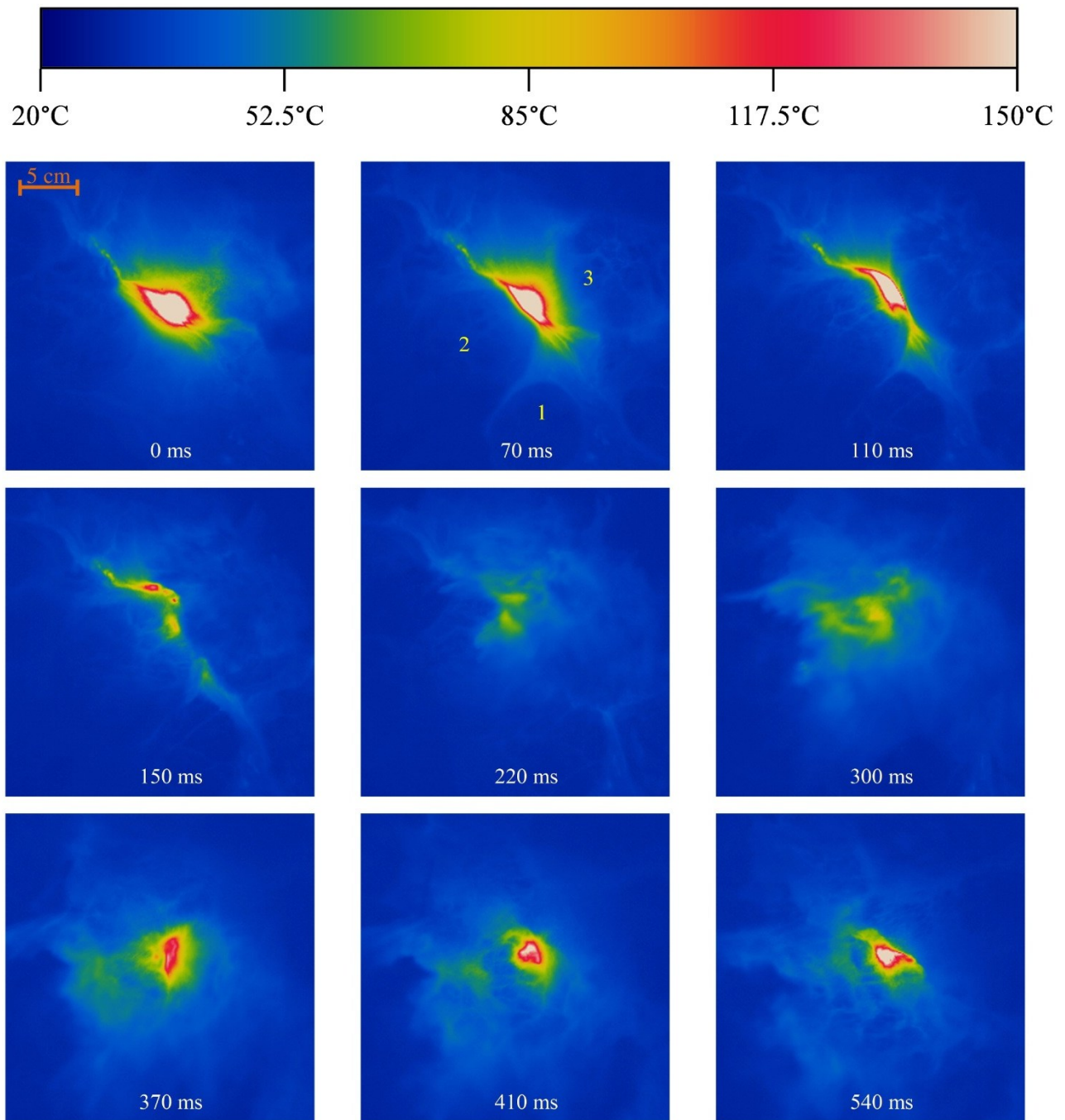


**Figure III.19:** Sequence of thermal maps of the bed surface under freely bubbling conditions ( $U=0.073 \text{ m s}^{-1}$ ). Numbers 1, 2 and 3 mark the location where bubble bursting causes extensive particles displacement by “avalanching”.

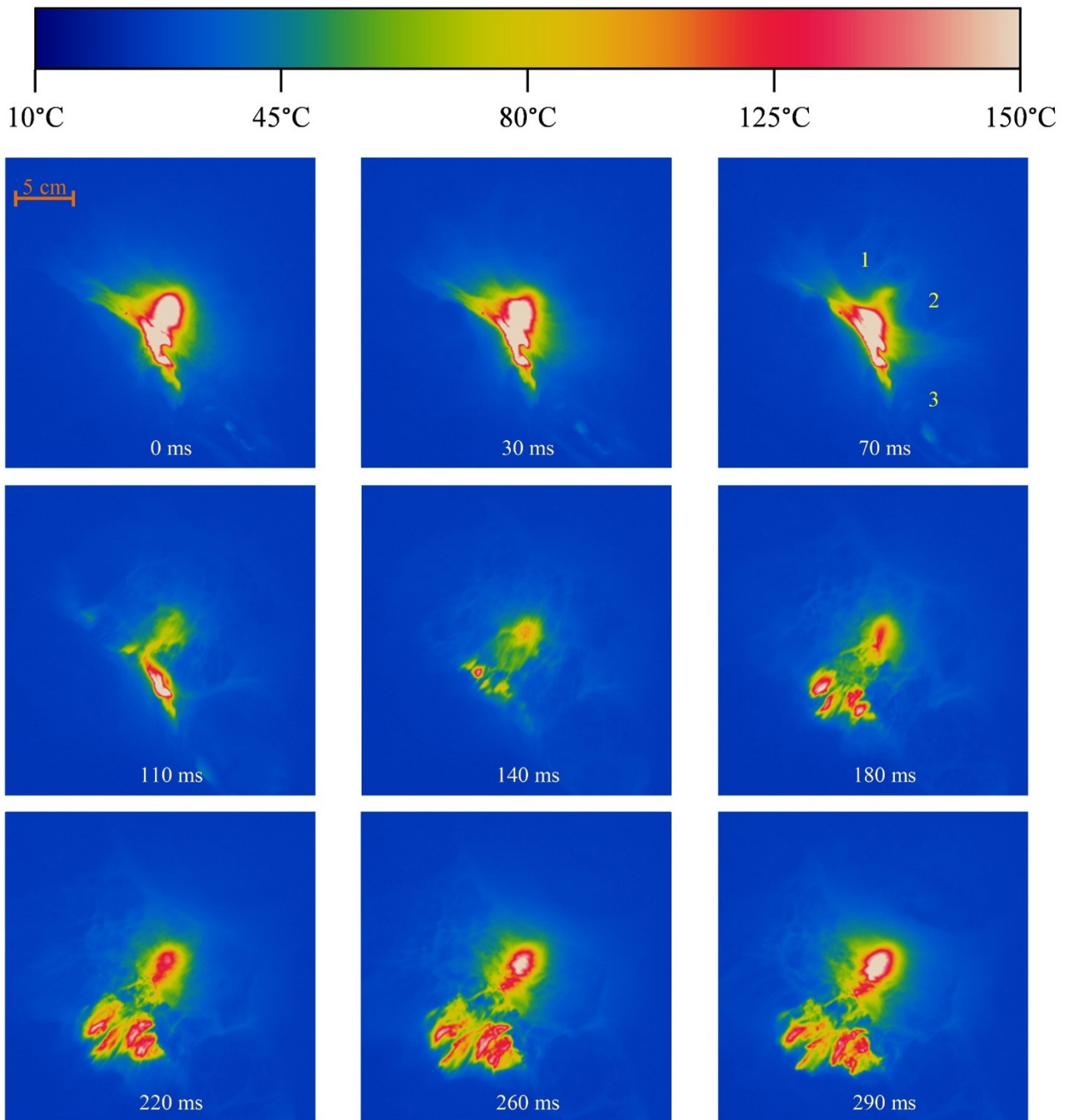


**Figure III.20:** Sequence of thermal maps of the bed surface under freely bubbling conditions ( $U=0.073 \text{ m s}^{-1}$ ). Numbers 1, 2 and 3 mark the location where bubble bursting causes extensive particles displacement by ejection and fall-out of particles.

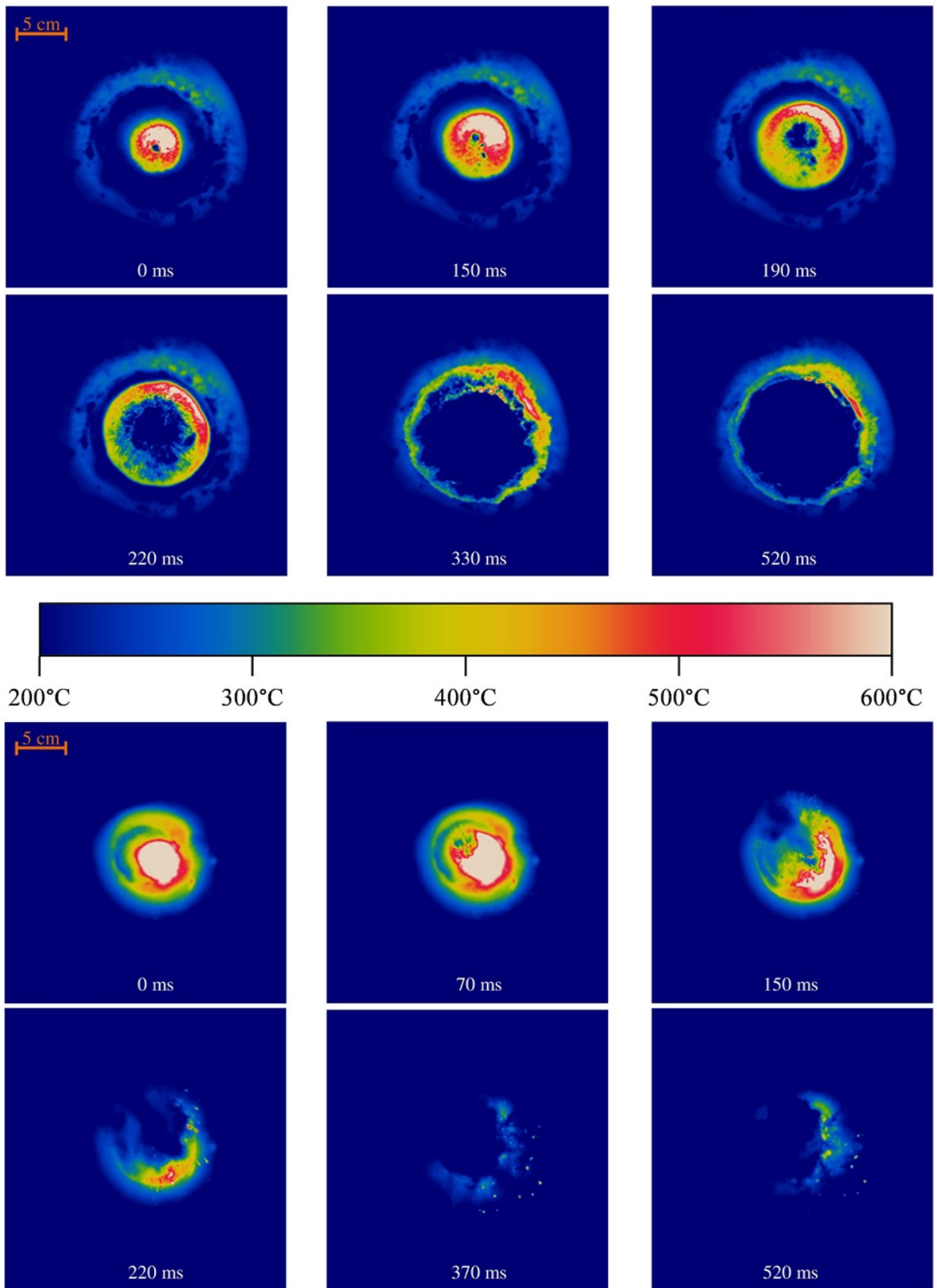


**Figure III.21:** Sequence of thermal maps of the bed surface in a test with injection of bubbles through the BGS nozzle ( $U=0.013 \text{ m s}^{-1}$ ). Nozzle–surface gap: 0.09 m (up); 0.03 m (down).

### **III.5.2 Analysis of the Temperature Time-Series at the Focal Point**

Figure III.22 reports time-resolved temperatures recorded at the focal point just after the radiation source was turned on. Profiles obtained at different values of the gas superficial velocity in fixed and fluidized beds without injection of additional bubbles are compared. When multiple calibration ranges of the infrared camera had to be used, the time-series obtained with each calibration range are reported as separate plots. Under fixed bed conditions, the 200–1500 °C calibration range of the infrared camera was used. The temperature steeply increases to  $T > 1200$  °C in less than 5 s, and eventually more gradually to the maximum detectable temperature of 1525 °C after about 90 s.—When freely bubbling conditions were established, temperature fluctuations became evident once the source was turned on. At gas superficial velocities just beyond incipient fluidization, the temperature was above 400 °C for most of the time, and measurements with the 200–1500 °C calibration range were sufficient to fully characterize the dynamics of the irradiated bed. As the gas superficial velocity was increased, temperature fluctuations became more pronounced, and tests with both the 0–250 °C and 150–900 °C and 200–1500 °C calibration ranges had to be carried out and complemented to each other to get an accurate picture of the dynamics of the bed.

Figure III.23 reports the time-resolved temperature profile at the focal point for different gas superficial velocities recorded in experiments in which additional bubbles were injected through the BGS. Results corresponding to two nozzle–surface gaps (0.03 m and 0.09 m) are compared. Time-series of bed temperature are reported over a relatively short time interval (5 s) to better disclose the details of temperature fluctuations associated with the bursting of individual bubbles. Results correspond to three operating conditions: fixed bed ( $U < U_{mf}$ ), incipiently fluidized bed ( $U_{mf} \cong U = 0.022$  m s<sup>-1</sup>), freely bubbling fluidized bed ( $U_{mf} < U = 0.063$  m s<sup>-1</sup>). Analysis of the time-series in Figure III.23 suggests that under fixed or incipiently fluidized bed conditions the temperature increases before bubble bursting and abruptly falls down when the bubbles erupt. The regular cyclic character of temperature rise/drop observed in fixed/incipiently fluidized beds is smoothed out when the bed is freely bubbling, due to interaction of multiple erupting bubbles. Comparison of results reported in Figures III.22 and III.23 demonstrates the pronounced effect of additional bubbles injected close to the focal point on the time-averaged temperature and extent of temperature fluctuations. Bubble bursting at the point of maximum radiative flux provides fast and continuous convective heat transfer through the displacement of hot fluidized particles.

Useful fingerprints of the dynamics of irradiated fluidized beds are provided by the probability density functions of bed surface temperature reported in Figures III.24 and III.25 for different gas superficial velocities. Figure III.24 refers to beds operated without injection of additional bubbles, and show that the  $P(T)$  functions are broad with fairly high peak temperatures when the bed is incipiently fluidized. Both the peak temperature and the variance of the distribution decrease as the gas superficial velocity is increased, occasionally displaying a bimodal character. Figure III.25 refers to experiments carried out with injection of additional bubbles and compares results obtained with nozzle–surface gaps of 0.09 m (up) and 0.03 m (down). Plots refer to fixed, incipiently fluidized and freely bubbling bed conditions. The general features of the  $P(T)$  plots are similar to those observed without bubble injection, with a clear indication that bubble injection suppresses the high-temperature peak when the bed is operated at gas superficial velocities smaller than or close to incipient fluidization velocity.

Figure III.26A summarizes the key findings of the experimental campaign. The time-averaged bed surface temperature at the focal point is reported as a function of the gas superficial velocity for all the experimental conditions tested. Plots also report the temperature standard deviation, represented as error bars, which is entirely due to temperature fluctuations since the contribution associated with reproducibility of data and inherent measurement error is negligible. The analysis of Figure III.26A suggests that the fluidized state of the bed improves lateral dispersion of incident radiative power: the larger the gas superficial velocity, the better the dispersion. Localized injection of gas bubbles close to the focal point yields noticeable effects on dispersion of the incident radiative power and temperature equalization. An even limited addition of fluidizing gas close to the focal point brings about a dramatic reduction of local overheating and improvement of heat transfer.

Altogether, results suggest that interaction of incident radiative power and the bed involves only a few layers of particles under fixed or incipiently fluidized bed conditions, as also suggested by previous studies (*Flamant, 1982*). When moderate fluidization is established, the concentrated incident radiative flux is dispersed inside the bed, mostly by lateral dispersion at the bed surface. At even larger gas superficial velocities, ejection of bed solids above the bed surface (in the splash region) contributes to the establishment of a collection mechanism of radiative flux approaching that of volumetric receivers. Moreover, the onset of large-scale bed solid circulation enhances convective transfer of the incident power to the bulk of the bed. Under these conditions a much larger volume of bed solids is involved in radiative power collection and transfer, and this reduces the time-averaged temperature and the extent of temperature fluctuations, with beneficial effects on collection efficiency and operability of the receiver. The effect of localized bubble injection close to the focal point emphasizes the importance of proper tailoring of the hydrodynamics of the bed to improve the collection performance of the solar receiver coupled with a proper thermal and/or thermochemical energy storage system. Results obtained in the present study demonstrate that a dramatic improvement of collection performance may be achieved by uneven fluidization along fluidized bed cross section (*Salatino et al., 2016*), i.e. establishing vigorous fluidization only within the section of the bed where solar radiation is mostly concentrated, while leaving the rest of the bed, acting as thermal and/or thermochemical energy storage system, under moderate fluidization conditions. This choice may represent an optimal trade off between conflicting requirements: a) improving convective heat transfer of incident radiative power to the bulk of the fluidized bed; b) reducing parasitic energy losses associated with sensible heat of the fluidizing gas and fan power required to establish the fluidized state of the bed.

### **III.5.3 A Compartmental Model of In-Bed Dispersion of Radiative Flux**

The interaction between the incoming radiative beam and the fluidized bed, with specific reference to the mechanism governing the dispersion of the radiative power to the bulk of the bed, has been further elucidated by a simple compartmental heat transfer model. The bed is partitioned into a “collection” zone and a “bulk” zone. The absorbed fraction of the energy flux impinging the collection zone is balanced by: a) heat losses due to thermal radiation to the environment, b) heat losses associated with convective flux of the fluidizing gas flowing across the collection zone, and c) convective heat flux due to bed solids circulation between the collection zone and the bulk zone. The latter is proportional to the circulation velocity of bed solids at bed surface which, in turn, is expressed as the product of a non-dimensional solids circulation parameter  $\beta$  and the gas superficial

velocity in excess with respect to the incipient fluidization velocity ( $U - U_{mf}$ ). The energy balance on the collection zone therefore reads:

$$\alpha q = \varepsilon \sigma T_s^4 + \rho U \bar{c}_p (T_s - T_{bed}) + \beta \rho_s (1 - \varepsilon_{mf}) (U - U_{mf}) \bar{c}_{ps} (T_s - T_{bed}) \quad (\text{III.7})$$

where:

$\alpha$  and  $\varepsilon$  are the fluidized bed absorptivity and emissivity, respectively (equals under the assumption of grey-body behaviour);

$q$  is the impinging radiative flux;

$\sigma$  is the Stefan–Boltzmann constant;

$T_s$  and  $T_{bed}$  are the temperatures of the collection and bulk zones, respectively;

$\rho$  and  $\rho_s$  are the gas density (at  $T_{bed}$ ) and bed solids density, respectively;

$\bar{c}_p$  and  $\bar{c}_{ps}$  are the gas and bed solids specific heat, respectively, averaged over the temperature range  $[T_{bed}, T_s]$ .

Equation (III.7) has been used to estimate the best fit value of the solids circulation parameter  $\beta$  by matching the computed vs. measured values of  $T_s$  at different values of the gas superficial velocity  $U$  (Figure III.26A). The calculated values of  $\beta$  increase with  $U$ , spanning from 0.042, close to incipient fluidization, to 0.12 when the bed is vigorously bubbling. Figure III.26A reports the  $T_s$  vs.  $U - U_{mf}$  curve calculated from Eq. (III.7) by taking  $\beta=0.071$  as an average over the range of  $U$  investigated. The estimated value of  $\beta$  is in fairly good agreement with the value (0.1) assumed by *Pemberton and Davidson* (1986a) to model the bed solids mass flux ejected by erupting bubbles at the bed surface in freely bubbling beds. The agreement of the solids circulation parameter  $\beta$  with values reported in previous and independent studies, and the general ability of Eq. (III.7) to reproduce the  $T_s$  vs.  $U - U_{mf}$  basic patterns reported in Figure III.26A, support the soundness of the chosen compartmental model. This model can be used for quantitative estimates of the ability of the bed to disperse the impinging flux and equalize the temperature throughout the bed. Equation (III.7) can be also applied in the case of bubble localized injection provided that the effective local fluidization velocity is taken into account. The agreement between the model and experimental data adopting the same value of  $\beta$  is good as evident from Figure III.26A.

The compartmental model may be conveniently used to estimate the solar capture efficiency ( $\eta$ ) of the fluidized bed. This is defined as the ratio between the heat flux transferred from the collection zone to the bulk zone and the maximum heat flux which would be absorbed by the bed if the same were at uniform temperature  $T_{bed}$ :

$$\eta = \frac{\beta \rho_s (1 - \varepsilon_{mf}) (U - U_{mf}) \bar{c}_{ps} (T_s - T_{bed})}{\varepsilon (q - \sigma T_{bed}^4)} \quad (\text{III.8})$$

Values of  $\eta$  computed according to Eq. (III.8) are reported in Figure III.26B as a function of the gas superficial velocity  $U$  and for different values of temperature  $T_{bed}$ . As expected, the solar capture efficiency sharply increases as the fluidization velocity departs from the incipient fluidization velocity, as a consequence of the effective dispersion of the radiative power to the bulk of the bed due to solids circulation. The capture efficiency levels off at larger values of  $U$ , and decreases with the temperature  $T_{bed}$  at pre-set values of  $U - U_{mf}$ .

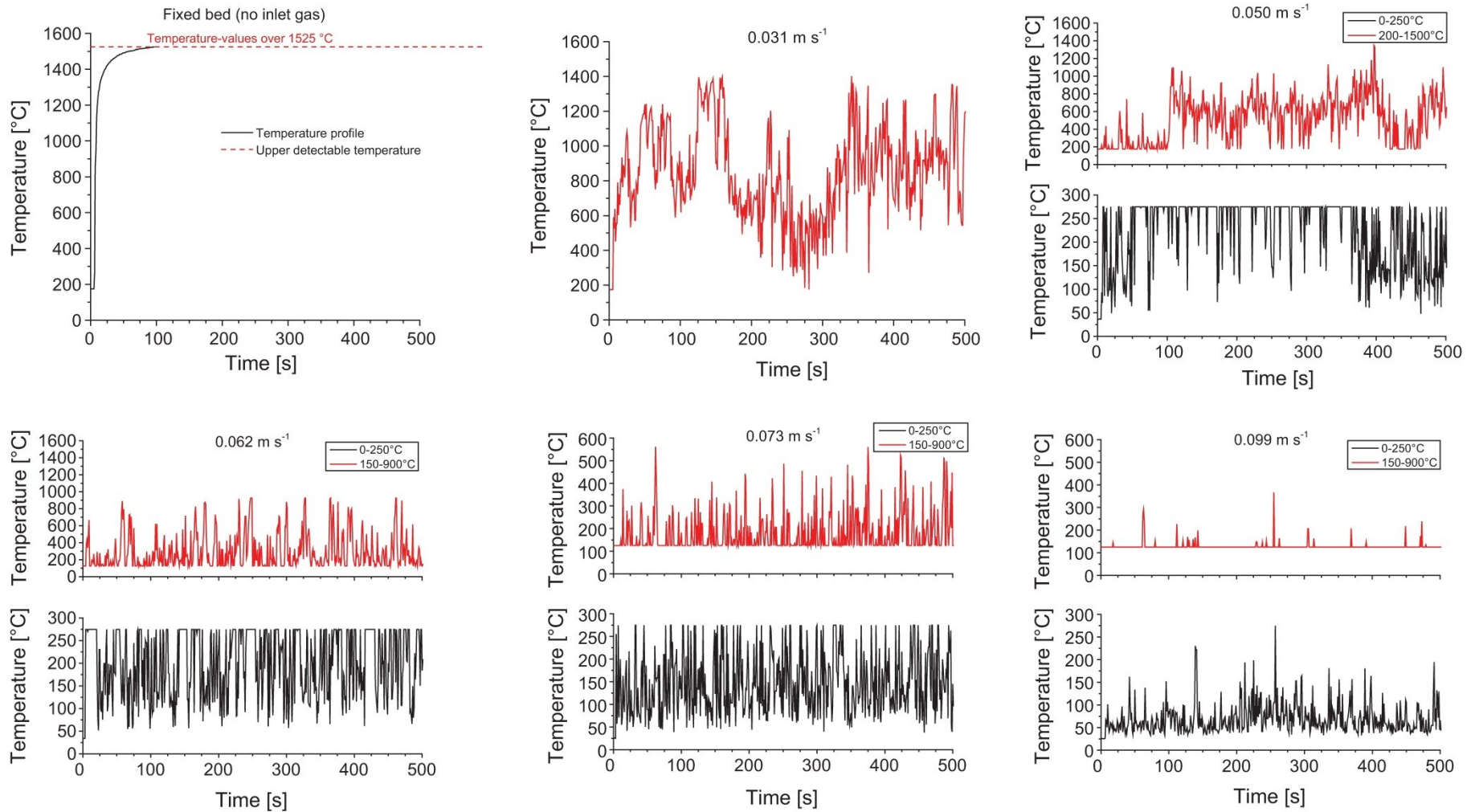


**Figure III.22:** Time-resolved bed surface temperature profiles in tests performed at different gas superficial velocities. Signals obtained in tests with different infrared camera calibration ranges are reported as separate plots.

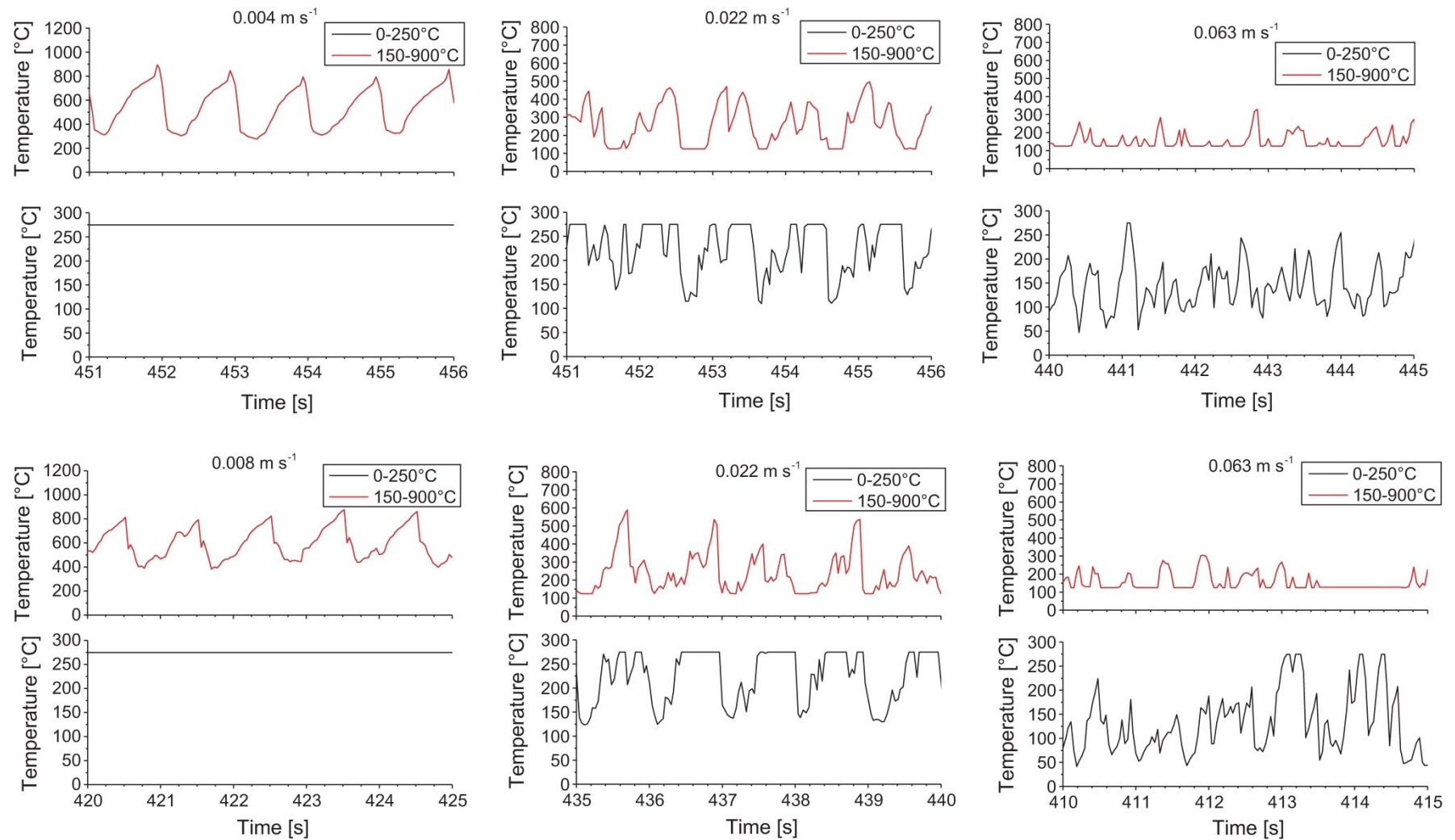


**Figure III.23:** Time-resolved bed surface temperature profiles in tests performed at different gas superficial velocities (left: fixed bed; centre: incipiently fluidized bed; right: freely bubbling bed) with injection of bubbles through the BGS. Nozzle-surface gap: 0.09 m (up); 0.03 m (down). Signals obtained in tests with different infrared camera calibration ranges are reported as separate plots.

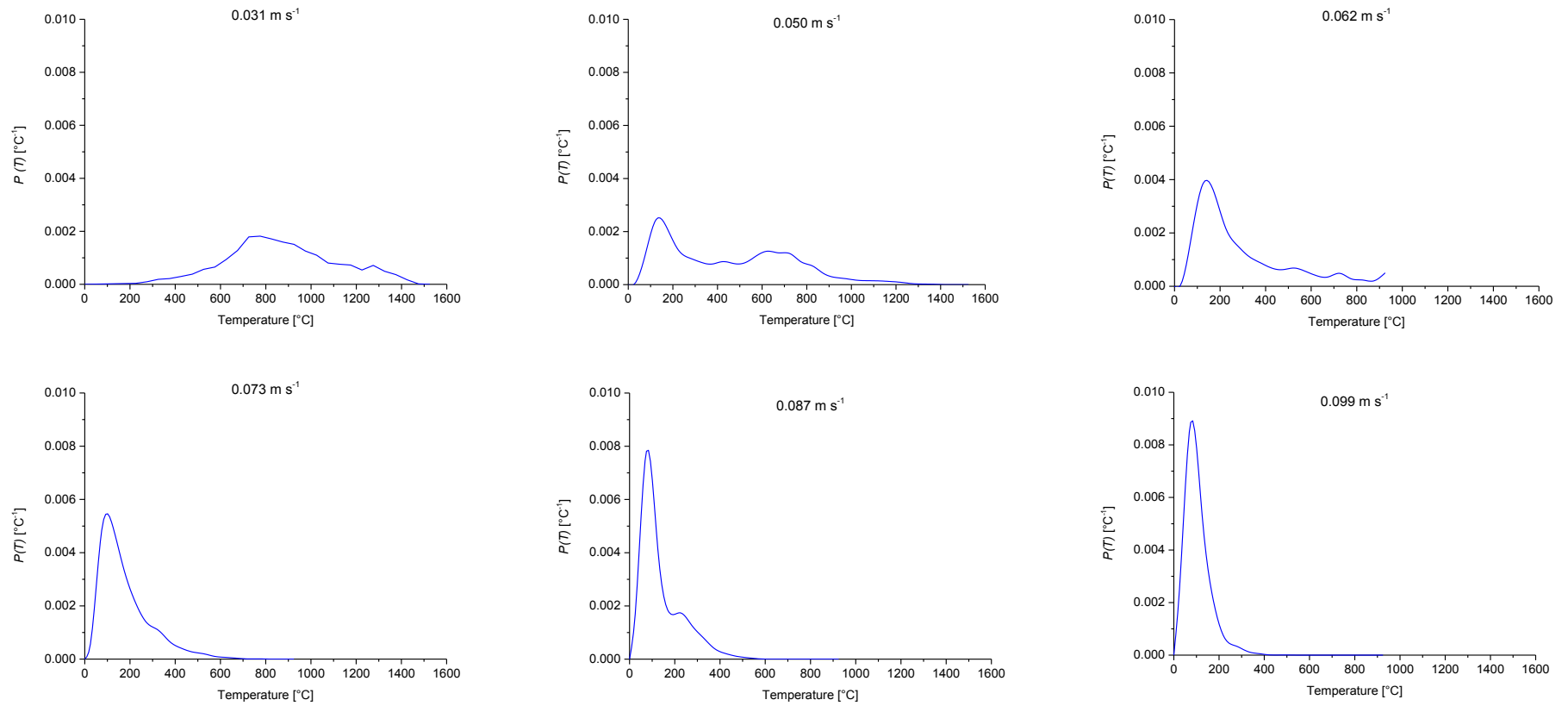


**Figure III.24:** Probability density functions of the time-series of bed surface temperature obtained in experiments at different gas superficial velocities without injection of bubbles.

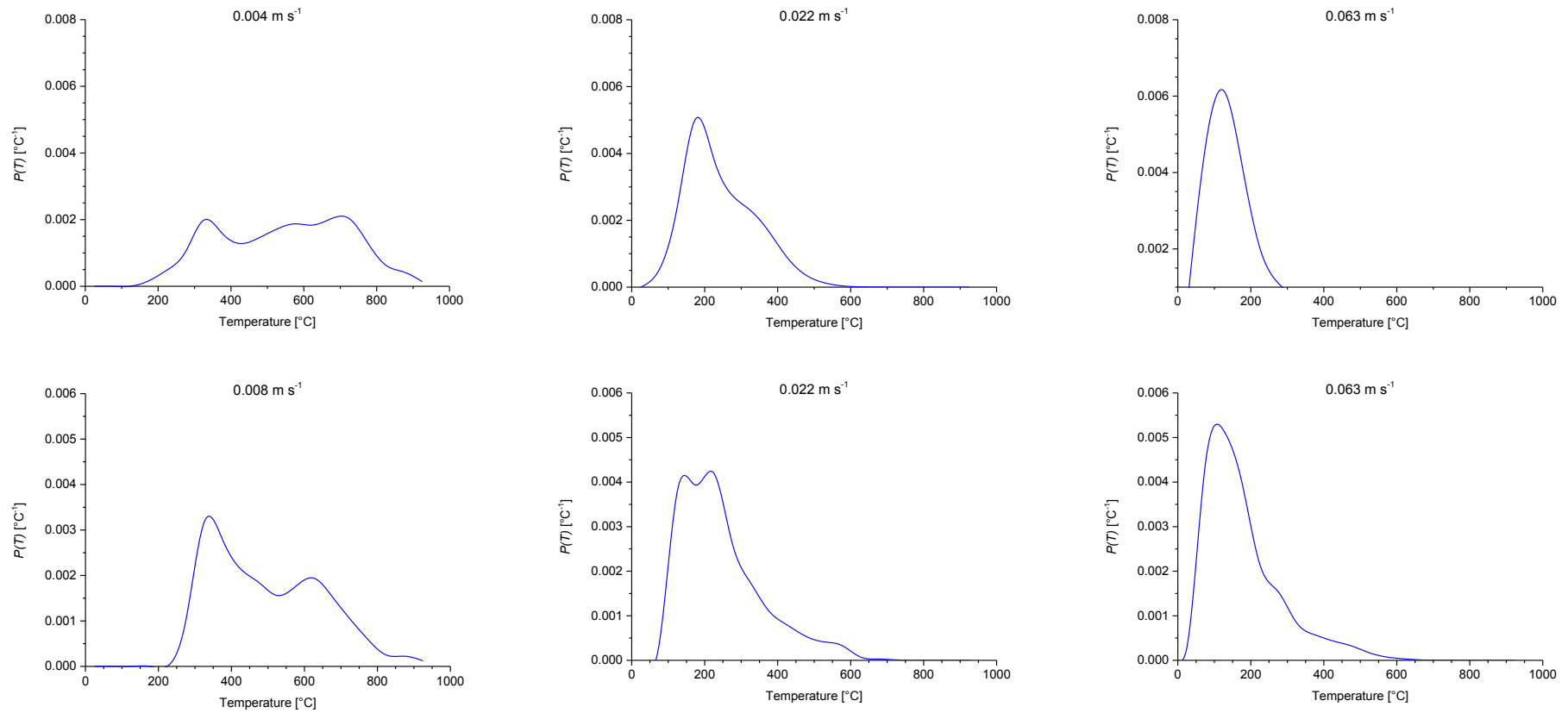


**Figure III.25:** Probability density functions of the time-series of bed surface temperature obtained in experiments at different gas superficial velocities (left: fixed bed; centre: incipiently fluidized bed; right: freely bubbling bed) with injection of bubbles through the BGS. Nozzle–surface gap: 0.09 m (up); 0.03 m (down).

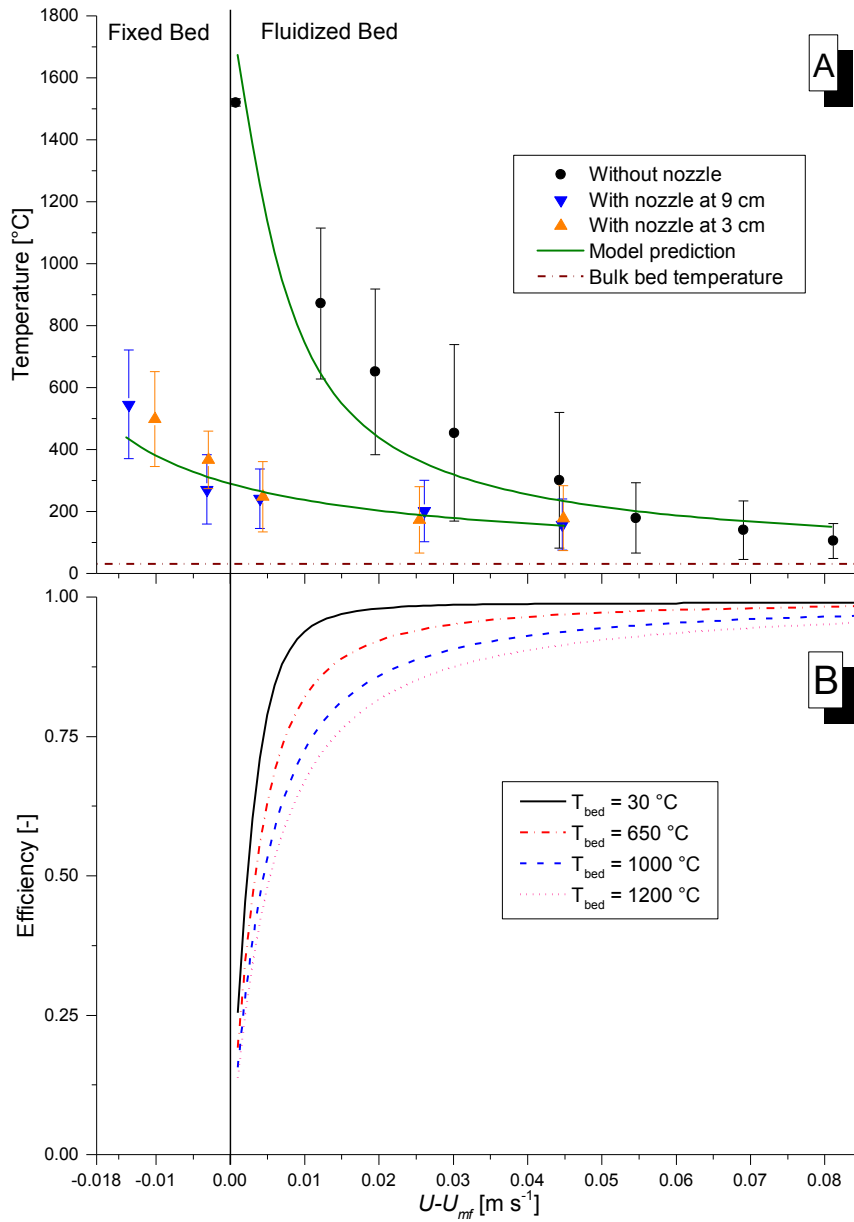


**Figure III.26:** A) Time-averaged bed surface temperature as a function of the excess of superficial gas velocity with respect to the minimum fluidization condition for all the operating conditions tested. Standard deviations are reported as error bars; B) radiative power collection efficiency according to Eq. (III.8) as a function of the excess of superficial gas velocity with respect to the minimum fluidization condition for different values of bed temperature  $T_{bed}$ .

### III.6 Final Remarks

Direct interaction between concentrated incident solar radiation and a fluidized bed has been experimentally investigated by time-resolved mapping of bed surface temperature with an infrared camera. Solar radiative flux was simulated by a 4 kW<sub>el</sub> short-arc Xe lamp coupled with an elliptical reflector. The mechanisms underlying heat transfer to the bed surface and further dispersion of heat to the bulk of the bed have been scrutinized under fixed and fluidized bed conditions by varying the gas superficial velocity. Moreover, the effect of localized injection of gas bubbles through a nozzle located in the proximity of the focal point has been assessed.

Experimental results suggest that collection of incident radiation changes from a surface-receiver to a volumetric-receiver paradigm as the gas superficial velocity is increased from fixed to incipiently fluidized bed conditions and even further to freely bubbling fluidization. Moreover, fluidization promotes lateral and axial dispersion of solids, hence efficient convective heat transfer from the focal point of the incident radiative flux to the bulk of the bed. This is reflected by a significant reduction of peak temperature and temperature fluctuations at the focal point of the receiver that positively affect the collection efficiency of the receiver and reduce the thermomechanical stresses suffered by process materials. Experimental results are used to validate a compartmental heat transfer model which provides a simple, though accurate, equation for predicting in-bed dispersion of radiative power and extent of temperature non-uniformity.

The favourable thermal behaviour of fluidized beds can be further improved by proper tailoring of the hydrodynamics of the bed in the proximity of the focal point, e.g. by additional/localized feeding of fluidizing gas and generation of bubbles. This is the path to follow to achieve a good compromise between the very favourable thermal properties of fluidized beds and the need to reduce parasitic energy losses associated with the establishment of the fluidized state.

# Chapter IV. Design of a Fluidized Bed Solar Reactor and Application to Calcium Looping Process

## IV.1 Introduction

In the present Chapter, the results obtained from the Xe-lamp characterization, together with the analysis of the direct interaction between a concentrated solar radiation and the surface of a fluidized bed, are used to design a directly irradiated solar fluidized bed reactor suitable for high temperature operations. The attention is focused on the investigation of thermochemical heat storage processes, with special reference to the calcination and carbonation reactions of a calcium-based sorbent to be employed in calcium looping applications. Several calcination-carbonation reactions are performed on a Ca-based sorbent in order to evaluate the CO<sub>2</sub> capture capacity of the limestone material and its trend over repeated cycles.

## IV.2 Basic Design of the Solar Reactor

Several aspects were taken into account, including geometrical and energetic considerations, in order to correctly design the solar fluidized bed reactor.

### IV.2.1 Geometrical Features

A first important aspect was the choice of the fluidized bed dimensions, more specifically of its inner bed diameter ( $D_{bed}$ ) and bed height ( $H_{bed}$ ). Concerning the internal bed diameter, two main issues were considered: i) small  $D_{bed}$  could result in a hydrodynamic behaviour of the fluidized bed strongly influenced by wall-effects, with the possible establishment of the undesired slugging regime, and ii) large  $D_{bed}$  would require significantly high input thermal power. The trade-off of these two issues resulted in setting  $D_{bed}$  equal to 4 inch (0.102 m).

The bed height was instead chosen equal to approximately 0.1 m, so as to obtain an aspect ratio for the reactor close to the unity. This was made in order to have the establishment of a single vortex ring involving the whole emulsion phase whatever the fluidization velocity: downward and upward vortex ring at low and high fluidizing gas velocity, respectively. Different configurations, such as deep or shallow beds, are characterized by multiple vortex rings which make more complex the control of motion of emulsion phase in the fluidized bed reactor.

Special attention was paid on the design of the freeboard section of the fluidized bed reactor, as the window required for the access of the solar simulated radiation is located at the extremity of this section. This section was then designed so as to accommodate the entry of the concentrated solar radiation and protect the upper window from particle impingement. In order to fulfill the former task, it is required that the freeboard section be characterized by a conical shape, whose internal cone angle is dependent on the geometry, the number and the arrangement of the elliptical reflectors. The considered reflectors were the ones described in § III.2.2, featuring a distance between the two conjugated foci of 1.585 m. Moreover, it was assumed a configuration which involves the use of a central elliptical reflector and up to four surrounding reflectors arranged in a cross around the central one. In a similar configuration, the four surrounding reflectors would be all tilted of the same angle but toward opposite directions. This configuration has also the potential of

adding four further reflectors arranged in a cross shifted by a  $45^\circ$  angle with respect to the previous one. Then, the total number of allowed Xe-lamps ranges from one to nine. By referring to the just described configuration, it was chosen an internal cone angle of  $32^\circ$ . It was also verified that this angle resulted smaller than the repose angle of the granular materials that will be used in the reactor (e.g., silica sand, silicon carbide) to avoid solids accumulation on the cone wall. Besides the internal cone-angle, it was also crucial the establishment of an appropriate height for the conical section to effectively protect the upper window, and to provide an outlet path for the gas avoiding the entrainment of the coarser solid particles ejected by bubble bursting. According to *Pemberton and Davidson* (1986b), the height reached by coarse particles due to bubble bursting is approximately equal to the diameter of the erupting bubble. By applying this concept to the designed reactor, the eruption of a bubble with a maximum diameter of 10 cm could eject the particles up to 10 cm height: it was then decided to place the gas outlet at a safety distance of 20 cm from the bed surface. However, fine particles can follow the gas flow lines and vortex structures may form in the upper zone: for these reason, the upper window was placed at a 20 cm further distance from the gas outlet. It is worth to note that the conical shape of the upper section also plays a beneficial role in the protection of the upper window thanks to the strong decrease of the gas velocity due to the cross section increase. Briefly summarizing, the upper conical section is, on the whole, 40 cm high and the gas output is located at half freeboard height.

#### **IV.2.2 Process Operating Conditions**

Reference data for the process parameters required to carry out the calcination and carbonation reactions of Ca-based sorbent in fluidized bed reactors were taken from the literature (*Coppola et al.*, 2013). In agreement with the previously developed CaL process scheme (see Figure II.1), only the endothermic calcination step will be carried out with the use of the solar simulated radiation, while the carbonation step will be performed with the use of conventional electrical heating sources. The designed solar reactor will then be equipped with both a solar simulator and electrical heating sources such as electric ovens or gas preheater, which could also be useful during the initial start-up period. In order to evaluate the heating demand of the solar reactor, the calcination reaction will be considered over the carbonation as the former it is the endothermic high temperature step of the CaL process, and thus the more power demanding stage. The experimental tests were conceived to be performed with relatively small amounts of  $\text{CaCO}_3$ -based limestone (10–15%<sub>w</sub>t) diluted in a silica sand bed, so as to avoid the occurrence of strong thermal changes during the course of the reactions. Concerning the limestone, a particle size range of 400–600  $\mu\text{m}$  was considered as a trade-off between the exigency of maximizing the heat and mass transfer coefficients –enhanced by a fine particle diameters–and limiting the attrition/elutriation phenomena, enhanced by fine particle diameters too (*Montagnaro et al.*, 2002). On the other hand, concerning the silica sand powder, particles in the range size 850–1000  $\mu\text{m}$  size range were considered. The fluidizing gas velocity ( $u_{gas}$ ) was set at  $0.6 \text{ m s}^{-1}$ , which is roughly twice the minimum fluidization value of the silica sand at  $950^\circ\text{C}$ . Lastly, the bulk bed temperature ( $T_{bed}$ ) was set at  $950^\circ\text{C}$ .

#### **IV.2.3 Fluidized Bed Surface Over-Temperature**

The efficiency of the solar receiver was preliminarily evaluated in order to correctly estimate the energy required to fulfil the calcination reaction through the solar simulator. To this end it was

of fundamental importance to consider the over-temperature of the fluidized bed surface. The acquired knowledge concerning the direct interaction between a concentrated solar radiation and the surface of a fluidized bed (see Chapter III) suggests indeed that a higher bed surface temperature should be expected with respect to the bulk bed value as a result of the highly concentrated radiation impinging on the bed surface. The over-temperature was estimated by applying the compartmented model of in-bed dispersion previously developed (see § III.5.3). The operating parameters described in the previous paragraph were considered, while for the solid bed material a silica sand powder with mean particle diameter of  $925\ \mu\text{m}$  was taken as reference. Air was considered as fluidizing gas. Emissivity and absorptivity coefficients were both set equal to 0.9, while an impinging flux equal to  $3000\ \text{kW m}^{-2}$ , roughly three times the one for a single Xe-lamp, was assumed (assumption ex post justified). Results of the model computations are reported as a function of the solid recirculation parameter in Figure IV.1. For  $\beta=0.07$  (the value estimated for the SiC powder in Chapter III) the over-temperature approaches a value of nearly  $120\ ^\circ\text{C}$ . However, as the silica sand powder taken as reference is considerably coarser than the SiC powder, it is reasonable to imagine that the solid recirculation parameter could be lower. As  $\beta$  decreases, the over-temperature steeply increases: values of  $138$  and  $164\ ^\circ\text{C}$  are obtained for  $\beta$  of  $0.06$  and  $0.05$ , respectively.

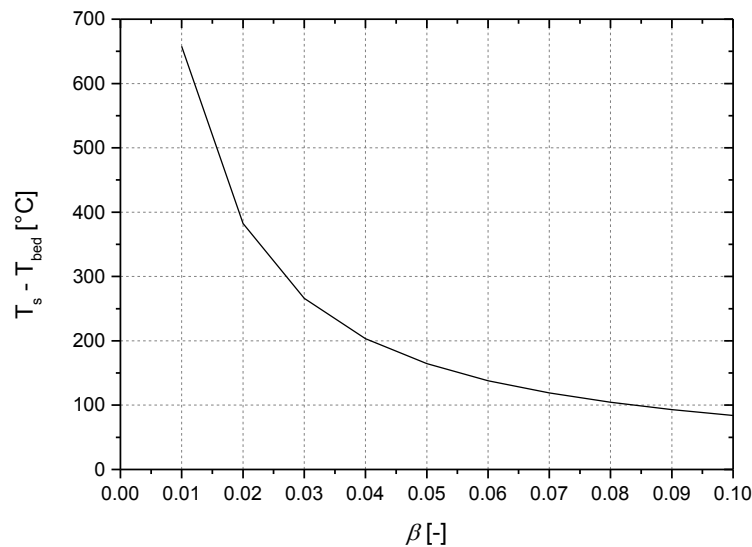


**Figure IV.1:** Over-temperature of the fluidized bed surface vs. the solid recirculation parameter.

For the solar reactor design it was then considered an over-temperature value of  $150\ ^\circ\text{C}$ , which reflects a  $\beta$ -value between  $0.06$  and  $0.05$ . The bed surface temperature ( $T_s$ ) is then expected to approach a temperature as high as  $1100\ ^\circ\text{C}$ .

With the aim of reducing the surface over-temperature, a central nozzle which passes through the distributor plate and stops at half the solid bed height has also been designed to tailor the hydrodynamics of the bed surface through a localized bubble generation.

#### ***IV.2.4 Energy Balance***

An energy balance under steady-state conditions was then performed to estimate the number and the power of Xe-lamps required to provide the reactor with a sufficient amount of heat. The

data reported in the previous paragraphs were used, while the following main assumptions were considered:

- i) The reactor is radially isotherm, while an axial gradient exists. Two temperature values are considered to take into account the axial distribution: a bulk value and a surface value;
- ii) Heat losses toward the surrounding environment due to conduction through the reactor wall are neglected;
- iii) The outlet gas is isotherm with the bulk reactor temperature;
- iv) Air is considered as the fluidizing gas;
- v) The heat of the calcination reaction is neglected (assumption ex post justified).

Under the stated hypothesis, the energy balance equation reads:

$$\alpha \overline{Q}_{IN} - \varepsilon \sigma_{SB} T_S^4 \frac{\pi D_{bed}^2}{4} - u_{gas} \overline{C_{p,gas}} (T_{bed} - T_{gas,IN}) \frac{\pi D_{bed}^2}{4} = 0 \quad (IV.1)$$

where  $\alpha$  and  $\varepsilon$  are the fluidized bed absorptivity and emissivity, respectively,  $\overline{Q}_{IN}$  is the full power impinging on the fluidized bed surface due to the Xe-lamps,  $\sigma_{SB}$  is the Stefan–Boltzmann constant,  $T_S$ ,  $T_{bed}$ ,  $T_{gas,IN}$ ,  $T_0$  are the temperature of the bed surface, the bulk bed, the inlet gas and the environment, respectively,  $D_{bed}$  is the internal diameter of the reactor,  $u_{gas}$  is the inlet gas velocity and  $\overline{C_{p,gas}}$  is the mean specific heat of the gas averaged over the temperature range  $[T_{gas,IN}, T_{bed}]$ .

By considering an inlet gas temperature ( $T_{gas,IN}$ ) of 600 °C and a value of 0.9 for both  $\alpha$  and  $\varepsilon$  (grey-body behaviour assumption), a required power of 2300 W can be estimated. This value was then increased of a 25% factor to account for the heat losses due to conduction through the external wall, obtaining a total required power of 2900 W, which leads to use three 4 kW<sub>el</sub> Xe-lamps. This also justify the previously made assumption of having considered an impinging flux of 3000 kW m<sup>-2</sup> for the estimate of the bed surface temperature through the compartmented model. Concerning instead the assumption of neglecting the heat of the calcination reaction, the following considerations are valid: assuming an initial mass of limestone equal to 150 g, which is nearly the 15%<sub>wt</sub> of the total bed inventory, an energy of 270 kJ would be required for a complete calcination. By spreading this energy over an average reaction time of 20 min (*Coppola et al.*, 2013), a power of nearly 200 W is obtained, thus less than the 7% of the total amount of 2900 W. Moreover, it should be also considered that during the CaL process the reactions are far from being complete (see Chapter II): considering an average carbonation degree of 25%, the relevance of the calcination contribute over the whole energy balance is further reduced.

### IV.3 Mechanical Design of the Solar Fluidized Bed Reactor

The solar reactor is composed of four main parts assembled together, which correspond to the windbox section, the reaction section, the distribution grid and an upper conical section that ends with a window to let enter the solar simulated radiation. All the parts are made of AISI 310 stainless steel.

The windbox (Figure IV.2-A) consists of a 4 inch diameter pipe, Sch. 40 (ID: 102 mm), 135 mm long. It is closed on the lower side, except for a central aperture connected to a 12 mm

diameter pipe (ID: 10 mm) used for the fluidizing gas inlet. The upper part of the windbox is instead welded to a flange, 20 mm thick, with an inner diameter of 102 mm and an outer diameter of 190 mm. Six equispaced 12.5 mm holes are drilled on a flange circumference of 165 mm. Lastly, a groove with a diameter of 140 mm and a depth of 7 mm is excavated in the upper part of the flange to host the distribution grid placed between two gaskets.

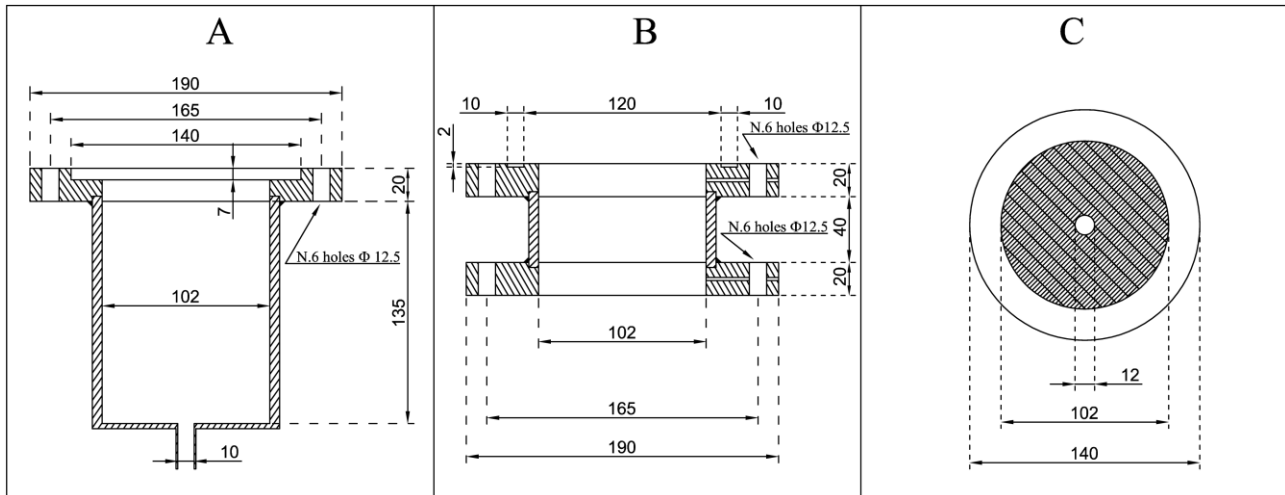


**Figure IV.2:** Technical drawing of: A) windbox; B) reaction section; C) distribution grid. Dimensions are expressed in mm.

The reaction section (Figure IV.2-B) consists of a 4 inch diameter pipe, Sch. 40 (ID: 102 mm), 40 mm long. It is welded to a flange on both sides. Both flanges are 20 mm thick, have an inner diameter of 102 mm and an outer diameter of 190 mm. Moreover, both flanges have six equispaced 12.5 mm holes drilled on a circumference of 165 mm, so as to fit the windbox section on one side and the upper conical section on the opposite side. An annular groove with an outer diameter of 140 mm, an inner diameter of 120 mm and a depth of 2 mm is excavated in the upper flange to host a gasket. Lastly both flanges have, at half-height, a small cylindrical hole directed from the outer to the inner diameter of the flange and used to host a thermocouple and a pressure tap.

The gas distributor (Figure IV.2-C) consists of a set of three stainless steel wire meshes (grid finer than 50  $\mu\text{m}$ ) welded between two metallic rings with an inner and outer diameter of 102 and 140 mm, respectively. A small central aperture is made in the gas distributor to permit the insertion of the central nozzle, which consists of a 6 mm AISI 310 pipe (ID 4 mm) with a fine metallic net (finer than 50  $\mu\text{m}$ ) at the tip to prevent the backflow of bed solids.

The upper conical section (Figure IV.3), consists of a 3 mm thick AISI 310 sheet calendered so as to have a conical shape with a lower inner diameter of 102 mm and an internal cone angle of 32°. The height of the conical section is 400 mm, which results in an upper inner diameter of 600 mm. Both sides of the conical section are welded to 20 mm thick flanges: the lower one is designed so as to fit the reaction section, while the upper one has an inner diameter of 600 mm, an outer diameter of 700 mm and sixteen equispaced 12.5 mm holes drilled on a circumference of 670 mm. A groove with a diameter of 635 mm and a depth of 12 mm is excavated in the upper flange to host the optically accessible window and two gaskets. A counter-flange has also been made to slightly squeeze the two gaskets on the window in order to seal the upper part of the reactor and avoid gas leakage. Close to the half-height of the conical section, four equispaced pipes of 1



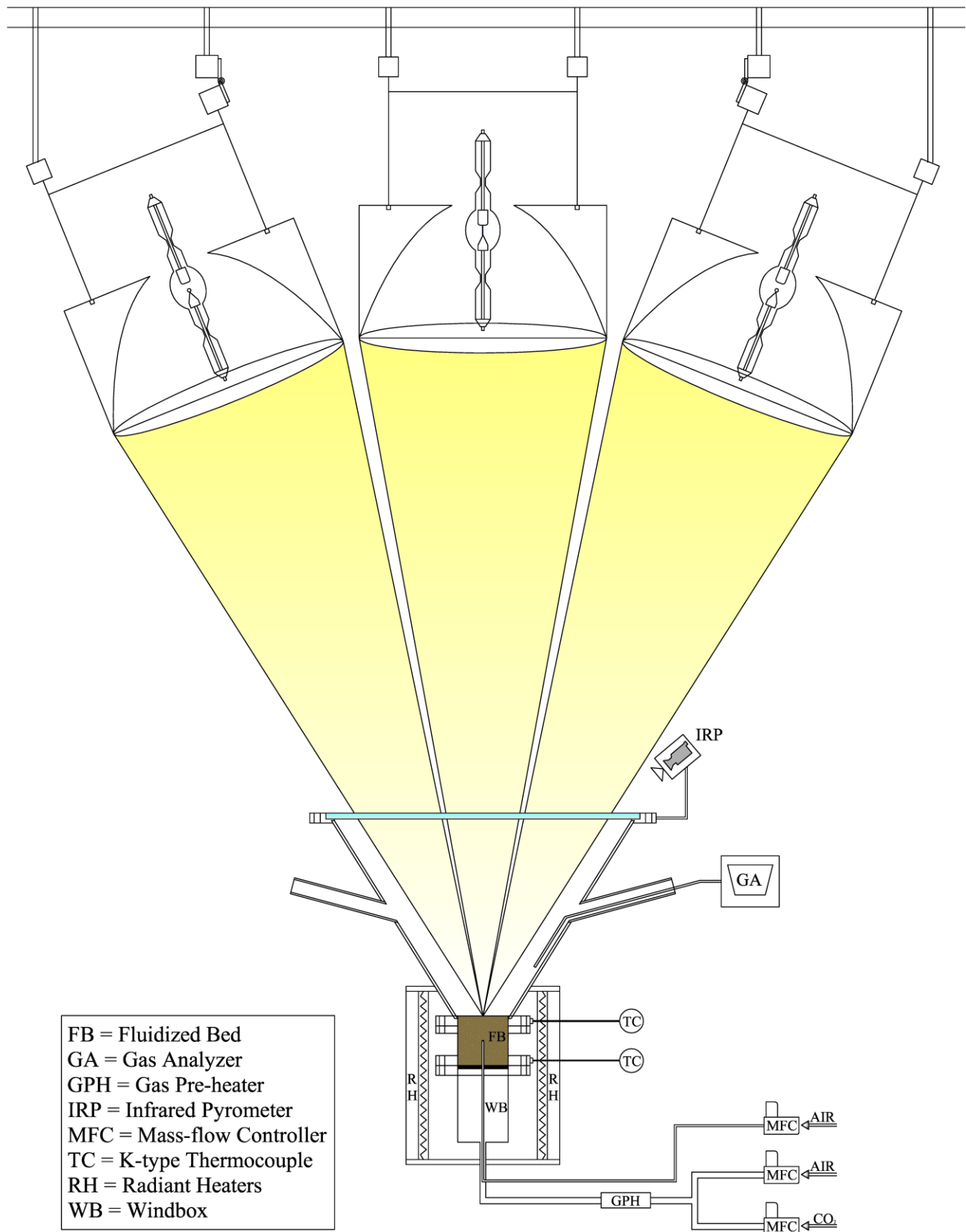


**Figure IV.4:** Outline of the solar fluidized bed reactor with its ancillary equipment.

#### **IV.4.1 Semi-Cylindrical Ceramic Fiber Heaters**

The two semi-cylindrical ceramic fiber heaters mounted around the fluidized bed reactor are made by Watlow and are schematically shown Figure IV.5.

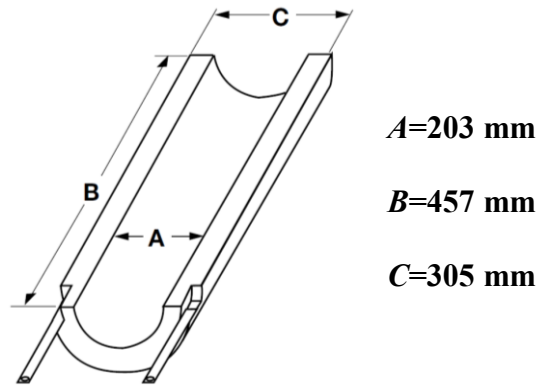


**Figure IV.5:** Technical drawing of the semi-cylindrical heaters.

These elements are made of high temperature iron-chrome-aluminium heating elements covered with ceramic (alumina-silica) fiber insulation and accomplish two main tasks: i) heating of the reaction chamber, and ii) isolating of the internal chamber from the outside. The heat transfer mechanism is only radiative, and operating temperatures as high as 1200 °C can be achieved.

The internal diameter of the semi-cylindrical elements (*A*) is 203 mm and the overall length (*B*) is 457 mm. The total power is 5000 W at 240 V. As these heaters are not self-controlled, a PID controller connected to one of the K-type thermocouples inserted into the bed bulk is used to set the bed temperature at the desired value. The ceramic fiber heaters are not used when performing the calcination reaction which is accomplished only through the solar simulator.

#### **IV.4.2 Gas Preheater**

The gas preheater is a stainless steel pipe of 3/8 inch diameter, threaded at the extremities and made by Osram Sylvania (Figure IV.6). A serpentine-coil electric heater element runs along the entire interior of the tube. The maximum power of the heating element is 1600 W at 170 V. As for the ceramic fiber heaters, the elements are not self-controlled, thus a K-type thermocouple placed at 1 inch from the heater exit is used in combination with a PID controller to achieve the desired value of the inlet temperature of the fluidizing gas.

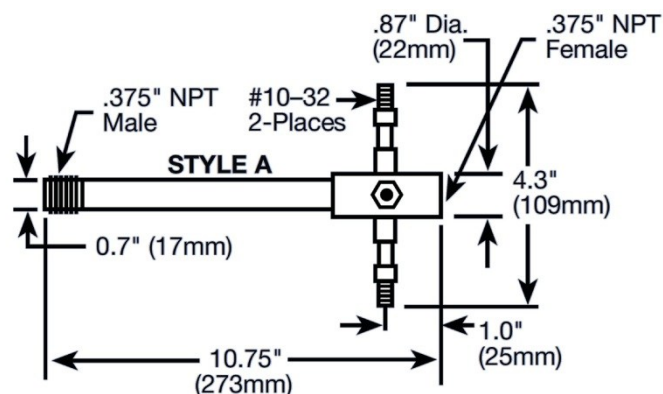


**Figure IV.6:** Sketch of the gas preheater.

### IV.4.3 Infrared Pyrometer

The infrared pyrometer used for the measurement of the bed surface temperature is an Optris CT Laser 2MH1-SF and is schematically shown in Figure IV.7.

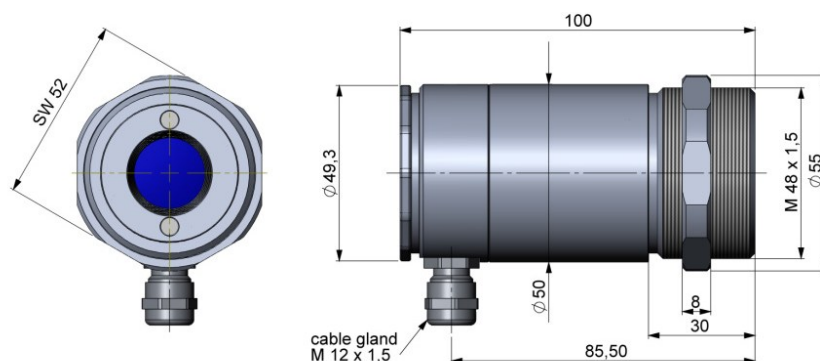


**Figure IV.7:** Sketch of the infrared pyrometer.

Unlike the thermal infrared camera used in the previous experiments, which was able to completely map the fluidized bed surface, the infrared pyrometer measures the space-averaged temperature in a limited portion of the bed surface. The dimensions of the measured area are dependent on both the optics of the pyrometer and the gap between the pyrometer and the target object. More in detail, the optics of the used pyrometer has a converging-diverging profile (Figure IV.8): the spot size is 12 mm at sensor level, converges to a minimum size of 3.7 mm at the focus distance of 1100 mm and then starts to indefinitely increase (e.g., spots sizes of 9.4 and 16.5 mm are obtained at 1500 and 2000 mm distances). A double laser is integrated in the pyrometer so to mark the real measurement spot location and spot size at any distance on the object surface.

The temperature is calculated by the pyrometer on the basis of the emitted infrared radiation in the  $1.6 \mu\text{m}$  spectral range: this feature enables to read temperatures even through a glass window (transmittance  $> 0.85$  in the  $0.4\text{--}2.5 \mu\text{m}$  range). This is the main reason why it was not possible to use the Optris PI-400 infrared camera (spectral range:  $7.5\text{--}13 \mu\text{m}$ ) during the operation of the solar reactor. The calibration range of the infrared pyrometer is  $490\text{--}2000 \text{ }^\circ\text{C}$ . Temperature data are continuously acquired and logged on a PC. As for the thermal infrared camera, a proper value for the emissivity of the material, whose temperature has to be detected, must be set. For silica sand, a value of 0.9 was obtained by measuring bed surface temperature with both the pyrometer and a K-type thermocouple under bubbling fluidized bed conditions. Moreover, a comparison between the temperature read by the thermal infrared camera and that measured by the pyrometer was performed under fixed bed conditions with a Xe-lamp focused on bed surface in order to evaluate a possible interference due to the part of the incident radiation which is reflected by the fluidized particles. The comparison showed a difference between the two temperature values of less than  $10 \text{ }^\circ\text{C}$  in the  $900\text{--}1200 \text{ }^\circ\text{C}$  range. During the experimental test, the pyrometer was pointed at the centre of the fluidized bed surface and the spot dimension approached an area of nearly 5 mm diameter.

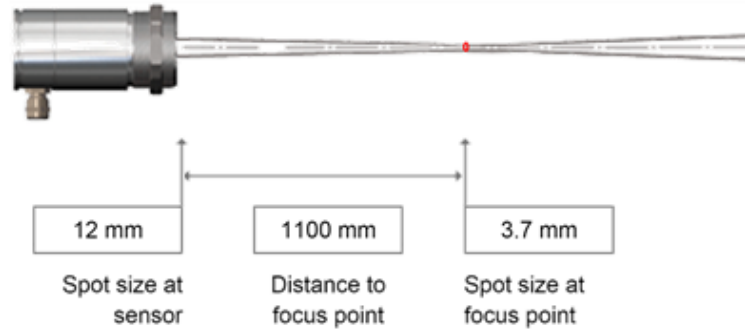


**Figure IV.8:** Sketch of the infrared pyrometer optics.

#### ***IV.4.4 Gas Analyzer***

An Advance Optima ABB AO2020 (Uras 14, 0–95%<sub>v</sub>) was used to monitor the CO<sub>2</sub> concentration at the exhaust. The measurement is based on the NDIR principle. The fine calibration of the analyzer was performed through the use of two gaseous streams: pure N<sub>2</sub> (99.7%<sub>v</sub>) and a 1:1 mixture N<sub>2</sub>-CO<sub>2</sub> (50.1%<sub>v</sub>). The instrument has four calibration ranges for best accuracy (0–5%<sub>v</sub>; 0–20%<sub>v</sub>; 0–50%<sub>v</sub>; 0–95%<sub>v</sub>), and the optimal one is self-selected according to the experienced CO<sub>2</sub> concentration. The gas collection is realized through a probe made of a 6 mm stainless steel pipe (ID 4 mm), inserted in the reactor through one of the four outlet pipes and located at an height of 15 cm from the bed surface. A suction pump is calibrated so as to collect a gas stream of nearly 60 Ndm<sup>3</sup> h<sup>-1</sup>. A filter made of steel wool is interposed between the pump and the reactor to avoid that fine solid particles reach the analyzer.

#### ***IV.4.5 Materials***

The materials used for the experimental tests are inert silica sand from Ticino river (Italy) and an Italian limestone (termed Massicci). The main properties of the materials are reported in Table IV.1, together with the theoretical minimum fluidization value ( $u_{mf}^t$ ), evaluated according to the classical Wen–Yu equation.

<b>Material</b>	$\rho_{particle}$ [kg m <sup>-3</sup> ]	<b>Size range</b> [μm]	$u_{mf}^t$ @ 650 °C [m s <sup>-1</sup> ]	$u_{mf}^t$ @ 950 °C [m s <sup>-1</sup> ]
Ticino sand	2400	850–1000	0.32	0.27
Massicci limestone	2200	420–590	0.08	0.07

**Table IV.1:** Main physical parameters for Ticino sand and Massicci limestone.

Ticino sand is an alluvial origin sand, naturally rounded, polychrome in colour and with a SiO<sub>2</sub> content of 83–86% and about 4% of mica. It has a high resistance to heat (1500–1700 °C). Massicci is an Italian limestone with a high Ca-content. A TGA analysis was performed on the raw limestone (Figure IV.9) at an heating rate of 10 °C min<sup>-1</sup>, from 25 to 870 °C, under N<sub>2</sub> atmosphere. The results show a CaCO<sub>3</sub> content close to 90%<sub>wt</sub>, even though it must be pointed out that higher TGA temperatures (unfortunately not reachable with the instrument at hand) would have led to calculate an even larger CaCO<sub>3</sub> content, that is then expected to be over 90%<sub>wt</sub>. This is in agreement with an earlier paper (Coppola *et al.*, 2013) that reports a 97.4%<sub>wt</sub> CaCO<sub>3</sub> content for this sorbent. XRD

analysis results further confirm the high purity of the sample (Figure IV.10): only calcite peaks are in fact detected.

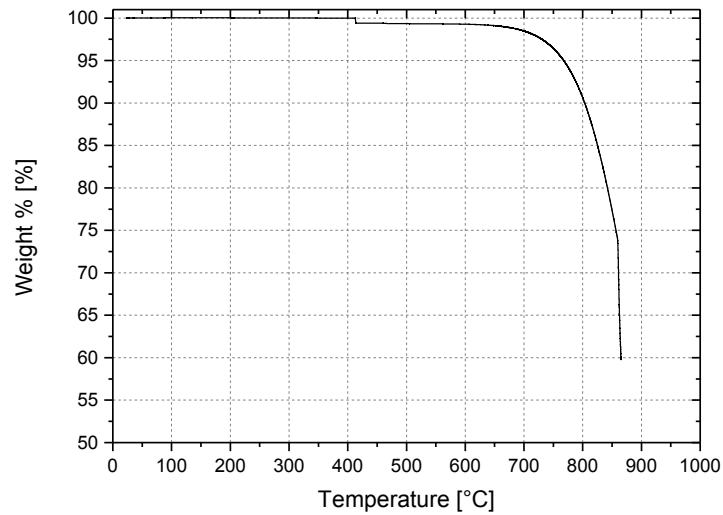


**Figure IV.9:** TGA analysis for the Massicci limestone.

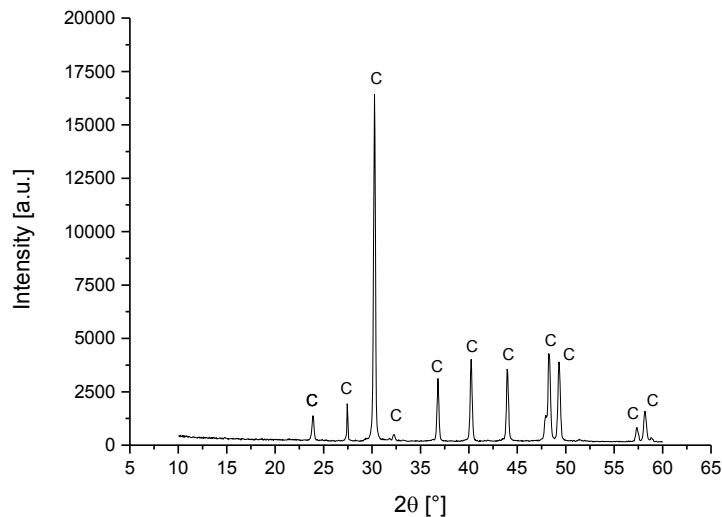


**Figure IV.10:** XRD analysis for Massicci limestone. C=calcite ( $\text{CaCO}_3$ , PDF 01-080-3277).

## IV.5 Characterization of the Solar Simulator

The characterization of the solar simulator was performed following the same procedure previously described (see § III.3.2.2). The three lamps were focused at the centre of the fluidized bed surface and the spatial flux distribution of each lamp was obtained independently from the others but with the infrared camera placed in a fixed position. Finally, the three spatial flux distributions were algebraically summed in order to obtain the overall heat flux distribution (Figure IV.11). A peak flux of nearly  $3000 \text{ kW m}^{-2}$  has been obtained, while the average flux over the whole reactor diameter is equal to  $390 \text{ kW m}^{-2}$ . Finally, by integrating the radiative flux over the whole bed area, a total irradiated power of 3200 W is obtained.

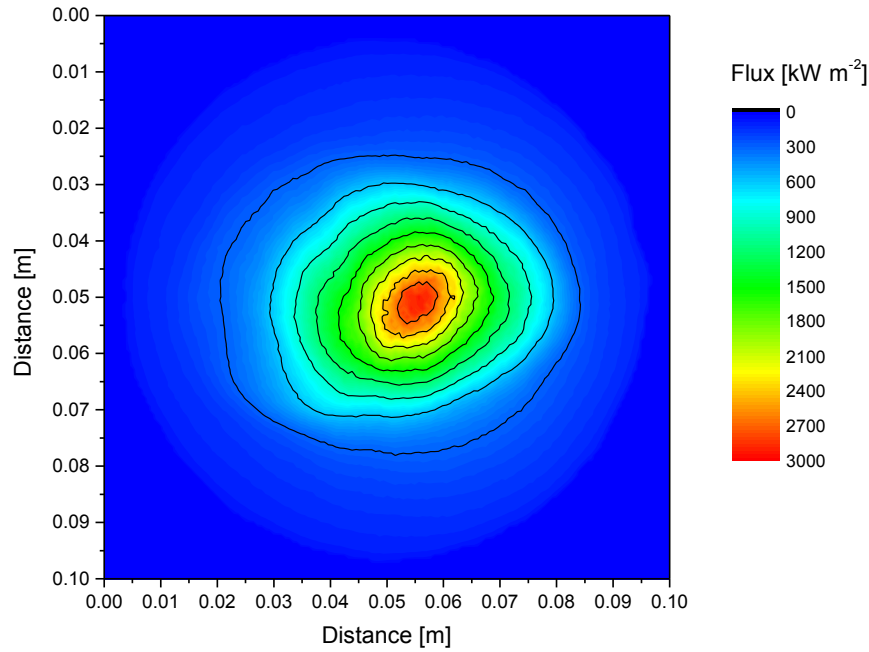


**Figure IV.11:** Contour chart of the spatial distribution of radiative heat flux incident on the bed surface.

## IV.6 Experimental Procedure

The experimental tests consisted of four calcination/carbonation cycles on the Massicci limestone. Both reactions were performed in the same fluidized bed reactor by gradually switching the operating parameters between the calcination and carbonation conditions. Operating parameters resembled when possible those used in *Coppola et al.* (2013), for comparison purposes. More in detail, the carbonation reaction was performed at a bulk bed temperature of nearly 650 °C and with an inlet CO<sub>2</sub> concentration close to 15%<sub>v</sub>, which is a typical value found in combustion flue gases. On the other hand, the calcination reaction was performed at a bulk bed temperature of nearly 940 °C and with an inlet CO<sub>2</sub> concentration close to 70%<sub>v</sub>, which is a typical value encountered in oxyfuel calcination reactors. The fluidizing gas velocity was set at 0.6 m s<sup>-1</sup> for both the calcination and carbonation step. It is observed that  $u_{gas}$  is nearly twice the sand minimum fluidization velocity. Operating conditions are summarized in Table IV.2.

Reaction	$T_{bed}$ [°C]	Inlet CO <sub>2</sub> [% <sub>v</sub> ]	$u_{gas}$ @ $T_{bed}$ [m s <sup>-1</sup> ]
Carbonation	650	15	0.6
Calcination	940	70	0.6

**Table IV.2:** Operating conditions for the carbonation and calcination reactions.

As previously discussed, only the calcination step was performed with the use of the solar simulated radiation while the carbonation step was performed with the only use of the radiant heaters and the gas preheater. Nearly 730 g of sand and 125 g of limestone were used at the beginning of the test. The course of the reactions was followed by measuring the CO<sub>2</sub> concentration at the exhaust. The following experimental procedure was followed (the material –sand/limestone– initially fed to the reactor remained into the system with no bed drain after each stage):

1. Charge of the bed material (silica sand) in the fluidized bed reactor;
2. Heating up the reactor up to 850 °C through both the electric heaters and the gas preheater;
3. Setting-up the calcination conditions:  $\text{CO}_{2,\text{IN}} = 70\%_{\text{v}}$ , gas velocity  $0.6 \text{ m s}^{-1}$  @ 940 °C;
4. Shutdown of the electric heaters, feeding of the limestone in the fluidized bed reactor, and power-up the three Xe-lamps;
5. Waiting for the calcination step to be complete (stable  $\text{CO}_2$  concentration at the exhaust);
6. Shutdown of the Xe-lamps and cooling down of the bed to 400 °C in air atmosphere;
7. Setting-up of the carbonation conditions:  $\text{CO}_{2,\text{IN}} = 15\%_{\text{v}}$ , gas velocity  $0.6 \text{ m s}^{-1}$  @ 650 °C;
8. Fast heating through both the electric heaters and the gas preheater up to 650 °C;
9. Waiting for the carbonation step to be complete (stable  $\text{CO}_2$  concentration at the exhaust);
10. Heating up the reactor up to 750 °C through the electric heaters;
11. Switching to the calcination conditions and heating up of the reactor to 850 °C through the electric heaters;
12. Shutdown of the electric heaters, and power-up the three Xe-lamps.

The points from 5 to 12 were repeated in order to achieve four complete calcination/carbonation cycles. It is worth to note that, during the points 7–11, the operating conditions are such that the calcination process is not thermodynamically favoured. Only when then Xe-lamps are powered on, point 12, the increase of temperature makes the calcination process thermodynamically favoured. This can be understood by following the experimental procedure on the  $P_{\text{CO}_2}$  vs.  $T$  plot (Figure IV.12).

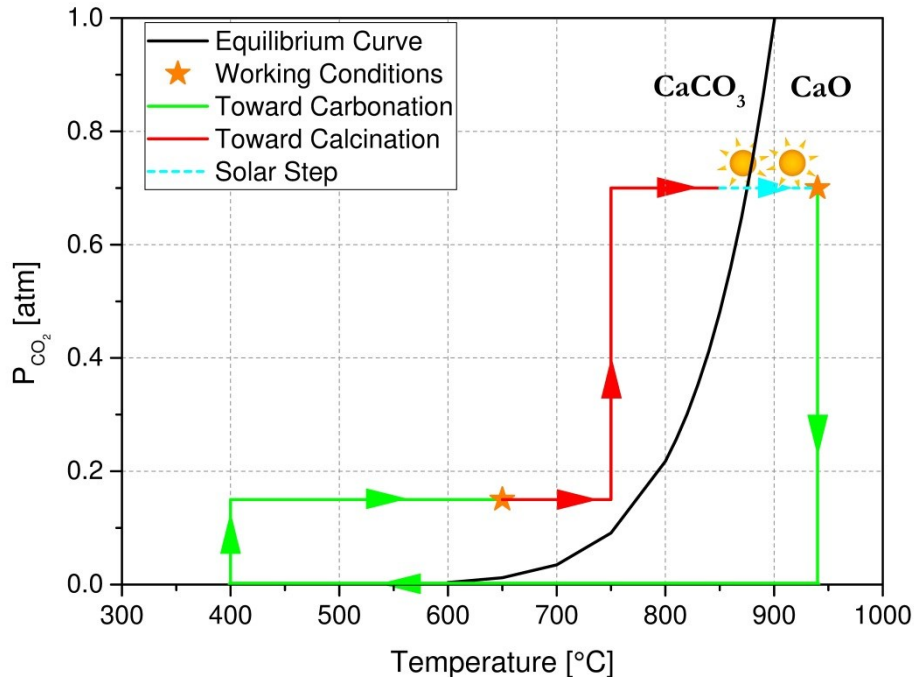


**Figure IV.12:** Pathway of the calcination/carbonation cycle carried out during the experimental procedure and viewed on the  $P_{\text{CO}_2}$  vs.  $T$  diagram, together with the equilibrium curve of  $\text{CaCO}_3$  decomposition.

Data of time, temperature and  $\text{CO}_2$  concentration were continuously acquired at 1 Hz through an ad-hoc developed LabVIEW program. The  $\text{CO}_2$  capture capacity of the sorbent is evaluated by integrating the  $\text{CO}_2$  profile of the carbonation reaction over the reaction time with respect to the baseline. The effect of expansion/reduction of the volumetric stream due to the occurrence of a

chemical reaction with increasing/decreasing overall mole number was considered negligible. TGA and XRD analyses were performed on a limestone sample after the first calcination in order to confirm the complete calcination of the sample before that the carbonation reaction occurs. To this end, a specific sample was prepared by stopping the above described procedure to the point 6 and cooling down the bed to ambient temperature.

## IV.7 Results and Discussion

### IV.7.1 A Complete Calcination-Carbonation Cycle

Figure IV.13 reports the typical chart plot of the first calcination-carbonation cycle. The initial time instant reported in the graph,  $t = 0$  s, is near the end of the point 2 of the experimental procedure. The blue and red curves show the temperature inside the fluidized bed reactor acquired by the two K-type thermocouples (“up” and “down”, respectively) the cyan curve refers to the data acquired by the pyrometer, and the black curve reports the CO<sub>2</sub> outlet concentration as measured by the gas analyzer. It is possible to observe the set-up of the calcination conditions at 250 s, where the CO<sub>2</sub> concentration grows from 0 to nearly 70%<sub>v</sub> while the reactor is still heated through the ceramic fiber heaters. During this phase, the temperature measured by the upper thermocouple is lower than the bottom bed value due to both an asymmetric positioning of the ceramic heaters (which are closer to the bottom section of the reactor) and the larger heat exchange toward the environment that occurs in the upper section of the reactor. The limestone feeding and the Xe-lamps ignition occur at almost the same time instant of nearly 1250 s. The charge of cold limestone particles can be recognized by the decrease of bed temperature, whereas the power-up of the lamps is easily detectable from the steep increase of the bed surface temperature measured by the pyrometer. The increase in the temperature measured by the two in-bed thermocouples is fast too, and a temperature of 935–940 °C is rapidly approached in almost 500 s. It is also interesting to note that, with the Xe-lamps turned on, there is an inversion in the trend of the temperatures measured by the two thermocouples, as now the upper one reads slightly higher values. Data of the bed surface temperature highlight instead a continuous fluctuation as a result of the competition between the highly concentrated radiation impinging on the fluidized bed surface and the continuous bubble bursting phenomena. The temperature values fluctuate between 1000 and 1150 °C, with a mean temperature of 1080 °C and a standard deviation of 30 °C. The time-averaged over-temperature measure is, in turn, almost 140 °C, comparable with the designed value obtained with the compartmented model. It is also worth to note that, around 1250 s, when the limestone is fed to the reactor, the temperature decrease can be also due to the start of the calcination reaction. The increase in the CO<sub>2</sub> concentration is, as expected from literature data (*Coppola et al.*, 2013), of nearly 1%. The calcination reaction ends at nearly 2500 s, with a total duration time of nearly 20 min.

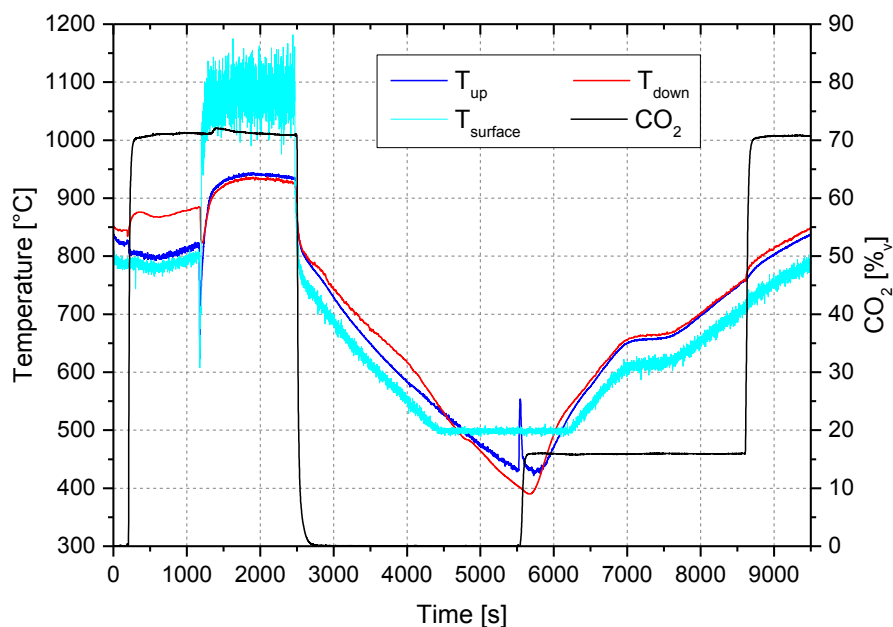


**Figure IV.13:** Bed temperatures and CO<sub>2</sub> concentration time-series during the first calcination-carbonation cycle.

At the end of the first calcination, CO<sub>2</sub> is no more fed to the reactor, and its concentration falls down to 450 ppm, a value close to the atmospheric CO<sub>2</sub> concentration. The temperature is then decreased down to nearly 400 °C by switching off all the heaters and using air at ambient temperature (15–20 °C) as fluidizing gas. This step goes from 2500 s to nearly 5500 s. Then, around 5500 s, when the targeted temperature is reached, CO<sub>2</sub> with a concentration of nearly 15%<sub>v</sub> is fed to the reactor. From this time instant, the temperature is increased as fast as possible up to 650 °C remaining quite stable at that value between 7000 and 7600 s. A temperature peak is also detectable for the “up” measure and is related to the heat release of the carbonation reaction at about 5500 s. During the carbonation reaction, there is a decrease in the CO<sub>2</sub> concentration of nearly 0.1–0.2% which, as for the calcination reaction, is barely detectable in the reported graph due to the adopted CO<sub>2</sub> scale. The carbonation reaction starts at 5500 s and ends at nearly 7600 s if a final temperature of 650 °C is considered (total reaction time 35 min) or at nearly 8500 s if a final temperature of 750 °C is considered (total reaction time 50 min). Finally, at 8500 s, the CO<sub>2</sub> concentration is increased again up to the 70%<sub>v</sub> calcination value and the cycle is repeated. Under these experimental conditions, a full calcination-carbonation stage has then an operating duration close to 140 min.

#### **IV.7.2 Detailed Analysis of the First and Fourth Carbonation Steps**

Figure IV.14 reports the data related to the course of the first and the fourth carbonation steps, with indications of only inner bed temperatures and outlet CO<sub>2</sub> concentration. Time values on the abscissa are the same as those reported in Figure IV.13. As highlighted before, the blue and red curves show a fast increase from the initial temperature toward the scheduled value of 650 °C, followed by a plateau at nearly 650 °C and a final increase toward 750 °C. The use of a reduced scale for the CO<sub>2</sub> concentration allows now to appreciate the decrease in the CO<sub>2</sub> concentration profile induced by the CaO carbonation reaction. The area between the baseline (dashed curve) and the CO<sub>2</sub> concentration profile, highlighted in green in the graphs, is proportional to the amount of CO<sub>2</sub> captured by the sorbent. It is interesting to note that the reaction starts as soon as the

temperature is increased, and well before the achievement of the scheduled temperature of 650 °C. Moreover, even though the major contribute to the carbonation reaction is detectable for temperatures up to 650 °C, a small but not negligible contribute can be found when the temperature is increased up to 750 °C. The small increase of the “up” temperature at nearly 5500 s appears to happen before the injection of the CO<sub>2</sub> stream because the signals of temperature and concentration are not synchronized and actually a time delay of about 80–100 s between outlet CO<sub>2</sub> concentration and bed temperature time-series exists. By comparing the data of the first and fourth carbonation it is clearly recognizable that, during the fourth carbonation, the sorbent undergoes a lower carbonation level with respect to the first cycle. Moreover, the temperature increase when CO<sub>2</sub> starts to be fed is no more observed for the fourth carbonation, probably due to a worse material reactivity (*vide infra*).

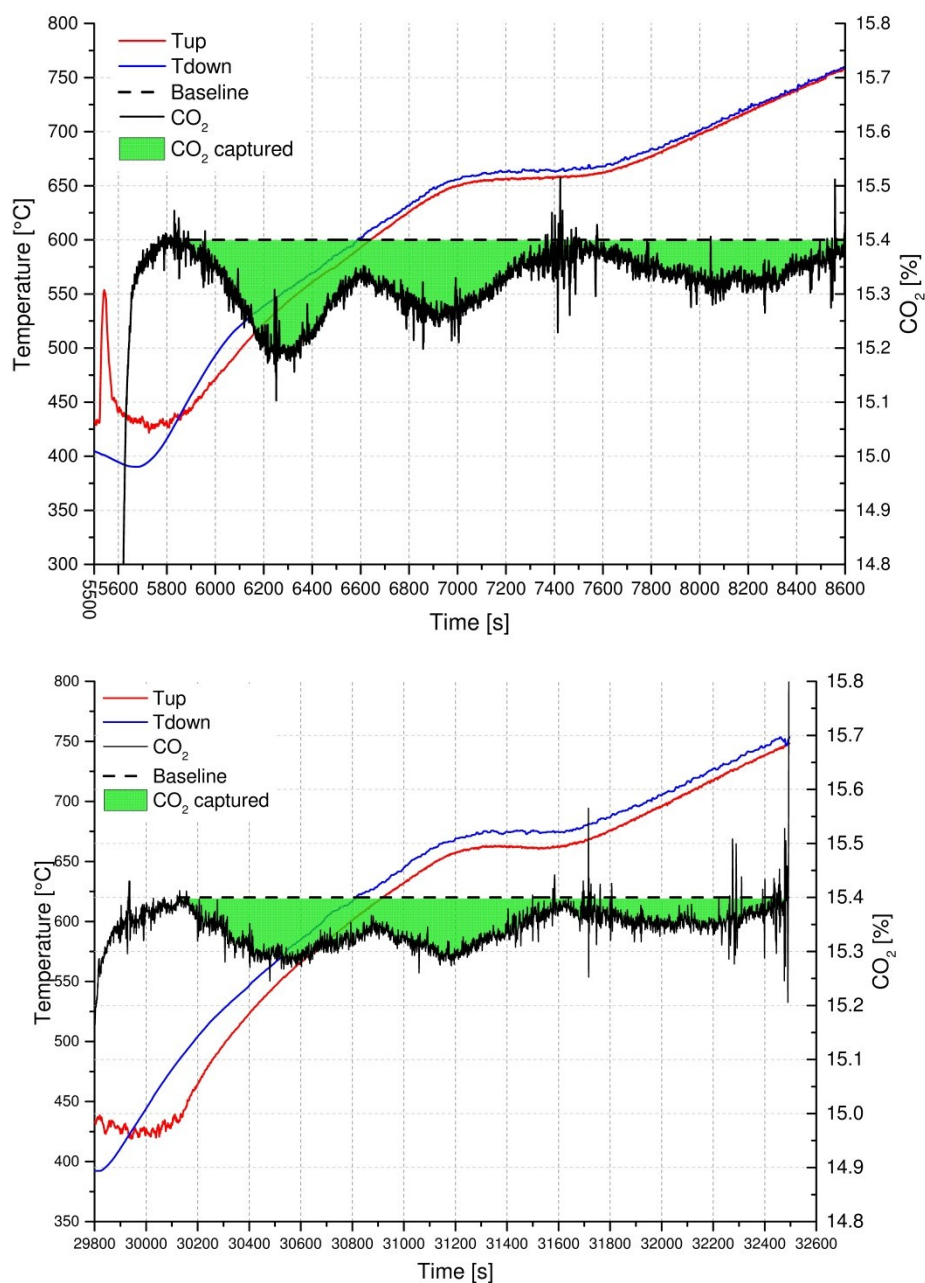


**Figure IV.14:** Bed temperature and outlet CO<sub>2</sub> concentration time-series measured during the first (up) and fourth (down) carbonation step. The dashed line indicates the inlet CO<sub>2</sub> concentration.

### IV.7.3 TGA and XRD Analysis of the Calcined Sample

Figure IV.15 reports the TGA analysis results of the sample obtained after the first calcination. The analysis was performed from ambient temperature to 870 °C under N<sub>2</sub> atmosphere, at an heating rate of 10 °C min<sup>-1</sup>. By comparing the weight of the sample at 600 °C (well before CaCO<sub>3</sub> thermal decomposition could take place) and the final weight, a residual amount of barely 8.0%<sub>wt</sub> CaCO<sub>3</sub> is estimated in the sample, thus concluding that the material has been extensively calcined in the solar reactor before the carbonation step occurs. This result is also confirmed by the XRD analysis results (Figure IV.16) which shows a marked presence of CaO and only feeble peaks ascribed to CaCO<sub>3</sub>. Weight loss before 600 °C (Figure IV.15) and portlandite signals (Figure IV.16) are due to uncontrolled CaO weathering in the sample after the fluidized bed test.

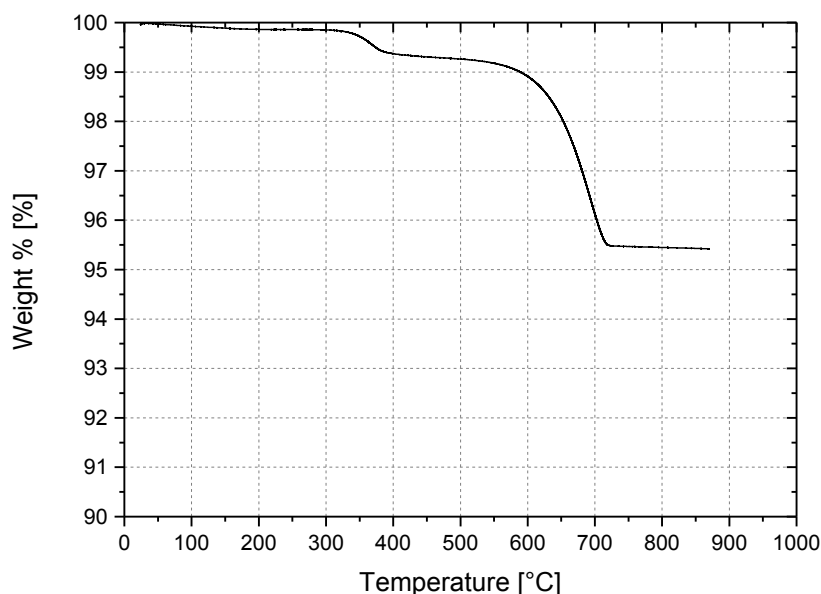


Figure IV.15: TGA analysis for the sorbent after the first calcination step.

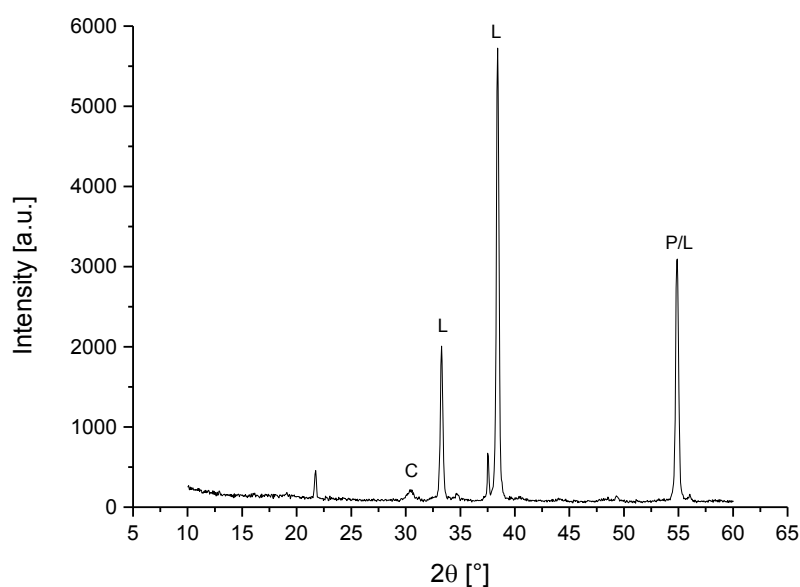


Figure IV.16: XRD analysis for the sorbent after the first calcination step. C=calcite (CaCO<sub>3</sub>, PDF 01-080-3277); L=lime (CaO, PDF 00-003-1123), P=portlandite (Ca(OH)<sub>2</sub>, PDF 00-002-0968).

#### IV.7.4 $\text{CO}_2$ Capture Efficiency

The data of  $\text{CO}_2$  capture capacity achieved by the sorbent in the CaL process as a function of the carbonation stage are summarized in Table IV.3: data evaluated up to a final carbonation temperature of both  $650\text{ }^\circ\text{C}$  and  $750\text{ }^\circ\text{C}$  are reported. Data referred to  $750\text{ }^\circ\text{C}$  are also plotted in Figure IV.17. The maximum carbonation degree is achieved during the 1<sup>st</sup> carbonation, when the sorbent is freshly calcined: a value of 9.5% is obtained ( $0.042\text{ g}_{\text{CO}_2}\text{g}_{\text{initial sorbent}}^{-1}$  at  $750\text{ }^\circ\text{C}$ ). For the 2<sup>nd</sup> carbonation, the carbonation degree decreases down to nearly 7% ( $0.031\text{ g}_{\text{CO}_2}\text{g}_{\text{initial sorbent}}^{-1}$  at  $750\text{ }^\circ\text{C}$ ). This was expected, due to the thermal sintering effects suffered by the sorbent particles especially under calcination. A further decrease in the carbonation degree is observed for the 3<sup>rd</sup> carbonation, where a value of 6% ( $0.027\text{ g}_{\text{CO}_2}\text{g}_{\text{initial sorbent}}^{-1}$  at  $750\text{ }^\circ\text{C}$ ) is obtained. But this decrease was smaller than the one observed for the 2<sup>nd</sup> carbonation. Moreover, practically same values were obtained for the 4<sup>th</sup> carbonation, suggesting a desired stabilization of the material performances and a decrease of the sintering relevance. The experimental results obtained for the Massicci limestone are comparable to the ones reported in the literature for tests performed on the same limestone but with conventional heating source (*Coppola et al.*, 2013). It therefore seems that the solar CaL cycle could be a feasible process, as the higher temperatures obtained on the fluidized bed surface appear to not produce a severe worsening of the reactive material properties, whose  $\text{CO}_2$  capture capacity, after a first initial decrease, appears quite stable over CaL cycling.

Carbonation no. [#]	$\text{CO}_2$ Capture Capacity @ $650\text{ }^\circ\text{C}$ [ $\text{g}_{\text{CO}_2}\text{g}_{\text{initial sorbent}}^{-1}$ ]	$\text{CO}_2$ Capture Capacity @ $750\text{ }^\circ\text{C}$ [ $\text{g}_{\text{CO}_2}\text{g}_{\text{initial sorbent}}^{-1}$ ]
1	0.035	0.042
2	0.027	0.031
3	0.020	0.027
4	0.023	0.028

**Table IV.3:**  $\text{CO}_2$  capture capacity for Massicci limestone as a function of the carbonation stage.

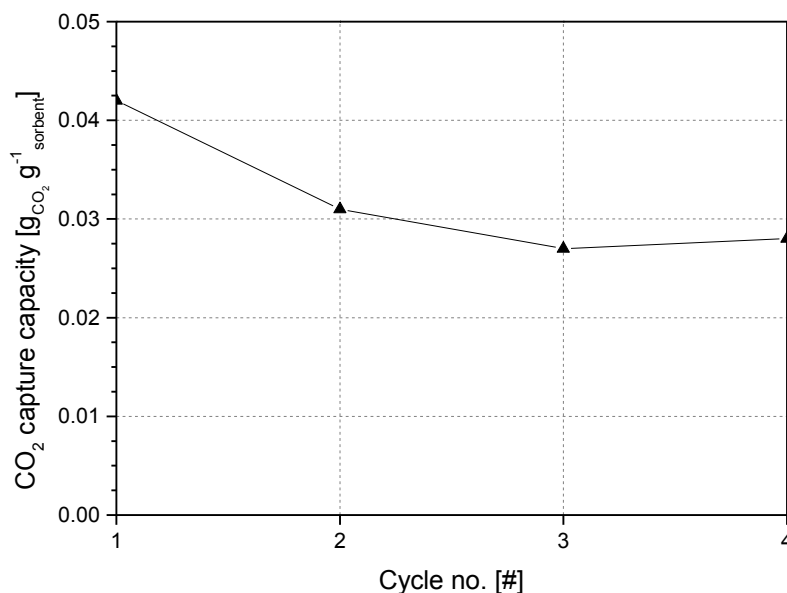


**Figure IV.17:**  $\text{CO}_2$  capture capacity ( $750\text{ }^\circ\text{C}$ ) for Massicci limestone as a function of the carbonation stage.

## IV.8 Final Remarks

A gas–solid fluidized bed reactor suitable for the investigation of thermochemical heat storage processes has been designed and operated to study the solar CaL process. The solar simulation task was achieved by an array of three Xe-lamps of 4 kW<sub>el</sub> each coupled with elliptical reflectors: a total irradiating power to the bed surface of nearly 3200 W was obtained, with a peak flux of 3000 kW m<sup>-2</sup>. Only the calcination step was performed through the use of the solar simulator, while the carbonation step was performed with the use of ceramic fiber heaters. The performance of an Italian limestone (Massicci) were assessed by achieving four complete carbonation-calcination cycles.

Experimental results on the calcination step highlighted a continuous fluctuation of the bed surface temperature as a result of the competition between the high concentrated radiation impinging on the bed surface and the continuous bubble bursting phenomena. A mean bed surface temperature of 1080 °C was detected, corresponding to an over-temperature of 140 °C. The extent of the calcination reaction was confirmed through TGA analysis, which showed a residual amount of CaCO<sub>3</sub> equal to barely the 8%<sub>wt</sub> after the first calcination step.

The CO<sub>2</sub> capture capacity of the Massicci limestone showed a first initial decreasing trend followed by a stabilization at lower values. A carbonation degree of 9.5% was achieved during the first cycle, while the residual CO<sub>2</sub> capture capacity was estimated to be around 6%. The experimental results obtained in this work are comparable to the ones reported in the literature for tests performed on the same limestone but with conventional heating source. The solar CaL process appears to be a practical way toward the integration of conventional fossil fuels and energy sources, with the aim of both taking advantage of the solar energy and reducing the CO<sub>2</sub> emissions.

## Chapter V. Final Remarks and Future Developments

In the present PhD Thesis an integration between solar energy and conventional fossil fuels sources has been proposed. An integrated scheme of a continuous Calcium Looping (CaL) process for CO<sub>2</sub> capture from combustion flue gases of a power plant, based on Fluidized Bed (FB) technology and sustained by a Concentrated Solar Power (CSP), was developed. Storage of the excess incident solar power during the daytime as calcined sorbent, which is eventually utilized in the CaL loop during the nighttime, was proposed to overcome the inherently unsteadiness of CSP systems. The potentialities of a similar integrated scheme were assessed by means of model computations to estimate the main features, performance, storage and energy requirements of the process. In order to study the practical feasibility of the process, directly irradiated FB systems were considered, as the direct heating configuration permits to obtain the high operating temperatures required to perform the calcination reaction. Initial studies were targeted at the comprehension of the heat transfer phenomena in directly irradiated FB, with the aim of establishing the efficiency of the solar FB receiver. Finally, a directly irradiated gas–solid FB reactor suitable for the investigation of thermochemical heat storage processes has been designed and operated to study the solar CaL process. Several calcination-carbonation reactions were performed on an Italian Ca-based sorbent (Massicci), and its CO<sub>2</sub> capture capacity was evaluated over repeated cycling. The following main results have been obtained in the present PhD Thesis:

- Model computations suggested that in order to couple a CSP with a 100 MW<sub>th</sub> combustion plant, the use of two storage vessels of nearly 2000 m<sup>3</sup> is required together with the building of an heliostat field of 0.26 sqkm. However, thanks to the heat recovery in the carbonator, the overall thermal throughput of the power plant is increased from 100 MW<sub>th</sub> to nearly 150 MW<sub>th</sub>. It was also highlighted that larger inlet Ca/C molar ratio could result into a higher CO<sub>2</sub> capture efficiency but at the expense of larger energy consumption;
- Collection of incident radiation changes from a surface-receiver to a volumetric-receiver paradigm as the gas superficial velocity is increased from fixed to bubbling fluidized bed conditions: this also results in a significant reduction of peak temperature and temperature fluctuations at the focal point of the receiver. A compartmental heat transfer model which provides a simple, though accurate, equation for predicting in-bed dispersion of radiative power and extent of temperature non-uniformity was developed. Moreover, a strong reduction of bed surface temperature has been obtained by exploring uneven fluidization strategies and, in turn, by tailoring the hydrodynamics of the bed through injecting a chains of bubbles from a nozzle located in the proximity of the radiation focal point;
- Operation of the directly irradiated FB reactor for the calcination reaction resulted into a continuous fluctuation of the bed surface temperature, with a mean over-temperature value of nearly 140 °C. The CO<sub>2</sub> capture capacity of the investigated limestone showed a first initial decreasing trend followed by a stabilization at lower values, with a residual CO<sub>2</sub> capture capacity of about 6%.

The solar CaL process appears to be a practicable way toward the integration of conventional fossil fuels and energy sources, with the aim of both taking advantage of the solar energy and reducing CO<sub>2</sub> emissions. Future developments could be aimed at:

- Investigating alternative schemes of integrated CaL-CSP processes with the aim of reducing the large required storage capacity. A calciner operated in transient mode, with an unsteady bed inventory (increasing during day-operations and decreasing during night-operations), could, for example, result into the need of just a single storage vessel;
- Further exploring the interaction between concentrated solar radiation and FB systems, by mapping the inner FB temperatures at different depths and distances from the focal point of the incident radiative flux, to evaluate the effectiveness of the heat transfer mechanisms between the bed surface and the bulk of the bed;
- Studying the tailoring of the bed surface hydrodynamics by evaluating the role of the bubble diameter and of the eruption frequency on heat transfer phenomena;
- Assessing the performance of the designed solar FB reactor when an additional air stream (uneven fluidization strategy) is sent through a central located nozzle with the aim of reducing the over-temperature of the FB surface;
- Assessing the CO<sub>2</sub> capture capacity of Ca-based sorbents characterized by different physico-chemical features in the solar Calcium Looping cycle.

## References

- Abanades, J.C. «The maximum capture efficiency of CO<sub>2</sub> using a carbonation/calcination cycle of CaO/CaCO<sub>3</sub>.» *Chemical Engineering Journal* 90 (2002): 303–306.
- Abanades, S., A. Legal, A. Cordier, G. Peraudeau, G. Flamant, A. Julbe. «Investigation of reactive cerium-based oxides for H<sub>2</sub> production by thermochemical two-step water-splitting.» *Journal of Materials Science* 45 (2010): 4163–4173.
- Abanades, S., G. Flamant. «Thermochemical hydrogen production from a two-step solar-driven water-splitting cycle based on cerium oxides.» *Solar Energy* 80 (2006): 1611–1623.
- Abanades, S., I. Villafan-Vidales. «CO<sub>2</sub> valorisation based on Fe<sub>3</sub>O<sub>4</sub>/FeO thermochemical redox reactions using concentrated solar energy.» *International Journal of Energy Research* 37 (2013): 598–608.
- Abanades, S., P. Charvin, G. Flamant, P. Neveu. «Screening of water-splitting thermochemical cycles potentially attractive for hydrogen production by concentrated solar energy.» *Energy* 31 (2006): 2805–2822.
- Agrafiotis, C., M. Roeb, M. Schmücker, C. Sattler. «Exploitation of thermochemical cycles based on solid oxide redox systems for thermochemical storage of solar heat. Part 1: Testing of cobalt oxide-based powders.» *Solar Energy* 102 (2014a): 189–211.
- Agrafiotis, C., H. von Storch, M. Roeb, C. Sattler. «Solar thermal reforming of methane feedstocks for hydrogen and syngas production – A review.» *Renewable and Sustainable Energy Reviews* 29 (2014b): 656–682.
- Aihara, M., T. Nagai, J. Matsushita, Y. Negishi, H. Ohya. «Development of porous solid reactant for thermal-energy storage and temperature upgrade using carbonation/decarbonation reaction.» *Applied Energy* 69 (2001): 225–238.
- Alonso, E., C. Pérez-Rábago, J. Licurgo, E. Fuentealba, C.A. Estrada. «First experimental studies of solar redox reactions of copper oxides for thermochemical energy storage.» *Solar Energy* 115 (2015): 297–305.
- Alonso, E., M. Romero. «Review of experimental investigation on directly irradiated particles solar reactors.» *Renewable and Sustainable Energy Reviews* 41 (2015): 53–67.
- Alonso, M., N. Rodríguez, B. González, G.S. Grasa, R. Murillo, J.C. Abanades. «Carbon dioxide capture from combustion flue gases with a calcium oxide chemical loop. Experimental results and process development.» *International Journal of Greenhouse Gas Control* 4 (2010): 167–173.
- Álvarez de Miguel, S., J. Gonzalez-Aguilar, M. Romero. «100-Wh multi-purpose particle reactor for thermochemical heat storage in concentrating solar power plants.» *Energy Procedia* 49 (2014): 676–683.
- Angrisani, G., K. Bizon, R. Chirone, G. Continillo, G. Fusco, S. Lombardi, F.S. Marra, F. Miccio, C. Roselli, M. Sasso, R. Solimene, F. Tariello, M. Urciuolo. «Development of a new

concept solar-biomass cogeneration system.» *Energy Conversion and Management* 75 (2013): 552–560.

Aprea, G., A. Cammarota, R. Chirone, R. Solimene, P. Salatino. «Hydrodynamic characterization of the biomass combustion in a pilot scale fluidized bed combustor.» *Chemical Engineering Transaction* 32 (2013): 1519–1524.

Babiniec, S.M., E.N. Coker, J.E. Miller, A. Ambrosini. «Investigation of  $\text{La}_x\text{Sr}_{1-x}\text{Co}_y\text{M}_{1-y}\text{O}_{3-\delta}$  (M = Mn, Fe) perovskite materials as thermochemical energy storage media.» *Solar Energy* 118 (2015): 451–459.

Bachovchin, D.M., D.H. Archer, D.H. Neale. «Heat transfer in a fluidized-bed solar thermal receiver.» *AIChE Symposium Series* 79 (1983): 27–36.

Badie, J.M., C. Bonet, M. Faure, G. Flamant, R. Foro, D. Hernandez. «Decarbonation of calcite and phosphate rock in solar chemical reactors.» *Chemical Engineering Science* 35 (1980): 413–420.

Benoit, H., I. Pérez López, D. Gauthier, J.-L. Sans, G. Flamant. «On-sun demonstration of a 750 °C heat transfer fluid for concentrating solar systems: Dense particle suspension in tube.» *Solar Energy* 118 (2015): 622–633.

Blamey, J., E.J. Anthony, J. Wang, P.S. Fennell. «The calcium looping cycle for large-scale  $\text{CO}_2$  capture.» *Progress in Energy and Combustion Science* 36 (2010): 260–279.

Block, T., N. Knoblauch, M. Schmücker. «The cobalt-oxide/iron-oxide binary system for use as high temperature thermochemical energy storage material.» *Thermochemica Acta* 577 (2014): 25–32.

Borodulya, V.A., Yu.G. Epanov, Yu.S. Teplitskii. «Horizontal particle mixing in a free fluidized bed.» *Journal of Engineering Physics* 42 (1982): 528–533.

Boot-Handford, M.E., J.C. Abanades, E.J. Anthony, M.J. Blunt, S. Brandani, N. Mac Dowell, J.R. Fernández, M.C. Ferrari, R. Gross, J.P. Hallett, R.S. Haszeldine, P. Heptonstall, A. Lyngfelt, Z. Makuch, E. Mangano, R.T.J. Porter, M. Pourkashanian, G.T. Rochelle, N. Shah, J.G. Yao, P.S. Fennell. «Carbon capture and storage update. » *Energy & Environmental Science* 7 (2014): 130–189.

Call, F., M. Roeb, M. Schmücker, C. Sattler, R. Pitz-Paal. «Ceria doped with zirconium and lanthanide oxides to enhance solar thermochemical production of fuels.» *The Journal Of Physical Chemistry* 119 (2015): 6929–6938.

Carrillo, A.J., J. Moya, A. Bayón, P. Jana, V.A. de la Peña O'Shea, M. Romero, J. Gonzalez-Aguilar, D.P. Serrano, P. Pizarro, J.M. Coronado. «Thermochemical energy storage at high temperature via redox cycles of Mn and Co oxides: Pure oxides versus mixed ones.» *Solar Energy Materials & Solar Cells* 123 (2014): 47–57.

Charitos, A., N. Rodríguez, C. Hawthorne, M. Alonso, M. Zieba, B. Arias, G. Kopanakis, G. Scheffknecht, J.C. Abanades. «Experimental validation of the calcium looping  $\text{CO}_2$  capture process with two circulating fluidized bed carbonator reactors.» *Industrial & Engineering Chemistry Research* 50 (2011): 9685–9695.

- Charitos, A., C. Hawthorne, A.R. Bidwe, S. Sivalingam, A. Schuster, H. Spliethoff, G. Scheffknecht. «Parametric investigation of the calcium looping process for CO<sub>2</sub> capture in a 10 kW<sub>th</sub> dual fluidized bed.» *International Journal Of Greenhouse Gas Control* 4 (2010): 776–784.
- Charvin, P., S. Abanades, F. Lemort, G. Flamant. «Hydrogen production by three-step solar thermochemical cycles using hydroxides and metal oxide systems.» *Energy & Fuels* 21 (2007a): 2919–2928.
- Charvin, P., S. Abanades, G. Flamant, F. Lemort. «Two-step water splitting thermochemical cycle based on iron oxide redox pair for solar hydrogen production.» *Energy* 32 (2007b): 1124–1133.
- Chen, H., C. Zhao, Y. Yang. «Enhancement of attrition resistance and cyclic CO<sub>2</sub> capture of calcium-based sorbent pellets.» *Fuel Processing Technology* 116 (2013): 116–122.
- Chen, J.C. Heat Transfer, Chapter 10, in: Yang, W.C. (Ed.), *Handbook of Fluidization and Fluid-Particle Systems*, Marcel Dekker Inc., 2003.
- Chirone, R., P. Salatino, P. Ammendola, R. Solimene, M. Magaldi, R. Sorrenti, G. De Michele, F. Donatini. «Development of a novel concept of solar receiver/thermal energy storage system based on compartmented dense gas fluidized beds.» In: *Proceedings of the 14th international conference on fluidization – from fundamentals to products*. Noordwijkerhout, The Netherlands, 2013. 95–102.
- Chueh, W.C., C. Falter, M. Abbott, D. Scipio, P. Furler, S.M. Haile, A. Steinfeld. «High-flux solar-driven thermochemical dissociation of CO<sub>2</sub> and H<sub>2</sub>O using nonstoichiometric ceria.» *Science* 330 (2010): 1797–1801.
- Coppola, A., F. Montagnaro, P. Salatino, F. Scala. «Fluidized bed calcium looping: the effect of SO<sub>2</sub> on sorbent attrition and CO<sub>2</sub> capture capacity.» *Chemical Engineering Journal* 207–208 (2012): 445–449.
- Coppola, A., F. Scala, P. Salatino, F. Montagnaro. «Fluidized bed calcium looping cycles for CO<sub>2</sub> capture under oxy-firing calcination conditions: Part 1. Assessment of six limestones.» *Chemical Engineering Journal* 231 (2013): 537–543.
- Coppola, A., L. Palladino, F. Montagnaro, F. Scala, P. Salatino. «Reactivation by steam hydration of sorbents for fluidized-bed calcium looping.» *Energy & Fuels* 29 (2015): 4436–4446.
- Coppola, A., P. Salatino, F. Montagnaro, F. Scala. «Hydration-induced reactivation of spent sorbents for fluidized bed calcium looping (double looping).» *Fuel Processing Technology* 120 (2014): 71–78.
- Cot-Gores, J., A. Catell, L.F. Cabeza. «Thermochemical energy storage and conversion: A-state-of-the-art review of the experimental research under practical conditions.» *Renewable and Sustainable Energy Reviews* 16 (2012): 5207–5224.
- Dean, C.C., J. Blamey, N.H. Florin, M.J. Al-Jeboori, P.S. Fennell. «The calcium looping cycle for CO<sub>2</sub> capture from power generation, cement manufacture and hydrogen production.» *Chemical Engineering Research and Design* 89 (2011): 836–855.

- Demont, A., S. Abanades. «Solar thermochemical conversion of CO<sub>2</sub> into fuel via two-step redox cycling of non-stoichiometric Mn-containing perovskite oxides.» *Journal of Materials Chemistry A* 3 (2015): 3536–3546.
- Demont, A., S. Abanades, E. Beche. «Investigation of perovskite structures as oxygen-exchange redox materials for hydrogen production from thermochemical two-step water-splitting cycles.» *The Journal of Physical Chemistry* 118 (2014): 12682–12692.
- Dieter, H., A.R. Bidwe, G. Varela-Duelli, A. Charitos, C. Hawthorne, G. Scheffknecht. «Development of the calcium looping CO<sub>2</sub> capture technology from lab to pilot scale at IFK, University of Stuttgart.» *Fuel* 127 (2014): 23–37.
- Edwards, S.E.B., V. Materić. «Calcium looping in solar power generation plants.» *Solar Energy* 86 (2012): 2494–2503.
- Einstein, A. Investigations on the Theory of the Brownian Movement. *Dover Publications Inc.*, New York, 1956.
- El Chaar, L., L.A. Iamont, N. El Zein. «Review of photovoltaic technologies.» *Renewable and Sustainable Energy Reviews* 15 (2011): 2165–2175.
- Ervin, G. «Solar heat storage using chemical reactions.» *Journal of Solid State Chemistry* 22 (1977): 51–61.
- Farzaneh, M., S. Sasic, A.-E. Almstedt, F. Johnsson, D. Pallarès. «A study of fuel particle movement in fluidized beds.» *Industrial Chemical Engineering Research* 52 (2013): 5791–5805.
- Felderhoff, M., B. Bogdanović. «High temperature metal hydrides as heat storage materials for solar and related applications.» *International Journal of Molecular Sciences*, n. 10 (2009): 325–344.
- Felderhoff, M., R. Urbanczyk, S. Peil. «Thermochemical heat storages for high temperature applications – A review.» *Green* 3 (2013): 113–123.
- Fernandes, D., F. Pitié, G. Cáceres, J. Baeyens. «Thermal energy storage: “How previous findings determine current research priorities”.» *Energy* 39 (2012): 246–257.
- Flamant, G. «Theoretical and experimental study of radiant heat transfer in a solar fluidized-bed receiver.» *AIChE Journal* 28 (1982): 529–535.
- Flamant, G., D. Hernandez, C. Bonet, Traverse J.P. «Experimental aspects of the thermochemical conversion of solar energy; Decarbonation of CaCO<sub>3</sub>.» *Solar Energy* 24 (1980): 385–395.
- Flamant, G., G. Olalde. «High temperature solar gas heating comparison between packed and fluidized bed receivers–I.» *Solar Energy* 21 (1983): 463–471.
- Flamant, G., D. Gauthier, H. Benoit, J.-L. Sans, R. Garcia B. Boissière, B. Ansart, M. Hemati. «Dense suspension of solid particles as a new heat transfer fluid for concentrated solar thermal plants: On-sun proof of concept.» *Chemical Engineering Science* 102 (2013): 567–576.
- Furler, P., A. Steinfeld. «Heat transfer and fluid flow analysis of a 4 kW solar thermochemical reactor for ceria redox cycling.» *Chemical Engineering Science* 137 (2015): 373–383.

- Gil, A., M. Medrano, I. Martorell, A. Lázaro, P. Dolado, B. Zalba, L.F. Cabeza. «State of the art on high temperature thermal energy storage for power generation. Part 1—Concepts, materials and modellization.» *Renewable and Sustainable Energy Reviews* 14 (2010): 31–55.
- Glasson, D.R., M.A. Sheppard. «Reactivity of lime and related oxides. XIX. Production of strontium oxide.» *Journal of Applied Chemistry* 18 (2007): 327–329.
- Gokon, N., R. Ono, T. Hatamachi, L. Liuyun, H.-J. Kim, T. Kodama. «CO<sub>2</sub> gasification of coal cokes using internally circulating fluidized bed reactor by concentrated Xe-light irradiation for solar gasification.» *International Journal of Hydrogen Energy* 37 (2012): 12128–12137.
- Gokon, N., S. Sagawa, T. Kodama. «Comparative study of activity of cerium oxide at thermal reduction temperatures of 1300–1550°C for solar thermochemical two-step water-splitting cycle.» *International Journal Of Hydrogen Energy* 38 (2013): 14402–14414.
- Gokon, N., T. Izawa, T. Kodama. «Steam gasification of coal cokes by internally circulating fluidized-bed reactor by concentrated Xe-light radiation for solar syngas production.» *Energy* 79 (2015a): 264–272.
- Gokon, N., T. Mataga, N. Kondo, T. Kodama. «Thermochemical two-step water splitting by internally circulating fluidized bed of NiFe<sub>2</sub>O<sub>4</sub> particles: Successive reaction of thermal-reduction and water-decomposition steps.» *International Journal of Hydrogen Energy* 36 (2011): 4757–4767.
- Gokon, N., T. Suda, T. Kodama. «Thermochemical reactivity of 5–15 mol% Fe, Co, Ni, Mn-doped cerium oxides in two-step water-splitting cycle for solar hydrogen production.» *Thermochimica Acta* 617 (2015b): 179–190.
- Gordillo, E.D., A. Belghit. «A bubbling fluidized bed solar reactor model of biomass char high temperature steam-only gasification.» *Fuel Processing Technology* 92 (2011): 314–321.
- Green, D.W., R.H. Perry. *Perry's Chemical Engineers' Handbook*, 8th Edition. McGraw–Hill, 2008.
- Guo, P., P.J. van Eyk, W.L. Saw, P.J. Ashman, G.J. Nathan, E.B. Stechel. «Performance assessment of Fischer–Tropsch liquid fuels production by solar hybridized dual fluidized bed gasification of lignite.» *Energy & Fuels* 29 (2015): 2738–2751.
- Herrmann, U., D.W. Kearney. «Survey of thermal energy storage for parabolic trough power plants.» *Journal of Solar Energy Engineering* 124 (2002): 145–152.
- Hoffert, M.I., K. Caldeira, G. Benford, D.R. Criswell, C. Green, H. Herzog, A.K. Jain, H.S. Khesghi, K.S. Lackner, J.S. Lewis, H.D. Lightfoot, W. Manheimer, J.C. Mankins, M.E. Mauel, L.J. Perkins, M.E. Schlesinger, T. Volk, T.M.L. Wigley. «Advanced technology paths to global climate stability: energy for a greenhouse planet.» *Science* 298 (2002): 981–987.
- Imhof, A. «Calcination of limestone in a solar reactor.» *ZKG International* 53 (2000): 504–509.
- Imhof, A. «Decomposition of limestone in a solar reactor.» *Renewable Energy* 10 (1997): 239–246.
- Imhof, A. «The cyclone reactor - an atmospheric open solar reactor.» *Solar Energy Materials* 24 (1991): 733–741.

- Jiang, Q., J. Tong, G. Zhou, Z. Jiang, Z. Li, C. Li. «Thermochemical CO<sub>2</sub> splitting reaction with supported La<sub>x</sub>A<sub>1-x</sub>Fe<sub>y</sub>B<sub>1-y</sub>O<sub>3</sub> (A = Sr, Ce, B = Co, Mn; 0 ≤ x, y ≤ 1).» *Solar Energy* 103 (2014): 425–437.
- Kaniyal, A.A., P.J. van Eyk, G.J. Nathan, P.J. Ashman, J.J. Pincus. «Polygeneration of liquid fuels and electricity by the atmospheric pressure hybrid solar gasification of coal.» *Energy & Fuels* 27 (2013): 3538–3555.
- Kato, Y., R. Takahashi, T. Sekiguchi, J. Ryu. «Study on medium-temperature chemical heat storage using mixed hydroxides.» *International Journal of Refrigeration* 32 (2009): 661–666.
- Kodama, T. «High-temperature solar chemistry for converting solar heat to chemical fuels.» *Progress in Energy and Combustion Science* 29 (2003): 567–597.
- Kodama, T., N. Gokon. «Thermochemical cycles for high-temperature solar hydrogen production.» *Chemical Reviews* 107 (2007): 4048–4077.
- Kodama, T., N. Gokon, N. Yamamoto. «Thermochemical two-step water splitting by ZrO<sub>2</sub>-supported Ni<sub>x</sub>Fe<sub>3-x</sub>O<sub>4</sub> for solar hydrogen production.» *Solar Energy* 82 (2008): 73–79.
- Kodama, T., Y. Kondoh, R. Yamamoto, H. Andou, N. Satou. «Thermochemical hydrogen production by a redox system of ZrO<sub>2</sub>-supported Co(II)-ferrite.» *Solar Energy* 78 (2005): 623–631.
- Kodama, T., Y. Kondoh, T. Tamagawa, A. Funatoh, K.-I. Shimizu, Y. Kitayama. «Fluidized bed coal gasification with CO<sub>2</sub> under direct irradiation with concentrated visible light.» *Energy & Fuels* 16 (2002): 1264–1270.
- Koenigsdorff, R., P. Kienzle. «Results of and prospects for research on direct-absorption fluidized bed solar receivers.» *Solar Energy Materials* 24 (1991): 279–283.
- Kunii, D., O. Levenspiel. *Fluidization Engineering*, 2nd Edition. *Butterworth-Heinemann*, 1991.
- Le Gal, A., S. Abanades, G. Flamant. «CO<sub>2</sub> and H<sub>2</sub>O splitting for thermochemical production of solar fuels using nonstoichiometric ceria and ceria/zirconia solid solutions.» *Energy & Fuels* 25 (2011): 4836–4845.
- Li, F., L.S. Fan. «Clean coal conversion process – progress and challenges.» *Energy & Environmental Science* 1 (2008): 248–267.
- Lisbona, P., A. Martínez, L.M. Romeo. «Hydrodynamical model and experimental results of a calcium looping cycle for CO<sub>2</sub> capture.» *Applied Energy* 101 (2013): 317–322.
- Liu, D., X. Chen. «Lateral solids dispersion coefficient in large-scale fluidized beds.» *Combustion and Flame* 157 (2010): 2116–2124.
- Loutzenhiser, P.G., A. Meier, A. Steinfeld. «Review of the two-step H<sub>2</sub>O/CO<sub>2</sub>-splitting solar thermochemical cycle based on Zn/ZnO redox reactions.» *Materials* 3 (2010): 4922–4938.
- Martínez, I., G. Grasa, R. Murillo, B. Arias, J.C. Abanades. «Modeling the continuous calcination of CaCO<sub>3</sub> in a Ca-looping system.» *Chemical Engineering Journal* 215–216 (2013): 174–181.

- Matsubara, K., Y. Kazuma, A. Sakurai, S. Suzuki, L. Soon-Jae, T. Kodama, N. Gokon, C. Hyun Seok, K. Yoshida. «High-temperature fluidized receiver for concentrated solar radiation by a beam-down reflector system.» *Energy Procedia* 49 (2014): 447–456.
- Matthews, L., W. Lipiński. «Thermodynamic analysis of solar thermochemical CO<sub>2</sub> capture via carbonation/calcination cycle with heat recovery.» *Energy* 45 (2012): 900–907.
- McDaniel, A.H., E.C. Miller, D. Arifin, A. Ambrosini, E.N. Coker, R. O'Hayre, W.C. Chueh, J. Tong. «Sr- and Mn-doped LaAlO<sub>3-δ</sub> for solar thermochemical H<sub>2</sub> and CO production.» *Energy & Environmental Science* 6 (2013): 2424–2428.
- Meier, A., E. Bonaldi, G.M. Cella, W. Lipinski, D. Wuillemin, R. Palumbo. «Design and experimental investigation of a horizontal rotary reactor for the solar thermal production of lime.» *Energy* 29 (2004): 811–821.
- Mills, D. «Advances in Solar Thermal Electricity Technology.» *Solar Energy* 76 (2004): 19–31.
- Mokhtar, M., S.A. Meyers, P.R. Armstrong, M. Chiesa. «Performance of a 100 kW<sub>th</sub> concentrated solar beam-down optical experiment.» *Journal of Solar Engineering* 136 (2014): 041007-1–041007-8.
- Montagnaro, F., P. Salatino, F. Scala. «The influence of sorbent properties and reaction temperature on sorbent attrition, sulfur uptake, and particle sulfation pattern during fluidized-bed desulfurization.» *Combustion Science and Technology* 174 (2002): 151–169.
- Montagnaro, F., P. Salatino, F. Scala, M. Urciuolo. «A population balance model on sorbent in CFB combustors: the influence of particle attrition.» *Industrial & Engineering Chemistry Research* 50 (2011): 9704–9711.
- Müller, R., A. Steinfeld. «H<sub>2</sub>O-splitting thermochemical cycle based on ZnO/Zn-redox: Quenching the effluents from the ZnO dissociation.» *Chemical Engineering Science* 63 (2008): 217–227.
- Müller, R., P.v. Zedtwitz, A. Wokaun, A. Steinfeld. «Kinetic investigation on steam gasification of charcoal under direct high-flux irradiation.» *Chemical Engineering Science* 58 (2003): 5111–5119.
- Muradov, N.Z., T.N. Verizoğlu. «"Green" path from fossil-based to hydrogen economy: an overview of carbon-neutral technologies.» *International Journal of Hydrogen Energy* 33 (2008): 6804–6839.
- Nikulshina, V., C. Gebald, A. Steinfeld. «CO<sub>2</sub> capture from atmospheric air via consecutive CaO-carbonation and CaCO<sub>3</sub>-calcination cycles in a fluidized-bed solar reactor.» *Chemical Engineering Journal* 146 (2009): 244–248.
- Nikulshina, V., A. Steinfeld. «CO<sub>2</sub> capture from air via CaO-carbonation using a solar-driven fluidized bed reactor - Effect of temperature and water vapor concentration.» *Chemical Engineering Journal* 155 (2009): 867–873.
- N'Tsoukpoe, K.E., H. Liu, N. Le Pierrès, L. Luo. «A review on long-term sorption solar energy storage.» *Renewable and Sustainable Energy Reviews* 13 (2009): 2385–2396.

- N'Tsoukpoe, K.E., T. Schmidt, H.U. Rammelberg, B.A. Watts, W.K.L. Ruck. «A systematic multi-step screening of numerous salt hydrates for low temperature thermochemical energy storage.» *Applied Energy* 124 (2014): 1–16.
- Olalde, G., J.L. Peube, M. Daguene. «Theoretical study of gas heated in a porous material subjected to a concentrated solar radiation.» *Revue de Physique Appliquée* 15 (1980): 423–426.
- Pardo, P., Z. Anxionnaz-Minvielle, S. Rougé, P. Cognet, M. Cabassud. «Ca(OH)<sub>2</sub>/CaO reversible reaction in a fluidized bed reactor for thermochemical heat storage.» *Solar Energy* 107 (2014a): 605–616.
- Pardo, P., A. Deydier, Z. Anxionnaz-Minvielle, S. Rougé, M. Cabassud, P. Cognet. «A review on high temperature thermochemical heat energy storage.» *Renewable and Sustainable Energy Reviews* 32 (2014b): 591–610.
- Parida, B., S. Iniyar, R. Goic. «A review of solar photovoltaic technologies.» *Renewable and Sustainable Energy Reviews* 15 (2011): 1625–1636.
- Pemberton, S.T., J.F. Davidson. «Elutriation from fluidized beds—I. Particle ejection from the dense phase into the freeboard.» *Chemical Engineering Science* 41 (1986a): 243–251.
- Pemberton, S. T., J. F. Davidson. «Elutriation from fluidized beds—II. Disengagement of particles from gas in the freeboard.» *Chemical Engineering Science* 41 (1986b): 253–262.
- Reich, L., L. Yue, R. Bader, W. Lipiński. «Towards solar thermochemical carbon dioxide capture via calcium oxide: A review.» *Aerosol and Air Quality Research* 14 (2014): 500–514.
- REN21's Renewables Global Status Report, 2015.*
- Rodríguez, N., M. Alonso, J.C. Abanades. «Experimental investigation of a circulating fluidized-bed reactor to capture CO<sub>2</sub> with CaO.» *AIChE Journal* 57 (2011a): 1356–1366.
- Rodríguez, N., M. Alonso, J.C. Abanades, A. Charitos, C. Hawthorne, G. Scheffknecht, D.Y. Lu, E.J. Anthony. «Comparison of experimental results from three dual fluidized bed test facilities capturing CO<sub>2</sub> with CaO.» *Energy Procedia* 4 (2011b): 393–401.
- Romano, M.C. «Modeling the carbonator of a Ca-looping process for CO<sub>2</sub> capture from power plant flue gas.» *Chemical Engineering Science* 69 (2012): 257–269.
- Romeo, L.M., J.C. Abanades, J.M. Escosa, J. Paño, A. Giménez, A. Sánchez-Biezma, J.C. Ballesteros. «Oxyfuel carbonation/calcination cycle for low cost CO<sub>2</sub> capture in existing power plants.» *Energy Conversion and Management* 49 (2008): 2809–2814.
- Romeo, L.M., Y. Lara, P. Lisbona, J.M. Escosa. «Optimizing make-up flow in a CO<sub>2</sub> capture system using CaO.» *Chemical Engineering Journal* 147 (2009): 252–258.
- Romero, M., A. Steinfeld. «Concentrating solar thermal power and thermochemical fuels.» *Energy & Environmental Science* 5 (2012): 9234–9245.
- Salatino, P., P. Ammendola, P. Bareschino, R. Chirone, R. Solimene. «Improving the thermal performance of fluidized beds for concentrated solar power and thermal energy storage.» *Powder Technology* 290 (2016): 97–101.
- Sasse, C., G. Ingel. «The role of the optical properties of solids in solar direct absorption process.» *Solar Energy Materials and Solar Cells* 31 (1993): 61–73.

- Scala, F., A. Cammarota, R. Chirone, P. Salatino. «Comminution of limestone during batch fluidized-bed calcination and sulfation.» *AIChE Journal* 43 (1997): 363–373.
- Schaube, F., A. Kohzer, J. Schütz, A. Wörner, H. Müller-Steinhagen. «De- and rehydration of  $\text{Ca}(\text{OH})_2$  in a reactor with direct heat transfer for thermo-chemical heat storage. Part A: Experimental results.» *Chemical Engineering Research and Science* 91 (2013): 856–864.
- Schaube, F., L. Koch, A. Wörner, H. Müller-Steinhagen. «A thermodynamic and kinetic study of the de- and rehydration of  $\text{Ca}(\text{OH})_2$  at high  $\text{H}_2\text{O}$  partial pressures for thermo-chemical heat storage.» *Thermochimica Acta* 538 (2012): 9–20.
- Scheffe, J. R., A. Steinfeld. «Oxygen exchange materials for solar thermochemical splitting of  $\text{H}_2\text{O}$  and  $\text{CO}_2$ : a review.» *Materials Today* 17 (2014): 341–348.
- Scheffe, J.R., D. Weibel, A. Steinfeld. «Lanthanum–strontium–manganese perovskites as redox materials for solar thermochemical splitting of  $\text{H}_2\text{O}$  and  $\text{CO}_2$ .» *Energy Fuels* 27 (2013): 4250–4257.
- Schmidt, M., C. Szczukowski, C. Roßkopf, M. Linder, A. Wörner. «Experimental results of a 10 kW high temperature thermochemical storage reactor based on calcium hydroxide.» *Applied Thermal Engineering* 62 (2014): 553–559.
- Segal, A., M. Epstein. «The optics of the solar tower reflector.» *Solar Energy* 69 (2000): 229–241.
- Shimizu, T., T. Hirama, H. Hosoda, K. Kitano, M. Inagaki, K. Tejima. «A twin fluid-bed reactor for removal of  $\text{CO}_2$  from combustion processes.» *Chemical Engineering Research and Design* 77 (1999): 62–68.
- Solimene, R., P. Fenelli, R. Chirone, P. Salatino. «Heat transfer phenomena in bubbling fluidized beds for concentrated solar power.» In: *Proceedings of the 11th international conference on fluidized bed technology*. Beijing, China, 2014. 435–440.
- Solimene, R., R. Chirone, P. Salatino. «Characterization of the devolatilization rate of solid fuels in fluidized beds by time-resolved pressure measurements.» *AIChE Journal* 58 (2012): 632–645.
- Spelling, J., A. Gallo, A. Romero, J. González-Aguilar. «A high-efficiency solar thermal power plant using a dense particle suspension as the heat transfer fluid.» *Energy Procedia* 69 (2015): 1160–1170.
- Stanmore, B.R., P. Gilot. «Review - Calcination and carbonation of limestone during thermal cycling for  $\text{CO}_2$  sequestration.» *Fuel Processing Technology* 86 (2005): 1707–1743.
- Steinfeld, A., A. Meier. «Solar fuels and materials.» *Encyclopedia of Energy* 5 (2004): 623–637.
- Stern, K.H., E.L. Weise. «High temperature properties and decomposition of inorganic salts, Part 2. Carbonates.» *NSRDS–NBS* 30 (1969): 1–27.
- Ströhle, J., M. Junk, J. Kremer, A. Galloy, B. Epple. «Carbonate looping experiments in a 1  $\text{MW}_{\text{th}}$  pilot plant and model validation.» *Fuel* 127 (2014): 13–22.
- Valverde, J.M., M.A.S. Quintanilla. «Attrition of Ca-based  $\text{CO}_2$ -adsorbents by a high velocity gas jet.» *AIChE Journal* 59 (2013): 1096–1107.

- Viebahn, P., J. Nitsch, M. Fishedick, A. Esken, D. Schüwer, N. Supersberger, U. Zuberbühler, O. Edenhofer. «Comparison of carbon capture and storage with renewable energy technologies regarding structural, economic, and ecological aspects in Germany.» *International Journal of Greenhouse Gas Control* 1 (2007): 121–133.
- von Zedtwitz, P., A. Steinfeld. «Steam-gasification of coal in a fluidized-bed/packed-bed reactor exposed to concentrated thermal radiation – Modeling and experimental validation.» *Industrial & Engineering Chemistry Research* 44 (2005): 3852–3861.
- von Zedtwitz, P., W. Lipiński, A. Steinfeld. «Numerical and experimental study of gas-particle radiative heat exchange in a fluidized-bed reactor for steam-gasification of coal.» *Chemical Engineering Science* 62 (2007): 599–607.
- Vorrias, I., K. Atsonios, A. Nikolopoulos, N. Nikolopoulos, P. Grammelis, e E. Kakaras. «Calcium looping for CO<sub>2</sub> capture from a lignite fired power plant.» *Fuel* 113 (2013): 826–836.
- Werther, J., P. Molerus. «The local structure of gas fluidized beds – I. A statistically based measuring system.» *International Journal of Multiphase Flow* 1 (1973): 103–122.
- Werther, J., R. Koenigsdorff, e M. Fischer. «Use of circulating fluidized beds as solar receivers.» *Preprints of Annual Meeting Society of Chemical Engineers*. Japan Sendai, March 28–30, 1994. 60–61.
- Wong, B. «Thermochemical heat storage for concentrated solar power, thermochemical system reactor design for thermal energy storage, *Phase II Final report for the period September 30, 2008 through April 30, 2011.*» 2011.
- Yadav, D., R. Banerjee. «A review of solar thermochemical processes.» *Renewable and Sustainable Energy Reviews* 54 (2016): 497–532.
- Yu, N., R.Z. Wang, L.W. Wang. «Sorption thermal storage for solar energy.» *Progress in Energy and Combustion Science* 39 (2013): 489–514.
- Zhang, X., Y. Liu. «Performance assessment of CO<sub>2</sub> capture with calcination carbonation reaction process driven by coal and concentrated solar power.» *Applied Thermal Engineering* 70 (2014): 13–24.